

## ABSTRACT

Title of Document: SYNTHESIS AND CHARACTERIZATION OF  
BIMETALLIC ZINTL CLUSTERS AND THEIR  
USE IN THE FABRICATION OF  
INTERMETALIC NANOPARTICLES

Domonique O. Downing  
Doctor of Philosophy, 2012

Directed By: Professor Bryan W. Eichhorn  
Department of Chemistry and Biochemistry

In this thesis, the synthesis, characterization and applications of bimetallic Zintl clusters are explored. Zintl ions are polyanions of main group elements, primarily of the heavier elements of groups 14 and 15. The *closo*-Sn<sub>9</sub>Ir(cod)<sup>3-</sup>, Sn<sub>9</sub>Rh(cod)<sup>3-</sup>, and Pb<sub>9</sub>Ir(cod)<sup>3-</sup> ions were prepared from precursors E<sub>9</sub><sup>4-</sup> (E = Sn, Pb), [M(cod)Cl]<sub>2</sub> (M = Rh, Ir) and 2,2,2-crypt in ethylenediamine/toluene solvent mixtures. The clusters were isolated and characterized via NMR spectroscopy and single-crystal X-ray diffraction studies. The *closo*-E<sub>9</sub>Ir(cod)<sup>3-</sup> ions are the first known Ir(I) Zintl clusters and are examples of isostructural Sn/Pb homologues. All three complexes have 22-electron, bicapped square-antiprismatic structures and pseudo-C<sub>4v</sub> point symmetry with the Ir(cod) and Rh(cod) vertices attached in an η<sup>4</sup> fashion. The Sn<sub>9</sub>Rh(cod)<sup>3-</sup> ion possesses <sup>119</sup>Sn NMR chemical shifts that are consistent with other known Sn<sub>9</sub><sup>4-</sup> transition metal derivatives. The structural studies and <sup>1</sup>H and <sup>13</sup>C NMR studies showed significant charge transfer to the cod ligands.

Novel  $\text{Rh@Sn}_{12}^{3-}$  and  $\text{Rh@Pb}_{12}^{3-}$  ions have been prepared and isolated in the solid state and the latter has been studied via  $^{207}\text{Pb}$  NMR. The ions are 26-electron clusters with near perfect icosahedral  $I_h$  point symmetry. Additionally,  $\text{Ir@Pb}_{12}^{3-}$  and the previously isolated  $\text{Ir@Sn}_{12}^{3-}$  ion [Fässler *et al.* 2010, *Chem. Eur. J.*] were detected for the first time via  $^{207}\text{Pb}$  and  $^{117}\text{Sn}$  NMR, respectively. The  $^{207}\text{Pb}$  NMR of  $\text{Rh@Pb}_{12}^{3-}$  and  $\text{Ir@Pb}_{12}^{3-}$  have the most downfield  $^{207}\text{Pb}$  signals known to date, due to their  $\sigma$ -aromaticity.

The  $\text{Sn}_9^{4-}$  and  $\text{As}_7^{3-}$  Zintl ions were shown to be effective reducing agents in the synthesis of three novel transition metal complexes. The synthesis and crystallographic characterization of the novel  $[\text{Rh}_2\text{H}(\text{PPh}_2)_2(\text{PPh}_3)_3]^-$ ,  $\text{Co}_3(\text{CO})_7^{3-}$ , and  $[(\text{C}_3\text{H}_7\text{N}_2\text{O})_3\text{Ir}_4(\text{CO})_9]^{3-}$  ions are reported for the first time and cannot be prepared using traditional reducing agents.

Controlled  $\text{I}_2$  oxidations of preformed Zintl clusters  $\text{Pt@Sn}_9\text{Pt}(\text{PPh}_3)^{2-}$  and  $\text{Sn}_9\text{Ir}(\text{cod})^{3-}$ , give well ordered tin-rich intermetallic nanoparticles of  $\text{PtSn}_4$  and  $\text{Ir}_3\text{Sn}_7$ , respectively. The intermetallics were characterized by HR-TEM and XRD analysis. Both clusters have strong structural similarities with the final intermetallic, which appears to be an important factor in determining the phase of the resulting intermetallic nanoparticles. Despite the 1:9 (Ir:Sn) atomic ratio of the  $\text{Sn}_9\text{Ir}(\text{cod})^{3-}$  cluster, ordered  $\text{Ir}_3\text{Sn}_7$  nanoparticles were formed instead of the compositionally-similar  $\text{IrSn}_4$  phase.  $\text{PtSn}_4$  is difficult to prepare by traditional methods and isolate due to the formation of other known Pt-Sn phases, such as  $\text{PtSn}$ ,  $\text{PtSn}_2$  and  $\text{Pt}_3\text{Sn}$ .

SYNTHESIS AND CHARACTERIZATION OF BIMETALLIC ZINTL  
CLUSTERS AND THEIR USE IN THE FABRICATION OF INTERMETALLIC  
NANOPARTICLES

by

Domonique O. Downing

Dissertation submitted to the Faculty of the Graduate School of the  
University of Maryland, College Park, in partial fulfillment  
of the requirements for the degree of  
Doctor of Philosophy  
2012

Advisory Committee:

Professor Bryan W. Eichhorn, Chair

Professor Sheryl H. Ehrman, Dean's Representative

Professor Jeffery T. Davis

Professor Lawrence R. Sita

Professor Andrei N. Vedernikov

© Copyright by  
Domonique O. Downing  
2012

## Dedication

This dissertation is dedicated to my loving and supportive family, especially my grandmother, Sadie Downing, who passed shortly after the completion of this dissertation. Thank you for everything, Grandma.

## Acknowledgements

I would like to thank my advisor, Prof. Bryan Eichhorn. It has been a true pleasure to work with him and I cannot imagine completing my PhD with anyone else. I never thought I would end up doing research in an inorganic chemistry lab. I was able to be successful because of his ability to teach me the chemistry and techniques and his ability to encourage me when things were not working. I also appreciate his advice, professionalism, and his passion for chemistry. Thanks for everything, Bryan.

I also thank all of my past lab mates from the Eichhorn research group—Dr. Zhufang Liu, Dr. Chunjuan Zhang, Dr. Yang Peng, Dr. Aldo Ponce, Dr. Tony Dylla, Dr. Selim Alayoglu, Dr. F. Sanem Kocak, Dr. Dennis Mayo, André Dennis, Pavan Bellamkonda, Chris Sims, Yi Yu, Samantha DeCarlo, Jonathan Senn, and Aaron Gellar. I sincerely especially thank Sanem for her advice and teaching me all she knew about the field and NMR. I also thank Zhufang and Chris for their help in carrying out XRD and TEM experiments, and special thanks go to Dennis and Zhufang for opening gas tanks for me all of the time.

I would like to thank Dr. Yiu-fai Lam for teaching me how to run NMR experiments as well as for his assistance in executing difficult NMR experiments. I thank Dr. Yinde Wang and Frederick Nytko, III for their assistance at the NMR facility as well. I thank Dr. Peter Zavalij for running crystallography experiments. I would also like to thank the staff at the NISP NanoCenter, Dr. Wen-An Chiou and Dr. LiChung Lai, for giving me TEM training and assisting me with the experiments.

I thank the NOBCChE chapter at Maryland for friendships made, support, and the opportunities to lead and attend conferences. My experience with NOBCChE-UMD was great and gave me the opportunity to position myself in the right situations to be successful at Maryland and beyond.

I also sincerely thank all the friends that I have made during my time at Maryland. I thank Dr. Rennisha Wickham for her friendship and advice throughout the difficult times in our program. She is a motivator like no other and pushed me to lead, apply for programs and fellowships, and has encouraged me to step out of my shell. I thank Dr. Liz Nguyen for her encouraging words and for always being someone that I could count on. I also thank Renee Siler and Jackie Smith for teaching me leadership skills and for making sure that I always stayed on top of my game. I also thank my friend Charles Gee for his valuable advice and for showing me that it is ok to be yourself and for reminding me to always “big it up.” I also thank Melantha Jackson for her friendship which will last beyond our years at Maryland. Additionally, I thank Alicia Bowen, Colef Talbert, Floyd Bates, Dr. Williamson Oloo, Derek Denning, Phong and Anna Truong, Lauren Graham, Ali Sikorsky, Joseph Peralta, Mauricio Leyva, Sofia Eriksson, Petrina Boucher, and Dr. Stefanie Sherrill for being a source of laughter and good times. I also thank everyone in the incoming classes of 2006 and 2007 for all the memorable events that we’ve shared.

Last but definitely not least, I thank my family for being a great support system. I thank my parents George and Karen Downing for always believing in me and allowing me to carve my own path. I thank my siblings George, LaQuita, and Gregory for always staying in my corner. I also thank my Aunt Sarah and her

family for always being there and encouraging me. My cousins Kimberly Zachary and Jerri Bailey have also been great to me and I appreciated having family here in Maryland. Thank you, everyone!



# Table of Contents

Dedication.....	ii
Acknowledgements.....	iii
Table of Contents.....	vi
List of Tables.....	ix
List of Figures.....	x
List of Abbreviations.....	xiv
List of Publications.....	xvi
Chapter 1: Introduction.....	1
1.1. Introduction to Zintl Clusters and their Relationship to Nanoparticles.....	1
1.2. Zintl Ions.....	6
1.3. Transition Metal Derivatives of Zintl Ions.....	15
1.3.1. E <sub>9</sub> -Zintl Cluster Transition Metal Derivatives.....	16
1.3.2. Endohedral M@E <sub>10</sub> and M@E <sub>12</sub> Transition Metal Derivatives.....	20
1.3.3. Large Fused Intermetalloid Zintl Clusters.....	24
1.3.4. Oxidative Coupling and Polymerization of Zintl Clusters.....	28
1.4. Solution Dynamics of Group 14 Zintl Ions.....	30
1.5. Intermetallic Nanoparticles.....	37
1.6. Overview of the Thesis.....	39
Chapter 2: Group 9 Derivatives of Sn <sub>9</sub> <sup>4-</sup> : Sn <sub>9</sub> ML.....	40
2.1. Introduction.....	40
2.2. Results and Discussion.....	41
2.2.1. Synthesis.....	41
2.2.2. Solid State Structure.....	42
2.2.3. NMR Spectroscopic Studies.....	52
2.3. Conclusion.....	56
2.4. Experimental Section.....	57
2.4.1. General Data.....	57
2.4.2. Chemicals.....	58
2.4.3. Synthesis.....	58
Chapter 3: The Icosahedral M@E <sub>12</sub> <sup>3-</sup> clusters (E = Sn, Pb; M = Ir, Rh).....	61
3.1. Introduction.....	61
3.2. Results and Discussion.....	63

3.2.1. Synthesis .....	63
3.2.2. Solid State Structure .....	65
3.2.3. NMR Spectroscopic Studies .....	69
3.3. Conclusion .....	73
3.4. Experimental Section .....	74
3.4.1. General Data .....	74
3.4.2. Chemicals.....	74
3.4.3. Synthesis .....	75
Chapter 4: The Use of the $E_9^{4-}$ and $E_7^{3-}$ Zintl Ions as Electron Transfer Reagents: The Synthesis of the Novel $[Rh_2H(PPh_2)_2(PPh_3)_3]^-$ , $Co_3(CO)_7^{3-}$ , and $[(C_3H_7N_2O)_3Ir_4(CO)_9]^{3-}$ Ions .....	78
4.1. Introduction.....	78
4.2. Results and Discussion .....	79
4.2.1. Synthesis .....	79
4.2.2. Solid State Structure .....	80
4.2.3. NMR Spectroscopic Studies .....	93
4.3. Conclusion .....	98
4.4. Experimental Section .....	101
4.4.1. General Data .....	101
4.4.2. Chemicals.....	101
4.4.3. Synthesis .....	102
Chapter 5: Fabrication of $PtSn_4$ and $Ir_3Sn_7$ Intermetallic Nanoparticles From Bimetallic Zintl Cluster Precursors.....	104
5.1. Introduction.....	104
5.2. Results.....	107
5.2.1. Synthesis .....	107
5.2.2. Powder X-ray Diffraction and Transition Microscopy Studies .....	108
5.3. Discussion .....	112
5.4. Conclusion .....	115
5.5. Experimental Section .....	116
5.5.1. General Data .....	116
5.5.2. Chemicals.....	117
5.5.3. Synthesis .....	118
Chapter 6: Conclusions.....	120
Appendix.....	124

Appendix A. Cobalt Derivatives of $\text{Sn}_9^{4-}$ .....	124
Appendix B. Isolation of $\text{Rh@Sn}_{10}^{3-}$ .....	128
References.....	131

## List of Tables

<b>Table 1.1.</b> Tabulation of Wade's Rules for the Boranes. ....	11
<b>Table 2.1.</b> Crystallographic data for the $\text{Sn}_9\text{M}(\text{cod})^{3-}$ ions ( $\text{M} = \text{Ir}, \text{Rh}$ ).....	43
<b>Table 2.2.</b> Selected bond lengths (Å) and angles (°) for the $\text{Sn}_9\text{Ir}(\text{cod})^{3-}$ ion. ....	45
<b>Table 2.3.</b> Selected bond lengths (Å) and angles (°) for the $\text{Sn}_9\text{Rh}(\text{cod})^{3-}$ ion. ...	47
<b>Table 2.4.</b> Average Bond Distances (Å) of the $\text{Sn}_9\text{M}(\text{cod})^{3-}$ clusters .....	48
<b>Table 2.5.</b> Crystallographic data for the $\text{Pb}_9\text{Ir}(\text{cod})^{3-}$ ion. ....	49
<b>Table 2.6.</b> Selected bond lengths (Å) and angles (°) for the $\text{Pb}_9\text{Ir}(\text{cod})^{3-}$ ion. ....	50
<b>Table 2.7.</b> Bond lengths (Å) and $^{13}\text{C}$ NMR Data of $\text{E}_9\text{Ir}(\text{cod})^{3-}$ and additional Ir-cod complexes.....	54
<b>Table 2.8.</b> NMR studies of metallated derivatives of $\text{Sn}_9^{4-}$ .....	56
<b>Table 3.1.</b> Crystallographic Data for $\text{Rh}@ \text{Sn}_{12}^{3-}$ and $\text{Rh}@ \text{Pb}_{12}^{3-}$ .....	66
<b>Table 3.2.</b> Selected Bond Lengths (Å) and Angles (°) for the $\text{Rh}@ \text{Sn}_{12}^{3-}$ Ion. ...	67
<b>Table 3.3.</b> Selected Bond Lengths [Å] and Angles [deg] for the $\text{Rh}@ \text{Pb}_{12}^{3-}$ Ion. 68	
<b>Table 3.4.</b> $^{207}\text{Pb}$ NMR Data for $\text{Rh}@ \text{Pb}_{12}^{3-}$ , $\text{Ir}@ \text{Pb}_{12}^{3-}$ , and other Plumbides.....	71
<b>Table 4.1.</b> Crystallographic data for the $[\text{Rh}_2\text{H}(\text{PPh}_2)_2(\text{PPh}_3)_3]^-$ ion.....	81
<b>Table 4.2.</b> Selected Bond Lengths (Å) and Angles (°) for $[\text{Rh}_2\text{H}(\text{PPh}_2)_2(\text{PPh}_3)_3]^-$ . .....	83
<b>Table 4.3.</b> Bond lengths (Å) and oxidation states of various rhodium complexes. .....	84
<b>Table 4.4.</b> Crystallographic data for the $[\text{Co}_3(\text{CO})_7]^{3-}$ ion. ....	85
<b>Table 4.5.</b> Selected Bond Lengths (Å) and Angles (°) for $[\text{Co}_3(\text{CO})_7]^{3-}$ .....	86
<b>Table 4.6.</b> Bond lengths (Å) of $\text{Co}_3(\text{CO})_7^{3-}$ & additional cobalt carbonyl complexes. ....	88
<b>Table 4.7.</b> Crystallographic data for the $[(\text{C}_3\text{H}_7\text{N}_2\text{O})_3\text{Ir}_4(\text{CO})_9]^{3-}$ ion. ....	89
<b>Table 4.8.</b> Selected Bond Lengths (Å) and Angles (°) of $[(\text{C}_3\text{H}_7\text{N}_2\text{O})_3\text{Ir}_4(\text{CO})_9]^{3-}$ . .....	92
<b>Table 5.1.</b> Average bond lengths of Zintl clusters and intermetallics (Å). ....	114

## List of Figures

<b>Figure 1.1.</b> Hexagonal close-packed clusters with a magic number of atoms. ....	4
<b>Figure 1.2.</b> Structure of 2,2,2-crypt (left) and 18-crown-6 (right), two important sequestering agents in Zintl cluster chemistry. ....	9
<b>Figure 1.3.</b> ORTEP drawing of $C_{3v}$ $Sb_7^{3-}$ cluster in $[Na-crypt]_3Sb_7$ .....	10
<b>Figure 1.4.</b> Atomic structures of select homoatomic main-group anionic clusters. (a) $E_9^{3-}$ and $E_9^{4-}$ (b) $E_5^{2-}$ (c) $As_7^{3-}$ and $Sb_7^{3-}$ (d) $Sb_4^{2-}$ and $Bi_4^{2-}$ .....	10
<b>Figure 1.5.</b> Example of idealized <i>closo</i> , <i>nido</i> , and <i>arachno</i> boranes highlighting the structure associated with the nomenclature. Structures of (a) <i>closo</i> - $B_{12}H_{12}^{2-}$ and $E_{12}^{2-}$ , (b) <i>nido</i> - $B_{11}H_{15}$ and $E_{11}^{4-}$ , (c) <i>arachno</i> - $B_{10}H_{16}$ and $E_{10}^{6-}$ (borane hydrogens omitted). ....	13
<b>Figure 1.6.</b> The (a) $\eta^4$ (b) and $\eta^5$ structural isomers of the <i>closo</i> - $[Sn_9M(CO)_3]^{4-}$ clusters, where M = Cr, Mo, W. The tungsten cluster has been characterized crystallographally in the both isomeric forms .....	18
<b>Figure 1.7.</b> Various $E_9$ -transition metal derivative structure types. The $Ge_9CuP(iPr)_3^{3-}$ , $Sn_9Ni_2CO^{3-}$ , $Sn_9Pt_2PPh_3^{2-}$ , and $Cu@Sn_9^{3-}$ clusters possess the same framework as other (a) <i>closo</i> - $E_9ML$ $C_{4v}$ , (b) <i>closo</i> - $M@E_9ML$ $C_{4v}$ , (c) <i>closo</i> - $M@E_9ML$ $C_{3v}$ , and (d) $M@E_9$ Zintl clusters respectively. ....	19
<b>Figure 1.8.</b> Structures of (a) $Sn_9^{4-}$ , (b) <i>closo</i> - $Sn_9^{2-}$ , and (c) $Pt@Sn_9Pt(PPh_3)^{2-}$ cluster ions. The bimetallic $Pt@Sn_9Pt(PPh_3)^{2-}$ ion may be viewed as a metalated derivative of $Sn_9^{2-}$ .....	20
<b>Figure 1.9.</b> Drawing of (a) the icosohedral <i>closo</i> - $[Pt@Pb_{12}]^{2-}$ polyanion and the packing of the clusters (b) with respect to the 001 projection and (c) a side view showing the placement of the clusters with respect to the plane of potassium ions. $[K(2,2,2-crypt)]^+$ counterions (Pb = green, Pt = pink, K = blue, crypt = red and gray). The cryptands are omitted in structure c for clarity. ....	22
<b>Figure 1.10.</b> Bimetallic ligand-free ten and twelve-atom Zintl clusters. (a) $Al@Pb_{10}^+$ , $Ni@Pb_{10}^{2-}$ , (b) $Al@Pb_{12}^+$ and $M@Pb_{12}^{2-}$ (M = Ni, Pd, Pt), and (c) $M@Ge_{10}^{2-}$ (M = Co, Fe). ....	22

<b>Figure 1.11.</b> Icosohedral onion-like structure of the $[\text{As}@Ni_{12}@As_{20}]^{3-}$ polyanion.....	24
<b>Figure 1.12.</b> Crystal structures of (a) $Ni@Ge_9^{3-}$ , (b) $Ni@Ge_9Ni(PPh_3)^{2-}$ , and (c) $Ni_3@Ge_{18}^{4-}$ . The $Ni@Ge_9^{3-}$ and $Ni@Ge_9Ni(PPh_3)^{2-}$ ions are proposed monomers of the $Ni_3@Ge_{18}^{4-}$ fused cluster. ....	26
<b>Figure 1.13.</b> The crystal structure of $Pt_2@Sn_{17}^{4-}$ , $Pd_2@Sn_{18}^{4-}$ , $Ni_2@Sn_{17}^{4-}$ , and $(Ni@Sn_8)(\mu\text{-Ge})(Ni@Sn_8)^{4-}$ .....	27
<b>Figure 1.14.</b> Structure of the $[Ge_9\text{-}Ge_9]^{6-}$ dimer, a product of the oxidative coupling of $Ge_9^{4-}$ .....	28
<b>Figure 1.15.</b> Structure of the ${}_{1\infty}[Ge_9]^{2-}$ polymer.....	29
<b>Figure 1.16.</b> Structure of the ${}_{1\infty}[HgGe_9]^{2-}$ polymer .....	30
<b>Figure 1.17.</b> (a) Proposed fluxional process and (b) $^{119}\text{Sn}$ NMR spectrum of the $Sn_9^{4-}$ cluster anion. The first cluster is viewed down the $C_4$ rotational axis. $^{119}\text{Sn}$ NMR data was recorded at 298 K at 186.4 MHz in en.....	31
<b>Figure 1.18.</b> (a) Proposed structure of the platinum-hydride $Pt@Sn_9H^{3-}$ ion along with its (b) $^1\text{H}\{^{119/117}\text{Sn}\}$ , (c) $^1\text{H}$ , and (d) $^1\text{H}\{^{195}\text{Pt}\}$ NMR spectra. ....	34
<b>Figure 1.19.</b> Proposed dynamic scheme for the interconversion between the $\eta^4$ and $\eta^5$ isomers of $Sn_9M(CO)_3^{4-}$ , where $M = \text{Cr}, \text{Mo}, \text{W}$ .....	36
<b>Figure 2.1.</b> Structures of the $E_9M(\text{cod})^{3-}$ cluster anions. ORTEP drawings of the (a) $Sn_9Ir(\text{cod})^{3-}$ ( <b>1</b> ); (b) $Pb_9Ir(\text{cod})^{3-}$ ( <b>2</b> ); (c) $Sn_9Rh(\text{cod})^{3-}$ ( <b>3</b> ) cluster anions (blue = Sn, green = Pb, orange = Ir, light blue = Rh, gray = carbon, white = hydrogen). Thermal ellipsoids are drawn at the 50% probability level. ....	43
<b>Figure 2.2.</b> Structure of the $E_9M(\text{cod})^{3-}$ cluster anions with various bonding groups defined. Group <b>A</b> describes the M-Sn bonds, while groups <b>B</b> and <b>D</b> are Sn-Sn bonds within the upper and lower square plane respectively. Group <b>C</b> is defined as the Sn-Sn bonds that make up the waist of the cluster in between the two planes. Group <b>E</b> of the cluster are the $\eta^4$ Sn-Sn bonds involving the capping Sn atom as illustrated.....	48
<b>Figure 2.3.</b> $^{13}\text{C}$ NMR spectrum for the $[\text{K}(2,2,2\text{-crypt})]_3[\text{Pb}_9\text{Ir}(\text{cod})]\cdot 2\text{en}$ salt. Data were recorded at 300 K at 125.8 MHz in Pyr-d5. ....	52

<b>Figure 2.4.</b> HSQC spectrum for the $[\text{Pb}_9\text{Ir}(\text{cod})]^{3-}$ ( <b>2</b> ). Data was recorded at 300 K at 125.8 MHz in Pyr-d5.....	53
<b>Figure 2.5.</b> $^{119}\text{Sn}$ NMR spectra of the $\text{Sn}_9\text{Rh}(\text{cod})^{3-}$ ( <b>3</b> ). Data was recorded at 298 K at 125.8 MHz in an en/tol solution. The signals with a chemical shift $\delta = +2471.7$ , $-379.5$ , and $-541.7$ ppm possess peak widths at half-height $v_{1/2} = 267$ , 135, and 183 Hz respectively.....	55
<b>Figure 3.1.</b> Preliminary structure of the $[\text{Rh}@\text{Sn}_{12}]^{3-}$ ion ( <b>1</b> ). Thermal ellipsoids drawn at the 50% probability level. ....	66
<b>Figure 3.2.</b> Preliminary structure of the $[\text{Rh}@\text{Pb}_{12}]^{3-}$ ion ( <b>1</b> ). Thermal ellipsoids drawn at the 50% probability level. ....	68
<b>Figure 3.3.</b> $^{207}\text{Pb}$ NMR spectrum for the $[\text{Rh}@\text{Pb}_{12}]^{3-}$ ( <b>2</b> ) ion. Data was recorded at 104.9 MHz from an en solution at room temperature.....	69
<b>Figure 3.4.</b> $^{207}\text{Pb}$ NMR spectrum for the $[\text{Ir}@\text{Pb}_{12}]^{3-}$ ( <b>3</b> ) ion. Data was recorded at 104.9 MHz from an en solution at room temperature.....	70
<b>Figure 3.5.</b> (a) $^{119}\text{Sn}$ , (b) $^{119}\text{Sn}\{^{117}\text{Sn}\}$ , and (c) $^{117}\text{Sn}$ NMR experiments of the $\text{Ir}@\text{Sn}_{12}^{3-}$ ion. $^{119}\text{Sn}\{^{117}\text{Sn}\}$ and $^{117}\text{Sn}$ spectra recorded using a custom-made Quad-inverse probe.....	72
<b>Figure 4.1.</b> Crystal structure of (a) $[\text{Rh}_2\text{H}(\text{PPh}_2)_2(\text{PPh}_3)_3]^-$ and (b) the dirhodium core omitting the phenyl groups for clarity. Thermal ellipsoids are drawn at the 50% probability level.....	82
<b>Figure 4.2.</b> Crystal structure of the $[\text{Co}_3(\text{CO})_7]^{3-}$ carbonyl cluster (blue = Co, red = O, gray = C). The $\text{C}_{3v}$ symmetry is highlighted by views of the cluster (b) down the $\text{C}_3$ axis and (c) perpendicular to the $\text{C}_3$ axis. Thermal ellipsoids are drawn at the 50% probability level.....	86
<b>Figure 4.3.</b> Crystal structure of the $[(\text{C}_3\text{H}_7\text{N}_2\text{O})_3\text{Ir}_4(\text{CO})_9]^{3-}$ carbamoyl cluster. Thermal ellipsoids are drawn at the 50% probability level. ....	91
<b>Figure 4.4.</b> $^{31}\text{P}\{^1\text{H}\}$ NMR spectrum for the $[\text{Rh}_2\text{H}(\text{PPh}_2)_2(\text{PPh}_3)_3]^-$ ion. Data were recorded at 298 K at 202.46 MHz in Pyr. $\delta = 23.5$ ppm ( $^1J(^{31}\text{P}, ^{103}\text{Rh}) = 194$ Hz, $^2J(^{31}\text{P}, ^{31}\text{P}) = 106$ Hz), 29.6 ppm ( $^1J(^{31}\text{P}, ^{103}\text{Rh}) = 208$ Hz), and 197.9 ppm ( $^1J(^{31}\text{P}, ^{103}\text{Rh}) = 156$ Hz, $^1J(^{31}\text{P}, ^{103}\text{Rh}) = 110$ Hz, $^2J(^{31}\text{P}, ^{31}\text{P}) = 106$ Hz).....	94
<b>Figure 4.5.</b> $^{31}\text{P}$ - $^{31}\text{P}$ COSY of the $[\text{Rh}_2\text{H}(\text{PPh}_2)_2(\text{PPh}_3)_3]^-$ ion.....	95

<b>Figure 4.6.</b> $^1\text{H}$ NMR spectrum for $[\text{Rh}_2\text{H}(\text{PPh}_2)_2(\text{PPh}_3)_3]^-$ . Data were recorded at 300 K at 500.1 MHz in Pyr.....	96
<b>Figure 4.7.</b> Phosphido signal in $^{31}\text{P}\{^1\text{H}\}$ NMR (top) and $^{31}\text{P}$ NMR (bottom) spectra for $[\text{Rh}_2\text{H}(\text{PPh}_2)_2(\text{PPh}_3)_3]^-$ . Data were recorded at 300 K at 202.5 MHz in Pyr. Bottom spectrum shows coupling to hydride ligand.....	97
<b>Figure 4.8.</b> Dynamic exchange mechanism scheme for $[\text{Rh}_2\text{H}(\text{PPh}_2)_2(\text{PPh}_3)_3]^-$ ..	97
<b>Figure 4.9.</b> Proposed reaction pathway for the synthesis of $[\text{Rh}_2\text{H}(\text{PPh}_2)_2(\text{PPh}_3)_3]^-$ anions.....	99
<b>Figure 5.1.</b> (a) The High resolution TEM image and (b) X-ray diffraction experiment of ‘as-prepared’ sub-10 nm ordered $\text{PtSn}_4$ nanoparticles ( $\text{PtSn}_4$ 04-0744). The 2.32 Å d-spacing is associated with the 213 facet at 39.7°.....	109
<b>Figure 5.2.</b> Nanoparticle size distribution of $\text{PtSn}_4$ particles.....	109
<b>Figure 5.3.</b> (a) The high-resolution TEM image and (b) X-ray diffraction data of annealed intermetallic $\text{Ir}_3\text{Sn}_7$ nanoparticles. The particles for the TEM experiments were washed with nitric acid to remove the excess Sn ( $\text{Ir}_3\text{Sn}_7$ 00-004-0673).....	110
<b>Figure 5.4.</b> Nanoparticle size distribution of $\text{Ir}_3\text{Sn}_7$ particles.....	110
<b>Figure 5.5.</b> X-ray diffraction experiment of annealed, nitric acid-rinsed intermetallic $\text{Ir}_3\text{Sn}_7$ nanoparticles on XC-72 carbon support ( $\text{Ir}_3\text{Sn}_7$ 00-004-0673).....	111
<b>Figure 5.6.</b> (a) Crystal lattice of $\text{PtSn}_4$ (pink = Pt, blue = Sn); (b) atomic arrangement of Sn atoms about each Pt atom in $\text{PtSn}_4$ ; (c) the $\text{PtSn}_8$ subunit of the $\text{Pt}@_{\text{Sn}_9}\text{Pt}(\text{PPh}_3)^{2-}$ cluster showing the similarity to the structure of $\text{PtSn}_4$ ; (d) the $\text{Pt}@_{\text{Sn}_9}\text{Pt}(\text{PPh}_3)^{2-}$ cluster. <sup>58,170</sup> .....	113
<b>Figure 5.7.</b> (a) Crystal lattice of $\text{Ir}_3\text{Sn}_7$ (green = Ir, blue = Sn); (b) the $\text{Ir}_2\text{Sn}_{12}$ subunit in the $\text{Ir}_3\text{Sn}_7$ crystal lattice; (c) $\text{IrSn}_4$ subunits in $\text{Ir}_3\text{Sn}_7$ ; (d) The $\text{IrSn}_9$ core of the $[\text{Sn}_9\text{Ir}(\text{cod})]^{3-}$ ion; (e) the $[\text{Sn}_9\text{Ir}(\text{cod})]^{3-}$ cluster anion.....	114



## List of Abbreviations

NPs	nanoparticles
PGM	platinum group metal
NMR	nuclear magnetic resonance
Eq	equation
e-	electron
en	ethylenediamine
tol	toluene
dmf	dimethylformamide
THF	tetrahydrofuran
Pyr	pyridine
TEM	transmission electron microscopy
XRD	X-ray diffraction
EDX	energy-dispersive X-ray spectroscopy
2,2,2-crypt	4,7,13,16,21,24-hexaoxa-1,10-diazabicyclo[8.8.8]hexacosane
18-crown-6	1,4,7,10,13,16-hexaoxacyclooctadecane
DPPE	1,2-Bis(diphenylphosphino)ethane
<sup>i</sup> Pr	isopropyl
Cy	cyclohexyl
Ph	phenyl
Mes	mesityl
Bu	butyl
DFT	density functional theory

cod	1,5-cyloocatadiene
ORTEP	Oakridge thermal ellipsoid parameters
ppm	parts per million
hr	hours
min	minutes
abs. coeff.	absorption coefficient
calc	calculated
$\delta$	chemical shift
Hz	hertz
MHz	megahertz
Å	angstrom
ave	average
mmol	millimole
nm	nanometer
mL	milliliter
MGE	main group element

## List of Publications

1. Downing, D. O.; Zavalij, P.; Eichhorn, B. W. “The *closo*-[Sn<sub>9</sub>Ir(cod)]<sup>3-</sup> and [Pb<sub>9</sub>Ir(cod)]<sup>3-</sup> Zintl Ions: Isostructural Ir(I) Derivatives of the *nido*-E<sub>9</sub><sup>4-</sup> Anions (E = Sn, Pb)” *Eur. J. Inorg. Chem.* **2010**, 890-894.
2. Downing, D. O.; Zavalij, P.; Eichhorn, B. W. “Dynamic properties of the fluxional Rh<sub>2</sub>H(μ-PPh<sub>2</sub>)<sub>2</sub>(PPh<sub>3</sub>)<sub>3</sub><sup>-1</sup> complex” *Inorg. Chem. Acta.* **2011**, 375(1), 329-332.
3. Kocak, F.S.; Downing, D.O.; Zavalij, P.Y.; Lam, Y.F.; Vedernikov, A.N.; Eichhorn, B. “The Surprising Acid-Base and Ion-Sequestration Chemistry of Sn<sub>9</sub><sup>4-</sup>: HSn<sub>9</sub><sup>3-</sup>, Ni@HSn<sub>9</sub><sup>3-</sup> and the Sn<sub>9</sub><sup>3-</sup> Ion Revisited” *J. Am. Chem. Soc.* *Accepted for publication.*
4. Downing, D. O.; Liu, Z.; Eichhorn, B. W. “Formation and catalytic properties of ordered and disordered PtSn<sub>4</sub> nanoparticles through controlled cluster oxidation” *Chemistry of Materials. Revision under consideration.*
5. Downing, D. O.; Zavalij, P.; Eichhorn, B. W. “The Isolation of the Rh@Sn<sub>12</sub><sup>3-</sup> and Rh@Pb<sub>12</sub><sup>3-</sup> Icosahedral Zintl ions and NMR studies of Rh@Pb<sub>12</sub><sup>3-</sup>, Ir@Pb<sub>12</sub><sup>3-</sup>, Ir@Sn<sub>12</sub><sup>3-</sup>” *In preparation.*
6. Downing, D. O.; Zavalij, P.; Eichhorn, B. W. “*Closo*-[Sn<sub>9</sub>Rh(cod)]<sup>3-</sup> and [Rh@Sn<sub>10</sub>]<sup>3-</sup> clusters: The first rhodium-substituted stannide Zintl Ions.” *In preparation.*
7. Downing, D. O.; Zavalij, P.; Eichhorn, B. W. “The Synthesis of the [(C<sub>3</sub>H<sub>7</sub>N<sub>2</sub>O)<sub>3</sub>Ir<sub>4</sub>(CO)<sub>9</sub>]<sup>3-</sup> Ion: A New Iridium Carbamoyl.” *In preparation.*

8. Downing, D. O.; Zavalij, P.; Eichhorn, B. W. “The Synthesis of  $\text{Co}_3(\text{CO})_7^{3-}$  via the Use of the  $\text{As}_7^{3-}$  Zintl ion as an Electron Transfer Reagent.” *In preparation.*
9. Downing, D.O.; Eichhorn, B. W. “Ni/As Binary Phase Nanoparticles from Zintl Anions” *In preparation.*

# Chapter 1: Introduction

## 1.1. Introduction to Zintl Clusters and their Relationship to Nanoparticles

Zintl ions are polyanions of main group elements (MGE), primarily of the heavier elements of groups 14 and 15 (e.g.  $\text{Sn}_9^{4-}$ ,  $\text{Pb}_9^{4-}$ ,  $\text{As}_7^{3-}$ ,  $\text{Sb}_7^{3-}$ ). Zintl clusters have been known for over 100 years, and there has been significant recent interest in this area due to the unique chemistry and novel properties of these ions. Recent synthetic studies have focused on reactions with transition metal precursors to give bimetallic Zintl clusters. The rising number of bimetallic Zintl clusters are composed of polyhedral frameworks (e.g.  $\text{Pt@Pb}_{12}^{2-}$ ,  $\text{Pd}_2\text{@Sn}_{18}^{4-}$ ). The synthesis and characterization of these Zintl cluster transition metal derivatives<sup>1-4</sup> have been of particular interest to the growing field of nanotechnology. As such, in this thesis, I describe my studies mainly on the synthesis of new bimetallic Zintl clusters and their use in the fabrication of highly-ordered nanoparticles previously inaccessible by other methods.

This research involves the synthesis, characterization and applications of Zintl clusters, which are small, molecular clusters. We show that Zintl clusters are excellent precursors to small (<15 nm), uniform nanoparticles (NPs) that cannot be formed by other means. Clusters are generally no larger than 1 nm, and represent the transition from molecules to nanoparticles. Clusters have monodisperse size distributions compared to nanoparticles, having a discrete number of atoms. This monodispersity separates clusters from NPs, which always have a certain degree of polydispersity. Controlling the size and

stoichiometry of NPs is critical in nanoscience because the various characteristics of the solid-state materials (*e.g.* optical, magnetic, catalytic, etc.) are highly compositionally, structure, and size-dependent.<sup>5</sup> Monodispersity among NPs is therefore crucial in eliciting consistent, uniform chemical and physical properties.

Despite their importance, much is still unknown about the structure, stability, and dynamic properties of small NPs; more specifically, NPs containing two or more elements. Nanostructures are typically no larger than 10 nm in diameter, oriented in a manner such that one spatial dimension is no longer than 100 nm.<sup>6,7</sup> Nanomaterials can be made in the form of the so called zero-dimensional nanocrystals or nanoparticles, 1D nanowires and nanotubes, or 2D nanofilms and nanowalls.<sup>7</sup> These materials can be synthesized via numerous methods including transition metal salt reduction, thermal decomposition and photochemical techniques, organometallic ligand reduction and displacement, metal vapor synthesis, and electrochemical methods.<sup>6</sup>

It is of particular importance to control the growth of NPs, especially bimetallic NPs. As the size composition, structure, and shape of the particles affect their functionality in applications, controlling the size of a particle and the uniformity in a sample of particles is important. Reproducibly controlling the characteristics of multicomponent NPs has shown to be an arduous task.<sup>8</sup> There are three major synthetic issues affecting this control including 1) co-reduction, 2) annealing, and 3) metal immiscibility. The co-reduction of metals is a common means of synthesizing bimetallic NPs but the method makes it intrinsically difficult to control particle size and composition. The reduction of the metal precursors occurs at different rates, which then leads to heterogeneous materials.






Secondly, annealing is a tool utilized to improve NP uniformity that unfortunately generates large NPs. Lastly, the immiscibility of certain metals (i.e. AlSn, CoCu) makes the formation of solid state alloys NP very difficult. The Zintl cluster precursors described herein provide an important advantage in the synthesis of bimetallic NPs.

The synthesis of small, uniform NPs can be promoted by the synthesis of relatively stable clusters. Such materials can be synthesized if close packed structures are synthesized, which promotes maximum metal-metal bonding and therefore maximizes cluster stability.<sup>8,9</sup> The regular packing of metal atoms around a central atom gives the cluster a regular form adopting a full shell when a magic number of atoms is present in the shell of a cluster. Such magic clusters can be represented by  $M_x$  where the number of atoms in each shell,  $y$ , is defined by:

$$y = 10n^2 + 2 \quad 1.1$$

where  $n$  is the number of shells in the cluster. Each magic cluster contains  $x$  metal atoms where  $x$  is the sum of the atoms in each shell and the central atom. The first magic cluster therefore contains the central atom and 12 surrounding atoms to give the magic number  $M_{13}$  (1+12). The second magic cluster has 42 atoms the second shell according to Eq. 1.1, and therefore has 55 total metal atoms (42+13). As a result it is beneficial to synthesize clusters of size  $M_{13}$ ,  $M_{55}$ ,  $M_{147}$ ,  $M_{309}$ ,  $M_{561}$ ,  $M_{923}$ ,  $M_{1415}$  etc., as illustrated in Figure 1.1.<sup>6</sup> Iridium NPs have been synthesized by Watzky and Finke having a magic number of metal atoms as  $Ir_{147}$ ,  $Ir_{309}$ , and  $Ir_{561}$ .<sup>8</sup> Other metallic clusters with ligands have been synthesized

with full shells such as  $\text{Au}_{55}(\text{PPh}_3)_{12}\text{Cl}_6$ .<sup>10</sup> The work described herein will provide fundamental advances in the area of cluster science, giving tangible examples of “magic” clusters  $\text{M}@E_{12}$  ( $\text{M} = \text{Rh}, \text{Ir}; \text{E} = \text{Sn}, \text{Pb}$ ; see Chapter 3) that have been the subject of many theoretical studies and models.<sup>11</sup> The novel isolated clusters join the rare class of isolated plumbaspherene and stannaspherenes, discussed in Section 1.3.2.

Full-Shell "Magic Number" Clusters					
Number of shells	1	2	3	4	5
Number of atoms in cluster	$\text{M}_{13}$	$\text{M}_{55}$	$\text{M}_{147}$	$\text{M}_{309}$	$\text{M}_{561}$
Percentage surface atoms	92%	76%	63%	52%	45%

**Figure 1.1.** Hexagonal close-packed clusters with a magic number of atoms (taken from reference [6]).

A lesser explored solution to gaining control over particle size is to first gain control over the mechanisms governing NP formation. Similar to other synthetic methods, knowing the growth mechanism can provide control over structure, composition, and particle sizes. The synthesis, characterization, and applications of very large bimetallic nanoclusters can provide insight into this critical issue. Bimetallic Zintl clusters in particular are of interest due to their unique properties as well as to their structural similarity to small nanoclusters and NPs. This thesis describes the fabrication of intermetallic NPs via the oxidation of both previously isolated and novel bimetallic Zintl clusters (see Chapter 5). Intermetallic materials, such as alloys, are composed of at least two different



metals, but intermetallic phases differ in the degree of atomic order present in their crystal structures. Alloys tend to adopt the crystal lattice of one of the metals in the NP, while their intermetallic counterparts possess crystal lattices independent of either metal. Although NP growth mechanisms are still not understood, this work aims to correlate the strong atomic level structural similarities of the Zintl precursors to the anti-prismatic  $M\text{Sn}_8$  subunits that define the respective intermetallic crystal lattices. The commonality of the structural features allows the facile isolation of intermetallic NPs that are still inaccessible via any other method to date.

Zintl clusters therefore essentially bridge the gap between large molecular clusters and small NPs. Zintl clusters are in a position of size where they can be characterized by the same means as molecules, such as NMR spectroscopy and X-ray crystallography. Zintl clusters sometimes exhibit delocalized electronic character<sup>12</sup> and possess high coordination numbers (6-12) in the case of the endohedral bimetallic clusters,<sup>13</sup> giving them NP-like structures in this regard. Exploring this area of chemistry has provided insight about NP stability and the mobility of the atoms on the surface of NPs. It is possible that there is a continuum of Zintl cluster sizes that start from smaller 4-atom clusters up to larger clusters approaching the size of NPs. The advantage of having the ability to characterize the complexes via X-ray crystallography and nuclear magnetic resonance (NMR) spectroscopy can allow for information to be gleaned about the structure and atomic mobility of small NPs of comparable composition as the size of the Zintls increases, though we are far from these analyses. Building a larger,

diverse library of Zintl clusters will likewise provide a better understanding of the structure-bonding relationships of these clusters via their characterization and explain the chemical reactivity of these anionic metal centers. Additionally, increasing the diversity of known bimetallic Zintl clusters will provide a compilation of precursors from which a new set of intermetallic NPs can be accessed for the first time, with a potential set of viable properties.

In the coming sections the chemistry of Zintl cluster anions, bimetallic Zintl cluster derivatives, and highly ordered NPs are reviewed.

## 1.2. Zintl Ions

The first group 14 “Zintl” cluster was observed in the late 19<sup>th</sup> century when Joannis discovered that intense colored solutions can be made upon dissolving Pb metal in an alkali metal-ammonia solution.<sup>14,15</sup> Green solutions were observed after the reaction of sodium and excess lead as well as a precipitate. The composition of the precipitates were found to be NaPb<sub>4</sub> and NaPb<sub>2</sub> under different experimental conditions. It is now known that anionic Pb<sub>9</sub><sup>4-</sup> was generated in these experiments, one of the common nine-atom atomic clusters of the group 14 main group metals, although they were not identified at the time.

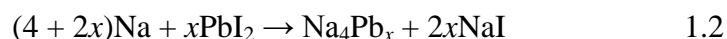
In 1907, Kraus and coworkers were able to show that the precipitated species were a plumbide salts that dissociate in ammonia, producing anionic metal species. This finding was determined through electrochemical studies in which the green solution was shown to be an electrolyte that precipitated Pb metal onto a

cathode, indicative of a negatively charged lead cluster.<sup>16</sup> From the precipitate, a 2 mole equivalent of lead per  $e^-$  was estimated to be deposited leading Kraus to characterize the salt as  $Na^+$  and  $Pb_2^-$  ions. Tin, another member of group 14 behaved similarly under the same reaction conditions. Additionally, Kraus was successful in showing that lead has similar reactivities with potassium metal and that tin reacts to give highly colored red solutions in liquid ammonia.

Further advancements were made by Smyth via solubility studies and the continued use of electrochemistry.<sup>17</sup> These studies showed that about 2.26 lead atoms could be dissolved in ammonia for every atom of sodium present in solution. The more precise measurement lead Smyth to believe that the solution was more complicated than first expected, proposing that an equilibrium between the  $Pb_2^-$  and  $Pb_3^-$  ions was taking place. Considering these studies as well as those by Peck showing that up to 4.0 and 2.33 atoms of tellurium and antimony respectively could be dissolved in ammonia solutions per atom of sodium,<sup>18</sup> Kraus later proposed that the observed anions were in the form of  $Na_4Pb_8 \bullet Pb$ ,  $Na_3Sb_6 \bullet Sb$ , and  $Na_2Te_3 \bullet Te$  salts, which are all correct stoichiometries.<sup>18,19</sup>

Polyanions of this type were termed Zintl ions after Eduard Zintl, a German chemist who made seminal contributions to the field.<sup>20-23</sup> Initial studies by the Zintl group were on the previously reported metal-sodium solutions in the 1930s. Potentiometric titrations were an important facet of the group's study, allowing them to come to the oxidation state of sodium and metal in the ammonia solutions.<sup>21</sup> An ammonia sodium solution was titrated using main-group salts such as  $PbI_2$  and  $BiI_3$ , as it was extremely time consuming to react the elemental

metals or metalloids with sodium solutions. Upon the addition of the main-group metallic salt to the sodium solution, the metal cation would be reduced to elemental form. This metal would then dissolve and further reduce to its anionic form, until precipitation began, following Eq. 1.2.<sup>20,22</sup> The titrations were used to measure the oxidation of the sodium and metal up until the onset of metal precipitation. Anions with the formulas  $E_9^{-4}$  (E = Sn, Pb),  $E_7^{-3}$  (E = Sb, Bi), and  $E_5^{-3}$  (E = As, Bi), were determined to be present, though the structural geometry of the anions could not be determined at the time.<sup>23</sup>



The solid state structures of these salts were not determined for another 45 years, where it was showed that many of these species are high symmetry, ligand-free clusters built on polyhedral cage-like structures. Zintl ions were first isolated as crystals in 1970 by Kummer and Diehl, giving low resolution crystal structures of  $\text{Na}_4(\text{en})_7\text{Sn}_9$ .<sup>24</sup> The crystallization of the salt was facilitated by the addition of tetrahydrofuran in the ethylenediamine (en) solution of the salt.

The next major find in the field came with the use of sequestering agents to facilitate crystallization and exploit the reactivity of these naked polyanionic clusters. As cryptands, a family of polycyclic ligands, were shown to increase alkali metal solubility in solution and able to sequester metal cations, Corbett and coworkers proposed utilizing these compounds as a sequestering agent to isolate Zintl ions in 1976.<sup>25-28</sup> Cryptands also prevent the anionic clusters from reverting back to the Zintl phase. The cryptand utilized in the study was 1,10-diaza-

4,7,13,16,21,24-hexaoxabicyclo[8.8.8]hexacosane, currently more commonly known as 2,2,2-crypt, depicted in Figure 1.2. Cryptands are excellent sequestering agents due to the 3 dimensional cavity of the structure which can host cations. This supramolecular host-guest interaction is stabilized by charge-dipole moment intermolecular force and is entropically driven due to the decrease in ion solvation in the presence of the sequestering agent.<sup>29</sup> Additionally, cluster crystallization is facilitated by the use of cryptands due to the relatively large size of the  $[A(2,2,2\text{-crypt})]^+$  cation (A = alkali metal), compared to free alkali metals, which allows more efficient packing with the large cluster anions.

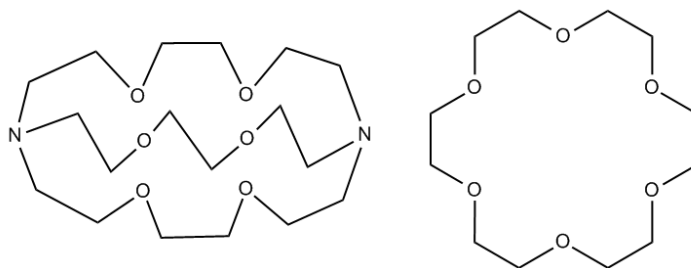


**Figure 1.2.** Structure of 2,2,2-crypt (left) and 18-crown-6 (right), two important sequestering agents in Zintl cluster chemistry.

Once 2,2,2-crypt was employed as an appropriate sequestering agent, Corbett and coworkers were able to isolate Zintl structures allowing them to obtain higher resolution crystal structures of these polyanions.<sup>28</sup> The  $Sb_7^{3-}$  cluster was characterized extensively, described as a  $C_{3v}$  cluster illustrated in Figure 1.3.

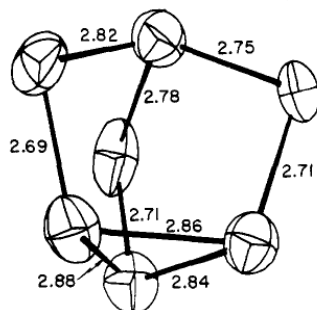


**Figure 1.3.** ORTEP drawing of  $C_{3v}$   $Sb_7^{3-}$  cluster in  $[Na-crypt]_3Sb_7$  (taken from reference [28]).

Due to the success of crypt as a sequestering agent, other ligands known as crown ethers have also been employed in isolating Zintl clusters. Crown ethers are heterocyclic compounds with successive ether linkages that bind to cations much like in the manner of cryptands. The commonly used 1,4,7,10,13,16-hexaoxacyclooctadecane, or 18-crown-6 is shown in Figure 1.2. Though relatively successful, crown ethers do not hold cations as tightly as cryptands. Nonetheless, the use of cryptands and crown ethers have led to the structure determination of various clusters such as  $E_5^{2-}$  ( $E = Si, Ge, Sn, Pb$ ),<sup>30-33</sup>  $E_9^{n-}$  ( $E = Si, Ge, Sn, Pb, n = 3,4$ ),<sup>32,34-37</sup>  $E_9^{2-}$  ( $E = Si, Ge$ ),<sup>36,38</sup>  $E_7^{3-}$  ( $E = P, As, Sb$ ),<sup>28,39,40</sup>  $E_{11}^{3-}$  ( $E = As, Sb$ ),<sup>41,42</sup>  $E_4^{2-}$  ( $E = As, Sb$ ),<sup>43,44</sup> and the  $Bi_2^{2-}$  ion<sup>45</sup> to name several (Figure 1.4).<sup>3</sup>

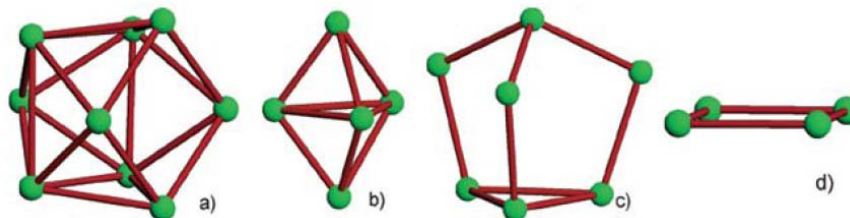


**Figure 1.4.** Atomic structures of select homoatomic main-group anionic clusters. (a)  $E_9^{3-}$  and  $E_9^{4-}$  (b)  $E_5^{2-}$  (c)  $As_7^{3-}$  and  $Sb_7^{3-}$  (d)  $Sb_4^{2-}$  and  $Bi_4^{2-}$  (taken from reference [3]).

The polyanions of groups 14 and 15 are quite different, with the group 14 tetrel anions conforming to borane-like geometries while the group 15 pnictogens are hydrocarbon-like.<sup>43,46</sup> The pnictogens form polycyclic structures with localized 2-center 2e- bonds; E and E<sup>-</sup> are therefore electronically equivalent to CH and CH<sub>2</sub> groups, respectively. The tetrrels, however, possess polyhedral cluster shapes with delocalized bonds holding their frameworks together.<sup>3,47</sup> Bonds between metal atoms in these structures are not simply composed of 2-center 2e- bonds because the clusters are electron-deficient, and the skeletal-bonding electrons in the system are delocalized over the entire cluster instead of having localized  $\sigma$ -bonds throughout.

Due to an electron-deficiency, group 14 Zintl anions take on the structural and electronic characteristics of the isoelectronic boranes. Boranes are binary boron compounds and were first isolated by Alfred Stock.<sup>48</sup> The simplest of these molecules is the boron hydride diborane B<sub>2</sub>H<sub>6</sub>, though higher structured boranes take on cage-like structures, reminiscent of the Zintls.<sup>47,48</sup> Borane structures cannot be predicted by Lewis structures, but more successfully described by Wade's rules, which correlates the number of electrons in a system to the shape of the borane, developed in the 1970s by Kenneth Wade. The rules are summarized below in Table 1.1.<sup>48</sup>

**Table 1.1.** Tabulation of Wade's Rules for the Boranes.<sup>48</sup>

Type	Formula	Skeletal e <sup>-</sup> Pairs	Borane Examples
<i>Closo</i>	[B <sub>n</sub> H <sub>n</sub> ] <sup>2-</sup>	n + 1	[B <sub>6</sub> H <sub>6</sub> ] <sup>2-</sup> , [B <sub>12</sub> H <sub>12</sub> ] <sup>2-</sup>
<i>Nido</i>	B <sub>n</sub> H <sub>n+4</sub>	n + 2	B <sub>2</sub> H <sub>6</sub> , B <sub>5</sub> H <sub>9</sub> , B <sub>6</sub> H <sub>10</sub>
<i>Arachno</i>	B <sub>n</sub> H <sub>n+6</sub>	n + 3	B <sub>4</sub> H <sub>10</sub> , B <sub>5</sub> H <sub>11</sub>
<i>Hypho</i>	B <sub>n</sub> H <sub>n+8</sub>	n + 4	None

The triangular-faced structures are termed deltahedra and are characterized by the number of vertices  $n$  present in the structure as well as the number of cluster-bonding electrons present. By Wade's rules, boranes of the structure  $[\text{B}_n\text{H}_n]^{2-}$  are said to have a *closo* deltahedral structures, a term derived from the Greek word for cage. These structures have a boron atom at each vertex and no bridged B-H-B bonds in the complex. Example anions include octahedral  $[\text{B}_6\text{H}_6]^{2-}$  and icosahedral  $[\text{B}_{12}\text{H}_{12}]^{2-}$  (Figure 1.5a), two structures with regular geometries. The *closo* structures possess  $n+1$  framework electron pairs, and therefore  $2n+2$  skeletal bonding electrons. The number of electrons is derived as follows:

1. Each  $[\text{B}_n\text{H}_n]^{2-}$  cluster has a **total** electron count of  $4n+2$  (each B =  $3e^-$ , each H =  $1e^-$ , charge =  $2e^-$ ).
2. This electron count equates to  $2n+1$  **total** bonding pairs.
3. *Closo* boranes exclusively contain terminal B-H bonds, and thus  $n$  bonding pairs are required for these bonds.
4. Therefore,  $n+1$  of the bonding pairs remain to form delocalized bonds within the cluster frameworks, giving  $2n+2$  **skeletal** bonding electrons.

The group 14 Zintl polyhedra are isoelectronic to corresponding borohydride structures, in which each tetrel atom, E, is equivalent to a B-H group. Each E donates has a lone pair and donates its remaining  $2e^-$  to the cluster framework for skeletal bonding. The charge on the borane clusters is not related to  $n$ , therefore each borohydride  $[\text{B}_n\text{H}_n]^{2-}$  theoretically has a related Zintl cluster,



$[E_n]^{2-}$ .<sup>48,49</sup> Transition metal derivatives of the *closo*- $[Pb_{10}]^{2-}$  and  $[Pb_{12}]^{2-}$  clusters will be discussed in Section 1.3.2 and novel *closo* icosahedra will be presented in Chapter 3 of this thesis.

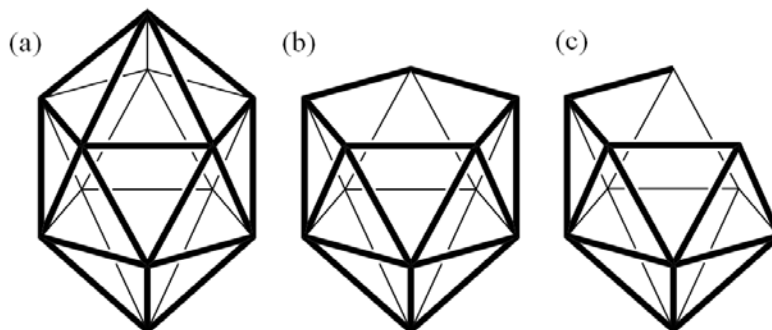


**Figure 1.5.** Example of idealized *closo*, *nido*, and *arachno* boranes highlighting the structure associated with the nomenclature. Structures of (a) *closo*- $B_{12}H_{12}^{2-}$  and  $E_{12}^{2-}$ , (b) *nido*- $B_{11}H_{15}$  and  $E_{11}^{4-}$ , (c) *arachno*- $B_{10}H_{16}$  and  $E_{10}^{6-}$  (borane hydrogens omitted).

*Nido*, *arachno*, and *hypo* structures differ from the cage-like *closo* type in that one, two, and three vertices are removed from the cage respectively in systems with equivalent bonding skeletal orbitals (Figure 1.5). *Nido*, Latin for nest, corresponds to boranes of the structure  $B_nH_{n+4}$ .<sup>48,49</sup> The term *Arachno* is Greek for spider is used to describe the cage structures missing two vertices, as when certain vertex combinations are missing the clusters may look like a spider web. The term *Arachno* corresponds to the boranes of the  $B_nH_{n+6}$  structure type. Example boranes *nido*- $B_{11}H_{15}$  and *arachno*- $B_{10}H_{16}$  are illustrated in Figure 1.5b-c for comparison to the more cage-like *closo*- $B_{12}H_{12}^{2-}$ .

The structure of the group 14 Zintl clusters can be predicted for clusters of a given size and charge and be designated as *closo*, *nido*, *arachno*, or *hypo* in nature. Ligand free group 14 clusters have the formulas  $[E_n]^{2-}$ ,  $[E_{n-1}]^{4-}$ ,  $[E_{n-2}]^{6-}$ ,

and  $[E_{n-3}]^{8-}$  for *closo*, *nido*, *arachno*, and *hypho* respectively.<sup>49</sup> As stated, *nido* clusters are analogous to the removal of a vertex site on a *closo* structure. Upon the removal of a vertex, 2e<sup>-</sup> are removed from the cluster in the case of the tetrels. In order to fill all bonding orbitals of the cluster, two extra electrons must be added, thus giving the above changes in relative cluster charge. It is important to note that in the case of these formulas *n* is an arbitrary value, so the formulas can be simplified to  $[E_n]^{2-}$ ,  $[E_n]^{4-}$ ,  $[E_n]^{6-}$ , and  $[E_n]^{8-}$  respectively.<sup>49</sup> Transition metal derivatives of the *nido*-Ge<sub>9</sub><sup>4-</sup>, Sn<sub>9</sub><sup>4-</sup>, and Pb<sub>9</sub><sup>4-</sup> clusters will be discussed in Section 1.3.1 and novel substituted Sn<sub>9</sub><sup>4-</sup> and Pb<sub>9</sub><sup>4-</sup> clusters will be discussed in Chapter 2.

As implied by the  $[E_n]^{2-}$ ,  $[E_n]^{4-}$ , and  $[E_n]^{6-}$  formulas for *closo*, *nido*, and *arachno* group 14 Zintl ions, the charge on group 14 MGE clusters is independent of cluster size. Despite this, no homoatomic tetrels with over nine Group 14 atoms have been isolated. As noted by Fässler and Hoffmann, this may be a result of the instability caused by building larger cavities within the cluster cages.<sup>13</sup> Another issue is likely due to the lack of  $\sigma$ -bonding stabilization compared to the stronger fullerenes that contain  $\pi$ -bonds. Unlike the fullerenes that utilize extensive  $\sigma$ -bonding, Zintl ions are held together primarily by delocalized bonds, allowing high fluxionality within the polyanions.<sup>50</sup> While increasing the size of these anions may not give instability due to increased charge, making large structures with a weak frame is not favorable. Bimetallic cluster anions have been targeted as it has been shown that encapsulated transition metals in particular are able to increase the stability of the larger isolated Zintl clusters.<sup>13</sup> The electron count of bimetallic Zintl clusters possessing vertex and endohedral transition metal centers

have an additional TE-12 and TE-10 electrons, respectively, where TE is the transition metal's electron count, including those due to donation by any ligands present on the metal center.

Zintl cluster chemistry is currently being studied on several fronts. As a bridge between molecules and NPs, it is of interest to investigate whether there is a continuum of cluster sizes and to fabricate small, ordered NPs from these clusters. This therefore requires an additional source of stabilization to first isolate larger clusters.

### 1.3. Transition Metal Derivatives of Zintl Ions

Bimetallic Zintl clusters are of interest due to their unique structures and properties as well as to their similarity to small nanoclusters and fullerenes.<sup>13</sup> Particularly interesting is the ability for both fullerenes and Zintl clusters to form endohedral structures<sup>13,51</sup> in which the centered elements are in highly symmetric coordination geometries (*e.g.* the  $I_h$  symmetries of La and Pt in La@C<sub>60</sub> and [Pt@Pb<sub>12</sub>]<sup>2-</sup>).<sup>52,53</sup> The lack of structure stability of the non-endohedral frameworks at these size regimes makes the isolation of larger clusters difficult, but it has been shown that the presence of an encapsulated atom or ion within these cluster structures can increase their stability. There are numerous bimetallic clusters such as M@E<sub>12</sub><sup>2-</sup> (M = Ti, V, Cr, Fe, Co, Ni, Cu, Y, Nb, Gd, Hf, Ta, Pt, Au; E = Sn, Pb) and AlE<sub>n</sub><sup>+</sup> (E = Si, Ge, Sn, Pb; n = 5-12) that for the most part have only been detected in the gas phase by Wang, Lievens, and others.<sup>54-56</sup>

Recently much focus has been geared towards isolating a diverse set of crystalline Zintl clusters. The isolation of these cluster ions is critical to their characterization and to the understanding of the chemistry of these ions. Cluster isolation allows the observation of solution dynamics (Section 1.4), crystal structure determination, and the study of cooperative effects (*e.g.* magnetic coupling, band formation, etc.) in assembled clusters. Below is a summary of various group 14 Zintl clusters isolated and characterized to date.

### ***1.3.1. E<sub>9</sub>-Zintl Cluster Transition Metal Derivatives***

Zintl clusters are potentially precursors to access a new class of catalytic PGM NPs, and it is therefore necessary to first isolate various bimetallic Zintl cluster precursors from which these NPs can be fabricated. Large clusters are also desirable for cluster assembled nanomaterials (Section 1.3.2); and while 9-vertex and 10-vertex clusters are known with and without interstitial atoms, structures with more than 10 vertices are expected to have interstitial atoms when prepared in solution or the solid state.<sup>13</sup> This notion currently holds true, with the largest of the known stannides encapsulating at least one transition metal center. As a result, it is of interest to synthesize smaller bimetallic E<sub>9</sub> clusters (E = group 14 element) that could allow for the systematic increase of Zintl cluster sizes.

Bimetallic Zintl clusters are synthesized via the reaction of the E<sub>9</sub><sup>4-</sup> (E = Ge, Sn, Pb) parent ions in the presence of crypt with their respective transition metal precursors. Many of the metal precursors possess labile ligands (*i.e.* PPh<sub>3</sub>, CO, C<sub>6</sub>H<sub>3</sub>(CH<sub>3</sub>)<sub>3</sub>, and 1,5-cyclooctadiene) to facilitate ligand displacement. The

first bimetallic Zintl cluster was prepared by Rudolph and co-workers in 1983.<sup>57</sup>  $K_4Sn_9$  and  $K_4Pb_9$  ethylenediamine solutions were reacted with a 1 mole equivalent of  $Pt(PPh_3)_4$  (with respect to  $E_9^{4-}$ ) to give a product detectable by  $^{31}P$  and  $^{119}Sn$  or  $^{207}Pb$  NMR spectroscopy, although the structure is not known. The product, often referred to as Rudolph's compound, has not been isolated, but NMR spectroscopy suggests a  $[Sn_9Pt(PPh_3)_x]^{4-}$  cluster, where an unknown number of triphenylphosphine units are present. The reaction of  $Sn_9^{4-}$  with  $Pt(PPh_3)_4$  in a 1:2 ratio in the presence of crypt leads to  $Pt@Sn_9Pt(PPh_3)^{2-}$  ions<sup>58</sup> (Eq. 1.3) instead of Rudolph's compound. Triphenylphosphine and hydrogen gas are products of the reaction along with the *nido*- $Pt@Sn_9Pt(PPh_3)^{2-}$  cluster.



Since Rudolph's efforts, various clusters have since been isolated and studied via NMR spectroscopy and X-ray crystallography. Most of these complexes can be described as derivatives of Wade-Mingos type deltahedral clusters.<sup>59,60</sup> Eichhorn and coworkers reported the synthesis and characterization of the first isolated bimetallic Zintl cluster, the  $[Sn_9Cr(CO)_3]^{4-}$  cluster anion in 1988.<sup>61</sup> In 2001, the complex was characterized by  $^{119}Sn$  NMR along with new molybdenum and tungsten analogues, by Eichhorn and Schrobilgen.<sup>62,63</sup> The different complexes can be described as the  $[K(2,2,2-crypt)]^+$  salts  $\eta^4$ - $[Sn_9M(CO)_3]^{4-}$  and  $\eta^5$ - $[Sn_9M(CO)_3]^{4-}$  ( $M = Cr, Mo, W$ ), where the tungsten analogue has been crystallographically characterized as existing in the  $\eta^5$  form (Figure 1.6). The  $\eta^4$  cluster type corresponds to the isomer in which the  $M(CO)_3$

unit is situated on an apical position of the *closo* bicapped square antiprismatic cluster cage, whereas in the  $\eta^5$  isomer the metal is along the waist of the bicapped square antiprism. The  $\eta^4$  and  $\eta^5$  tungsten derivatives co-crystallize in varying ratios of roughly 30-60%  $\eta^5$ , as measured via infrared spectroscopy. Evidence of the interconversion from  $\eta^4$  to  $\eta^5$  the isomer in solution has been evidenced and will be described in section 1.4.

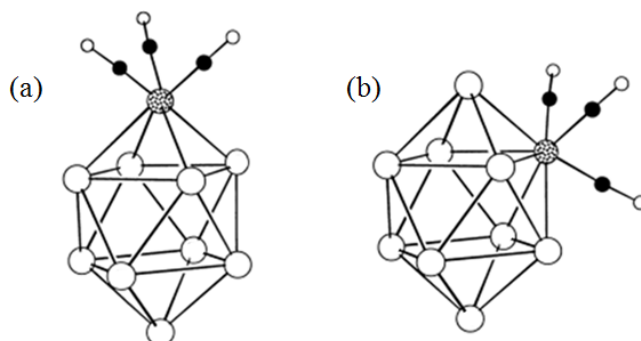


**Figure 1.6.** The (a)  $\eta^4$  (b) and  $\eta^5$  structural isomers of the *closo*- $[\text{Sn}_9\text{M}(\text{CO})_3]^{4-}$  clusters, where  $\text{M} = \text{Cr}, \text{Mo}, \text{W}$ . The tungsten cluster has been characterized crystallographically in the both isomeric forms (taken from reference [62]).

The  $\eta^4$  type structure is the typical atomic arrangement for many of the bimetallic  $\text{E}_9\text{ML}_n$  Zintl clusters isolated thus far, including  $[\text{Pb}_9\text{Mo}(\text{CO})_3]^{4-}$ ,<sup>64</sup>  $[\text{Ge}_9\text{CuPR}_3]^{3-}$  ( $\text{R} = \text{}^i\text{Pr}, \text{Cy}$ ),<sup>65</sup>  $\text{Ni}@\text{Sn}_9\text{Ni}(\text{CO})^{3-}$ ,<sup>58</sup>  $[\text{Ge}_9\text{Ni}(\text{CO})]^{3-}$ ,<sup>66</sup>  $[\text{Ge}_9\text{PdPPh}_3]^{3-}$ ,<sup>67</sup>  $[\text{E}_9\text{ZnR}]^{3-}$  ( $\text{E} = \text{Si}, \text{Ge}, \text{Sn}, \text{Pb}, \text{R} = \text{C}_6\text{H}_5, \text{}^i\text{Pr}, \text{mes}$ ),<sup>68,69</sup> and  $\text{E}_9\text{CdR}$  ( $\text{E} = \text{Sn}, \text{Pb}, \text{R} = \text{C}_6\text{H}_5, \text{SnBu}_3$ )<sup>70</sup> to name several. The former most also exists as the  $\eta^5$  isomer, while  $\text{Ni}@\text{Sn}_9\text{Ni}(\text{CO})^{3-}$  has an interstitial nickel atom in the center of the cluster cage.

There are a number of clusters that deviate from the  $\text{C}_{4v}$  symmetry associated with the typical  $\eta^4$  bonding model, presumably due to steric and electronic effects. Additional  $\text{E}_9$  endohedral clusters that have been isolated

include the  $\text{Cu@E}_9^{3-}$  ( $E = \text{Sn, Pb}$ ),<sup>71</sup>  $\text{Ni@Sn}_9^{4-}$ ,<sup>72</sup>  $\text{M@SnH}_9^{3-}$  ( $M = \text{Ni, Pd, Pt}$ ),<sup>73,74</sup>  $\text{Pd@Sn}_9\text{SnCy}_3^{3-}$ ,<sup>75</sup>  $\text{Pd@Sn}_9\text{PdSnCy}_3^{3-}$ ,<sup>75</sup> and  $\text{Pt@Sn}_9\text{Pt}(\text{PPh}_3)^{2-}$  ion (synthesis described above).<sup>58</sup> Several of these cluster frameworks are illustrated in Figure 1.7.<sup>2</sup>

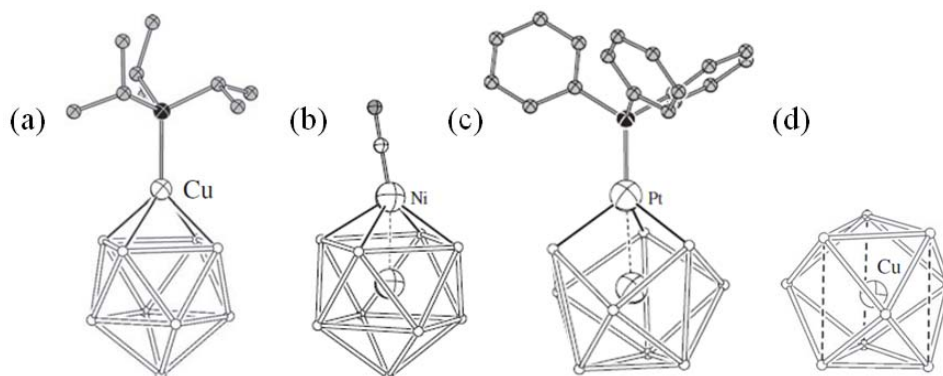


**Figure 1.7.** Various  $E_9$ -transition metal derivative structure types. The  $\text{Ge}_9\text{CuP}(\text{iPr})_3^{3-}$ ,  $\text{Sn}_9\text{Ni}_2\text{CO}^{3-}$ ,  $\text{Sn}_9\text{Pt}_2\text{PPh}_3^{2-}$ , and  $\text{Cu@Sn}_9^{3-}$  clusters possess the same framework as other (a) *closo*- $E_9\text{ML}$   $C_{4v}$ , (b) *closo*- $M@E_9\text{ML}$   $C_{4v}$ , (c) *closo*- $M@E_9\text{ML}$   $C_{3v}$ , and (d)  $M@E_9$  Zintl clusters respectively (taken from reference [2]).

The  $\text{Pt@Sn}_9\text{Pt}(\text{PPh}_3)^{2-}$  cluster is similar structurally to the  $D_{3h}$   $\text{Sn}_9^{2-}$  ion, as shown in Figure 1.8.<sup>58</sup> Both cluster cages can be described as regular tricapped trigonal prisms, where the platinum derivative has an interstitial platinum as well as the bridging ligated platinum group. The  $\text{Ni@Ge}_9\text{Ni}(\text{PPh}_3)^{2-}$  ion has the same geometry as  $\text{Pt@Sn}_9\text{Pt}(\text{PPh}_3)^{2-}$  despite the  $\text{Ni@Sn}_9\text{NiCO}^{3-}$  tin-carbonyl analogue adopting the traditional  $C_{4v}$  framework (Figure 1.7b). The  $\text{Cu@E}_9^{3-}$  ( $E = \text{Sn, Pb}$ ),  $\text{Ni@Sn}_9^{4-}$  endohedral nine-atom clusters are also structural analogues of  $\text{Sn}_9^{2-}$ , with the ligand-free clusters housing the copper and nickel transition metals in the center of their respective cages.<sup>71,72</sup>

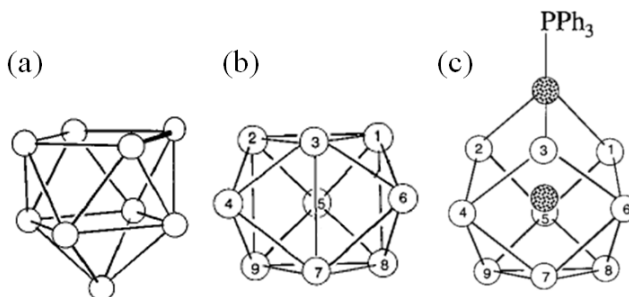


**Figure 1.8.** Structures of (a)  $\text{Sn}_9^{4-}$ , (b)  $\text{clos-Sn}_9^{2-}$ , and (c)  $\text{Pt@Sn}_9\text{Pt(PPh}_3\text{)}^{2-}$  cluster ions. The bimetallic  $\text{Pt@Sn}_9\text{Pt(PPh}_3\text{)}^{2-}$  ion may be viewed as a metalated derivative of  $\text{Sn}_9^{2-}$  (taken from ref [58]).

### 1.3.2. Endohedral $M@E_{10}$ and $M@E_{12}$ Transition Metal Derivatives

Naked, or ligand-free, Zintl clusters are potentially excellent candidates for cluster assembly processes.<sup>52</sup> Naked Zintl clusters have been of interest for their potential ability to assemble into nanomaterials, because ligands can hinder packing efficiency.<sup>52</sup> The more broad field of cluster science has been targeting the fabrication of nanomaterials from discrete clusters such as the fullerenes, cadmium selenide clusters or magic clusters, as their size and properties are much more precise and/or tunable than those of nanomaterials.<sup>76</sup>

Several theoretical studies were done from 2002-2004 to determine possible ligand-free Zintl clusters that had not yet been discovered that could lend interesting new properties to this growing area of cluster science.<sup>77-84</sup> Computational studies steadily pointed towards  $E_{12}^{4-}$  and  $E_{10}^{2-}$  ( $E = \text{Si, Ge, Sn, Pb}$ ) as well as their endohedral transition metal derivatives  $M@E_{12}^{2-}$  and  $M@E_{10}^{2-}$  ( $M = \text{Ni, Pt}$ ). Kumar noted that the smaller silicon and germanide clusters were



ideal to encapsulate nickel atoms, whereas the stannides and plumbides were more ideal to house the larger platinum atom for increased stability.<sup>80</sup> The theoretical studies encouraged efforts to synthesize these undiscovered group 14 clusters. From a structural standpoint, they indeed mimic the fullerenes in that they approach being spherical. The spherical shape is a favorable characteristic increasing the potential for hexagonal closest packing of such clusters. The three-fold symmetry of the [K(2,2,2-crypt)]<sup>+</sup> cation promotes the formation of hexagonal arrays, while the spherical-like nature of the clusters allow them to pack efficiently.

Shortly thereafter endohedral ten and twelve-atom clusters were successfully synthesized from the E<sub>9</sub><sup>4+</sup> parent complexes. The first complex of this type was the Pt@Pb<sub>12</sub><sup>2-</sup> cluster anion, isolated by Eichhorn *et al.* (Figure 1.9a).<sup>52,85</sup> The cluster was prepared by reacting Pb<sub>9</sub><sup>4+</sup> with [PPh<sub>3</sub>]<sub>4</sub> in the presence of 2,2,2-crypt in an ethylenediamine/toluene solution and is defined by a Pb<sub>12</sub><sup>2-</sup> ion centered by a platinum atom. The 12 lead atoms are arranged as a near regular icosahedron, giving it virtual icosahedral (I<sub>h</sub>) point symmetry as expected from the previously mentioned theoretical studies. The icosahedral shapes are sphere-like, allowing for the efficient packing of the naked cluster anions in a crystal lattice as illustrated in Figure 1.9.

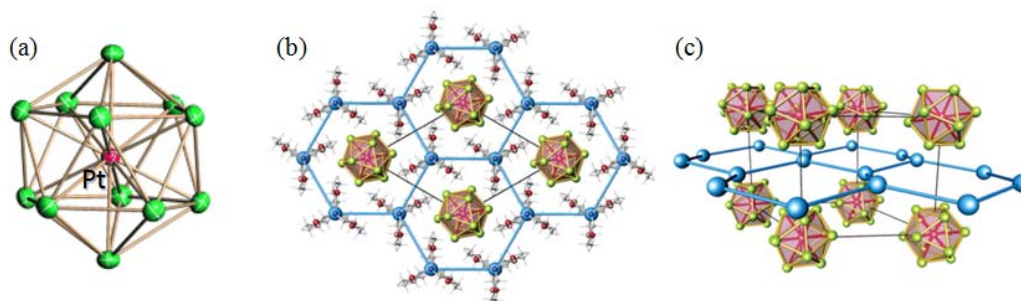


**Figure 1.9.** Drawing of (a) the icosahedral *closo*-[Pt@Pb<sub>12</sub>]<sup>2-</sup> polyanion and the packing of the clusters (b) with respect to the 001 projection and (c) a side view showing the placement of the clusters with respect to the plane of potassium ions. [K(2,2,2-crypt)]<sup>+</sup> counterions (Pb = green, Pt = pink, K = blue, crypt = red and gray). The cryptands are omitted in structure c for clarity (taken from references [52,85]).

Additional high symmetry clusters of intermediate size were later characterized including Ni@Pb<sub>10</sub><sup>2-</sup>,<sup>52,86</sup> Al@Pb<sub>n</sub><sup>+</sup> (n = 10, 12),<sup>87</sup> M@Pb<sub>12</sub><sup>2-</sup> (M = Ni, Pd),<sup>52</sup> and M@Ge<sub>10</sub><sup>2-</sup> (M = Co, Fe).<sup>88,89</sup> Lievens and coworkers first synthesized gas-phase Al@Pb<sub>10</sub><sup>+</sup> and Al@Pb<sub>12</sub><sup>+</sup> clusters in laser vaporization studies and observed the cations via mass spectrometry.<sup>87</sup> Density functional theory (DFT) studies revealed the clusters were most plausibly bicapped square antiprisms and icosahedral, respectively, as highlighted in Figure 1.10a-b.

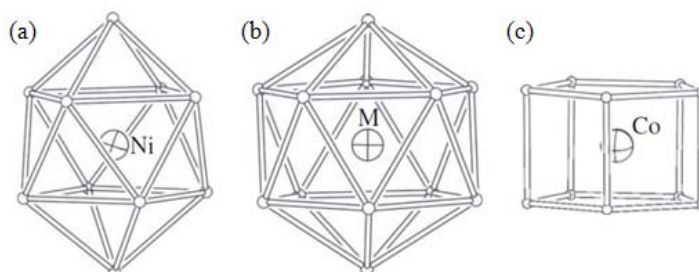


**Figure 1.10.** Bimetallic ligand-free ten and twelve-atom Zintl clusters. (a) Al@Pb<sub>10</sub><sup>+</sup>, Ni@Pb<sub>10</sub><sup>2-</sup>, (b) Al@Pb<sub>12</sub><sup>+</sup> and M@Pb<sub>12</sub><sup>2-</sup> (M = Ni, Pd, Pt), and (c) M@Ge<sub>10</sub><sup>2-</sup> (M = Co, Fe) (taken from reference [2]).

In 2005 Eichhorn and coworkers reported the synthesis of  $\text{Ni@Pb}_{10}^{2-}$ , the first  $\text{M@Pb}_{10}^{2-}$  cluster characterized by X-ray crystallography.<sup>52,86</sup> The reaction of  $\text{K}_4\text{Pb}_9$  and  $\text{Ni}(\text{cod})_2$  ( $\text{cod} = 1,5\text{-cyclooctadiene}$ ) afforded the cluster, which crystallized from an ethylenediamine/toluene solution. Consistent with the theoretical structure of  $\text{Al@Pb}_{12}^+$ ,  $\text{Ni@Pb}_{10}^{2-}$  is a *closo*-bicapped square antiprism with an endohedral nickel atom as illustrated in Figure 1.10a. This discovery was soon followed by the discovery of the nickel and palladium derivatives of  $\text{Pb}_{12}^{2-}$  to complete the series of icosahedral group 10 derivatives,  $\text{M@Pb}_{12}^{2-}$  ( $\text{M} = \text{Ni, Pd, Pt}$ ) (Figure 1.10b).<sup>52</sup> The three clusters were the sole icosahedral clusters characterized structurally prior to 2010. Solution NMR studies have shown them to possess  $\sigma$ -aromaticity, which will be discussed in Chapter 3.

In 2009 Fassler reported the synthesis of the  $\text{Co@Ge}_{10}^{3-}$  ion, which differs from all previous endohedral clusters in that it does not possess a deltahedral structure.<sup>88</sup> The cluster cage is a pentagonal prism with  $\text{D}_{5h}$  point symmetry as shown in Figure 1.10c and does not contain triangular faces characteristic of deltahedral structures. The unique framework of the Zintl ion was also supported by DFT calculations which showed the  $\text{D}_{5h}$  structure to be the global minimum and 13.3 kcal/mol more favorable than the traditionally expected square antiprismatic structure.  $\text{Fe@Ge}_{10}^{3-}$ , possessing the same geometry, was discovered in the same year by Goicoechea.<sup>89</sup> The new structure type is potentially a new class fullerene-like clusters based on fused pentagonal rings as predicted to exist in the  $\text{Hf@Ge}_n$  series first described by Korber.<sup>90,91</sup> In contrast,

Sevov reported the synthesis of  $\text{Ge}_{10}\text{Mn}(\text{CO})_4^{3-}$ , an *exo*-substituted  $\text{Ge}_{10}^{2-}$  derivative, in which the cluster cage is a bicapped square antiprism.<sup>92</sup>

### 1.3.3. Large Fused Intermetalloid Zintl Clusters

There are a limited number of Zintl cluster anions possessing cages beyond 12 atoms. These bimetallic clusters along with the  $\text{E}_{10/12}$  clusters are the so-called intermetalloids, ligand-free clusters composed solely of two or more metals or semimetals. In many cases intermetalloids are reminiscent of the smaller bimetallic  $\text{E}_9$  analogues mentioned above.

The first Zintl metalloid, as well as the first isolated ligand-free cluster larger than 10 atoms, was the anion  $[\text{As}@\text{Ni}_{12}@\text{As}_{20}]^{3-}$  reported by Eichhorn in 2003.<sup>93</sup> The arsenide cage cluster, illustrated in Figure 1.11, is an additional example of a cluster with interstitial units. The cluster possesses an arsenic atom in the center of an icosahedral Ni cage and that entire  $[\text{As}@\text{Ni}_{12}]^{3-}$  unit is encapsulated within the pentagonal dodecahedral  $\text{As}_{20}$  cage, the reciprocal platonic solid of the centered icosahedron.

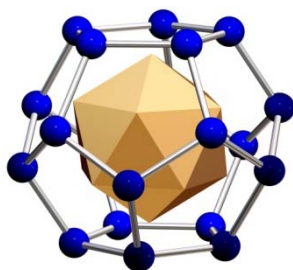


**Figure 1.11.** Icosahedral onion-like structure of the  $[\text{As}@\text{Ni}_{12}@\text{As}_{20}]^{3-}$  polyanion (taken from reference [93]).

Other metalloids are known as fused clusters, due to their appearance of being formed through the joining of two smaller clusters. Interestingly, all of these large clusters have smaller bimetallic analogues that are likely intermediates along their synthetic pathways. The first clear example of a Zintl that could be idealized as a fusion of two clusters is the  $\text{Ni}_3@\text{Ge}_{18}^{4-}$  germanide, isolated and characterized via X-ray crystallography and mass spectrometry by Goicoechea and Sevov (Figure 1.12c).<sup>94</sup> The cluster was synthesized via the reaction of  $\text{Ge}_9^{4-}$  and 3 equivalents of  $\text{Ni}(\text{cod})_2$  in the presence of 2,2,2-crypt in ethylenediamine. The authors speculate that the cluster is formed by the fusion of  $\text{Ni}@\text{Ge}_9^{3-}$  and  $\text{Ni}@\text{Ge}_9\text{NiL}^{2-}$  clusters where L is a ligand (Eq 1.4). The final fused cluster was not isolated as a result of a series of individual reactions as implied by the equation, but the isolation and existence of each component serves as a clue to the reaction's mechanism. The  $\text{Ni}@\text{Ge}_9^{3-}$  cluster was reported in the same study and obtained via the reaction of  $\text{K}_4\text{Ge}_9$  with 1 equivalent of  $\text{Ni}(\text{cod})_2$  (Figure 1.12a). The subsequent nickel substituted cluster  $\text{Ni}@\text{Ge}_9\text{NiL}^{2-}$ , where L would likely be cod was not isolated, but its likely existence was supported by the existence of the  $\text{Ni}@\text{Ge}_9\text{Ni}(\text{PPh}_3)^{2-}$  ion, previously isolated by Eichhorn and coworkers.<sup>95,96</sup> Shown in Figure 1.12b,  $\text{Ni}@\text{Ge}_9\text{Ni}(\text{PPh}_3)^{2-}$  has a tricapped trigonal prismatic structure comparable to that of the two  $\text{Ni}@\text{Ge}_9$ -units of  $\text{Ni}_3@\text{Ge}_{18}^{4-}$ .



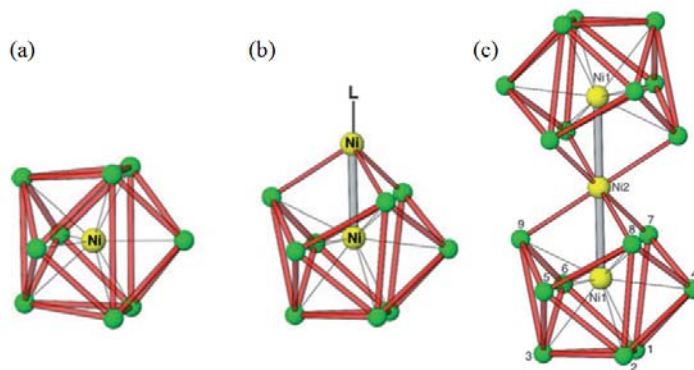


**Figure 1.12.** Crystal structures of (a)  $\text{Ni@Ge}_9^{3-}$ , (b)  $\text{Ni@Ge}_9\text{Ni}(\text{PPh}_3)^{2-}$ , and (c)  $\text{Ni}_3\text{@Ge}_{18}^{4-}$ . The  $\text{Ni@Ge}_9^{3-}$  and  $\text{Ni@Ge}_9\text{Ni}(\text{PPh}_3)^{2-}$  ions are proposed monomers of the  $\text{Ni}_3\text{@Ge}_{18}^{4-}$  fused cluster (taken from reference [94]).

Additional fused clusters such as  $\text{Pd}_2\text{@Ge}_{18}^{4-}$ ,  $\text{Ni}_2\text{@Sn}_{17}^{4-}$ ,  $\text{Pd}_2\text{@Sn}_{18}^{4-}$ ,  $\text{Pt}_2\text{@Sn}_{17}^{4-}$ , and  $(\text{Ni@Sn}_8)(\mu\text{-Ge})(\text{Ni@Sn}_8)^{4-}$  were isolated subsequently.<sup>72,74,97-100</sup>  $\text{Pd}_2\text{@Ge}_{18}^{4-}$  is similar in structure to the trinickel anion, but having only two palladium centers causes a shortening of the distance between the  $\text{Ge}_9$ -units giving a more compact, capsule-like structure.<sup>97</sup> The same structure type is observed in the characterization of  $\text{Pd}_2\text{@Sn}_{18}^{4-}$ , the largest Zintl stannide isolated to date (Figure 1.13b).<sup>99,100</sup> The clusters were synthesized in the reaction of either  $\text{Ge}_9^{4-}$  or  $\text{Sn}_9^{4-}$  with excess  $\text{Pd}(\text{PPh}_3)_4$  in the presence of 2,2,2-crypt. The clusters possess pseudo- $D_{3d}$  point symmetry with two palladium atoms acting as foci in the elongated cage.

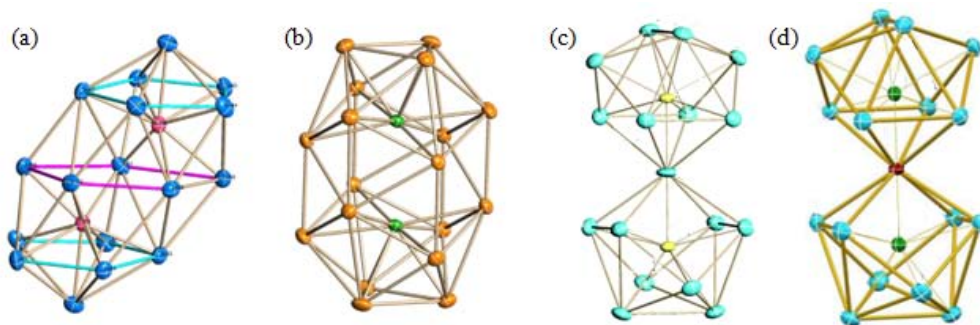


**Figure 1.13.** The crystal structure of  $\text{Pt}_2@Sn_{17}^{4-}$ ,  $\text{Pd}_2@Sn_{18}^{4-}$ ,  $\text{Ni}_2@Sn_{17}^{4-}$ , and  $(\text{Ni}@Sn_8)(\mu\text{-Ge})(\text{Ni}@Sn_8)^{4-}$  (taken from references [72,74,97-100]).

Two very different  $M_2@Sn_{17}^{4-}$  clusters were reported by Eichhorn and coworkers with the synthesis of  $\text{Pt}_2@Sn_{17}^{4-}$  and  $\text{Ni}_2@Sn_{17}^{4-}$ . The  $\text{Pt}_2@Sn_{17}^{4-}$  anion is capsule-like as shown in Figure 1.13a, but the tin is arranged quite different from in the  $\text{Pd}_2@Sn_{18}^{4-}$  cluster.<sup>74</sup> The  $\text{Pt}_2@Sn_{17}^{4-}$  cluster is built on a framework of two  $\text{Pt}@Sn_9$  subunits sharing a common vertex. The cluster is a member of the  $C_2$  point group, composed of two  $\text{PtSn}_6$  pentagonal prisms. Although  $\text{Ni}_2@Sn_{17}^{4-}$  is isoelectronic to the platinum capsule, the structure with virtual  $D_{2d}$  point symmetry is more similar to the  $\text{Ni}_3@Ge_{18}^{4-}$  cluster (Figure 1.13c).<sup>98</sup> The cluster is composed of two  $\text{Ni}@Sn_8$  cages fused and held together by an additional tin atom instead of a transition metal as in the case of  $\text{Ni}_3@Ge_{18}^{4-}$ . Recently in 2011, Sevov and coworkers reported the synthesis of the first heteroatomic fused cluster,  $\text{Ni}@Sn_8(\mu\text{-Ge})\text{Ni}@Sn_8^{4-}$ .<sup>72</sup> The cluster is both isostructural and isoelectronic to  $\text{Ni}_2@Sn_{17}^{4-}$  (Figure 1.13d), differing only by the germanium atom at the vertex site bridging eight tin atoms in the center of the cluster. The cluster was synthesized by utilizing the heteroatomic  $\text{Ge}_{4.5}\text{Sn}_{4.5}^{4-}$  cluster as the Zintl precursor.

### 1.3.4. Oxidative Coupling and Polymerization of Zintl Clusters

In attempt to isolate larger Zintl clusters, the polymerization of Zintl clusters has been seen to a small degree. The linking of group 14 Zintl clusters was first seen in 1999 with the oxidative coupling of germanide clusters to give the  $[\text{Ge}_9\text{-Ge}_9]^{6-}$  dimer.<sup>12,101</sup> The product is made of up of two *nido*- $\text{Ge}_9$ -subunits covalently linked via an *exo*-bond between atoms along the open square face, such that the bond is an inversion center for the cluster as shown in Figure 1.14. The mechanism by which the dimer forms is unclear, but Sevov speculates that the one-electron oxidation of  $\text{Ge}_9^{4-}$  leads to the formation of the  $\text{Ge}_9^{3-}$  radical anion which is thereby able to couple to a like radical to give the  $[\text{Ge}_9\text{-Ge}_9]^{6-}$  oligomer.<sup>101</sup>

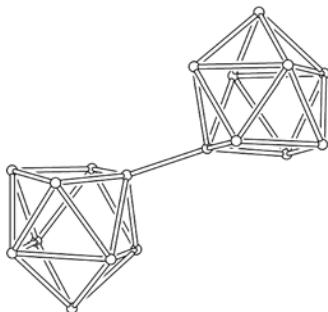


**Figure 1.14.** Structure of the  $[\text{Ge}_9\text{-Ge}_9]^{6-}$  dimer, a product of the oxidative coupling of  $\text{Ge}_9^{4-}$  (taken from reference [12]).

Sevov and coworkers have since reported the synthesis of  $[\text{Ge}_9=\text{Ge}_9=\text{Ge}_9]^{6-}$  and  $[\text{Ge}_9=\text{Ge}_9=\text{Ge}_9=\text{Ge}_9]^{8-}$ , which were the first Zintl cluster trimers and tetramers, respectively.<sup>12,102,103</sup> The trimer was synthesized via the reaction with  $\text{PPh}_3$  or  $\text{AsPh}_3$  as mild oxidizing agents,<sup>102</sup> while the tetramer was synthesized by a thermal oxidation process.<sup>103</sup> The monomers of each oligomer have an average oxidation of  $\text{Ge}_9^{2-}$  but the charge is delocalized over the entire



cluster chain. The individual  $\text{Ge}_9$ -units are bonded to each adjacent  $\text{Ge}_9$  group through two *exo*-bonds. The tetramer is described as nanorodlike, with a 2 nm long capsule structure and with an aspect ratio of 5. In subsequent studies, Guloy reported the synthesis of the linear polymer,  $_{1\infty}[\text{Ge}_9]^{2-}$  (Figure 1.15), via the reaction of  $\text{K}_4\text{Ge}_9$  with 18-crown-6 in an ethylenediamine/toluene solvent mixture.<sup>104</sup>

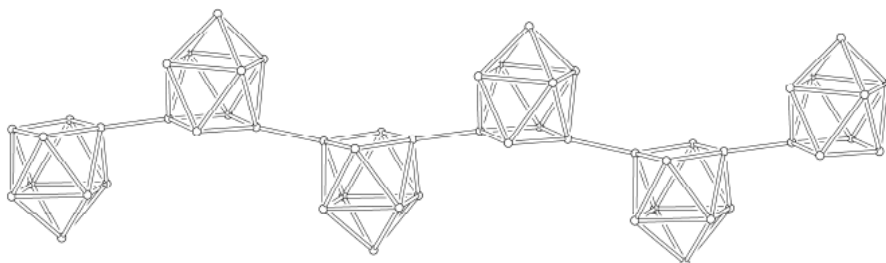


**Figure 1.15.** Structure of the  $_{1\infty}[\text{Ge}_9]^{2-}$  polymer (taken from reference [12]).

Oligomers and polymers of Zintl clusters held together with transition metals have also been isolated by Fassler.<sup>12</sup> The reaction of  $\text{Ge}_9^{4-}$  with the  $\text{AuCl}(\text{PPh}_3)$  gold precursor afforded the  $\text{Au}_3\text{Ge}_{18}^{5-}$  gold trimer and  $\text{Au}_3\text{Ge}_{45}^{9-}$  pentamer.<sup>105,106</sup> In the trimer, the gold atoms are arranged in a triangle linking two  $\text{Ge}_9$ -units. The pentamer is the largest known germanium cluster and is composed of four  $\text{Ge}_9$ -groups linked to three central gold atoms through nine bridging germanium atoms.<sup>106</sup> There was further success in utilizing mercury to isolate the  $_{1\infty}[\text{HgGe}_9]^{2-}$  polymer, in which the transition metal bridges a linear array of  $\text{Ge}_9$  clusters (Figure 1.16).<sup>107</sup>

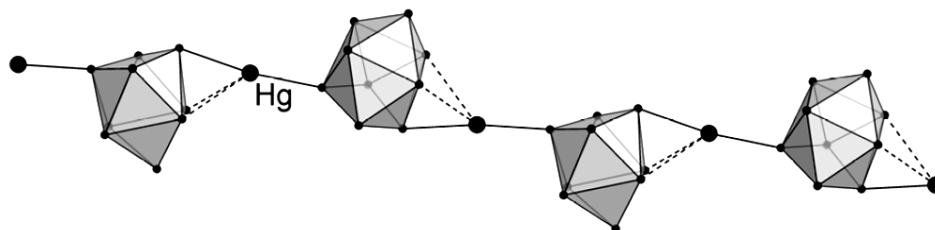


**Figure 1.16.** Structure of the  $_{1\infty}[\text{HgGe}_9]^{2-}$  polymer (taken from reference [12]).

The polymerization of these clusters is important to the goal of forming nanomaterials, as it shows the ability for short range order and highlights the potential for long range order to give nanomaterials with novel properties.

#### 1.4. Solution Dynamics of Group 14 Zintl Ions

Through the use of NMR spectroscopy, the fluxionality of Zintl clusters in solution has been studied and gives telling information about atomic mobility. These studies may provide clues about atomic mobility within small NPs. Zintl clusters are soluble in solvents polar aprotic solvents such as ammonia, ethylenediamine (en), dimethylformamide (dmf), and pyridine (pyr). Additionally, most Zintl clusters slowly decompose in dmf and pyr.

As previously mentioned, the frameworks of Zintl clusters are not supported by strong, rigid  $\sigma$ -bonds. This feature sets them apart from the fullerenes, which are held together by strong  $\sigma$  and  $\pi$ -bonding interactions. As a result, the delocalized electronic character allows for the scrambling of bonds within a cluster cage, which can often be observed through NMR analysis. The  $^{119}\text{Sn}$  NMR spectrum of the  $\text{Sn}_9^{4-}$  stannide parent complex, shown in Figure 1.17, is a classic example. On the basis of the  $C_{4v}$  solid state structure, one would anticipate three signals with a relative intensity of 4:4:1, yet only one signal is

present about at -1208 ppm, relative to a tetramethyltin external standard. This inconsistency can be explained by the rapid breaking and reformation of bonds in the cluster. The dynamic process is shown in Figure 1.17a.<sup>62</sup> Formation of a bond along the open square face with the simultaneous breaking of the bond between atoms, such as Sn5 and Sn8, gives an identical structure. This process allows the open square face to scramble around to different positions rapidly with respect to the NMR time scale, making each tin atom chemically equivalent. Likewise, the  $\text{Pb}_9^{4-}$  ion has a single signal with a chemical shift 4089 ppm upfield from 1 M  $\text{Pb}(\text{NO}_3)_2$ .

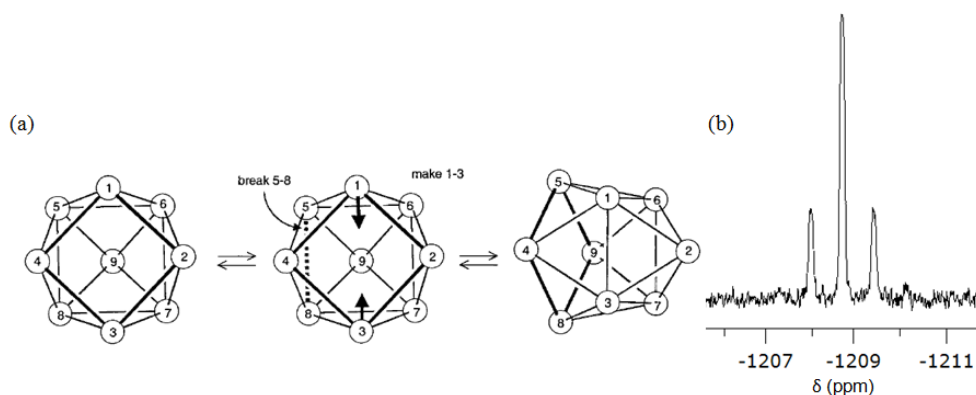


**Figure 1.17.** (a) Proposed fluxional process and (b)  $^{119}\text{Sn}$  NMR spectrum of the  $\text{Sn}_9^{4-}$  cluster anion (fluxional scheme taken from reference [62]). The first cluster is viewed down the  $C_4$  rotational axis.  $^{119}\text{Sn}$  NMR data was recorded at 298 K at 186.4 MHz in en.

The  $^{119}\text{Sn}$  NMR spectrum of  $\text{Sn}_9^{4-}$  is further complicated by the fact that there are two naturally occurring spin active nuclei ( $I = 1/2$ ), of comparable and low abundances ( $^{119}\text{Sn}$  8.68%,  $^{117}\text{Sn}$  7.67%). While the nine atoms of  $\text{Sn}_9^{4-}$  are chemically equivalent, a singlet is not observed experimentally. The chemical shift observed is actually the superposition of signals resulting from different isotopomers of the cluster, where  $J(^{119}\text{Sn}-^{117}\text{Sn}) = 263$  Hz. The observed relative

intensities agree with the statistical analysis expected for the two natural abundances.

Although the dynamic effects complicate the NMR spectra of various Zintl clusters, it provides a unique handle for the identification of the nuclearity of tin clusters in solution. As detailed above in section 1.3, various products have arisen from the reaction of the  $E_9^{4-}$  anions with the zero-valent platinum precursor,  $Pt(PPh_3)_4$ . Rudolph's complex, of proposed structure  $Sn_9Pt(PPh_3)_x^{4-}$ , has yet to be isolated in the solid state. As a result, its accepted chemical identity is based solely on the basis of  $^{119}Sn$  and  $^{195}Pt$  NMR experiments as well as the  $^{207}Pb$  spectrum for the lead analogue.<sup>57</sup> The  $^{119}Sn$  NMR spectrum has a single time-averaged chemical shift at -736 ppm that is marked by a 1:4:1 "triplet" as a result of the coupling to a single  $^{195}Pt$  nucleus ( $I = 1/2$ , 33% abund.). The presence of the lone signal suggests that the complex is highly fluxional, while spin-spin coupling is also observed in the spectrum due to coupling to spin active  $^{117}Sn$  nuclei. A nine-atom system in which the tin atoms are chemically equivalent implies an expected relative intensity pattern of 0.04:0.31:1:0.3 1:0.04, while 0.06:0.33:1:0.33:0.06 was observed experimentally leading Rudolph to identify the structure as a complex possessing nine tin atoms.<sup>57</sup> The  $^{207}Pb$  NMR of  $Pb_9Pt(PPh_3)_x^{4-}$  is less telling in terms of the lead composition but the complex is assumed to be similar in nature to the tin cluster. Attempts to locate the  $^{195}Pt$  resonance were unsuccessful and a lack of observed  $^{119}Sn$ - $^{31}P$  coupling leaves a lack of sufficient evidence to give specific values to the number of  $PPh_3$  ligands,  $x$ . Although the dynamic effects lend some compelling evidence of the structure's

make up, the exact composition and symmetry of the cluster is still unknown to this date.

Eichhorn and coworkers reported the synthesis of the  $\text{Pt@Sn}_9\text{H}^{3-}$  platinum hydride complex.<sup>74</sup> The proposed *nido*-like structure is illustrated in Figure 1.18a was determined after extensive NMR studies enhanced by the dynamic scrambling of the hydride about the cluster. One signal was observed via  $^{119}\text{Sn}$  NMR indicating high fluxionality on the NMR time scale. The  $^{119}\text{Sn}$  singlet displays  $^{195}\text{Pt}$  satellites due to coupling to one  $^{195}\text{Pt}$  nucleus to give a doublet of 33% intensity ( $J(^{195}\text{Pt}-^{119}\text{Sn}) = 1540$  Hz). Splitting by the proposed hydride ligand gives a doublet on the singlet as well as on the  $^{195}\text{Pt}$  satellites ( $J(^{119}\text{Sn}-^1\text{H}) = 46$  Hz), while tin isotopomer splitting is also present ( $J(^{119}\text{Sn}-^{117}\text{Sn}) = 160$  Hz). A proton signal marked by second order effects was subsequently located at -22.3 ppm (Figure 1.18c). Sophisticated  $^{119/117}\text{Sn}$  and  $^{195}\text{Pt}$  decoupled  $^1\text{H}$  NMR experiments made possible through the use of a custom-made Bruker Quad nuclei inverse probe further supported the proposed composition of the cluster. The selectively decoupled proton spectra also support the proposed composition with the observed relative line intensities corresponding to one platinum and nine tin atoms. Splitting patterns supporting the same findings in the  $^{195}\text{Pt}$  NMR spectrum are also observed, with relative intensities similar to the structurally characterized nine atom cluster  $[\text{Pt@Sn}_9\text{Pt}(\text{PPh}_3)]^{2-}$ .

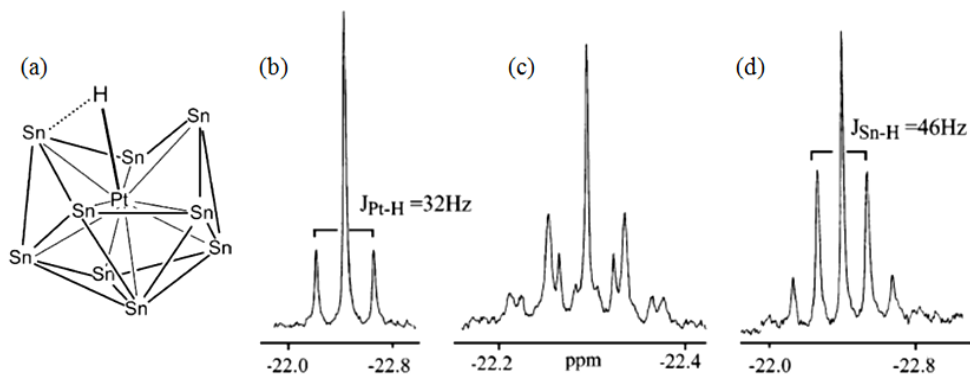


**Figure 1.18.** (a) Proposed structure of the platinum-hydride  $\text{Pt@Sn}_9\text{H}^{3-}$  ion along with its (b)  $^1\text{H}\{^{119/117}\text{Sn}\}$ , (c)  $^1\text{H}$ , and (d)  $^1\text{H}\{^{195}\text{Pt}\}$  NMR spectra (taken from reference [74]).

NMR spectroscopy alone cannot identify the structure of an unknown cluster. As the authors note, the number of atoms present in the structure cannot unequivocally be proven with NMR, in part due to the fluxionality, but they believe strongly in the evidence provided. The charge on the cluster was determined through solubility studies. As the cluster is diamagnetic, it implies a 20 ( $2n+2$ ) or 22 ( $2n+4$ ) electron count for the nine-vertex cluster, which supports a -1 or -3 charge. As soluble -1 charged Zintl clusters had not been reported previously, a -3 charge was assumed because of its solubility as well as its stability. X-ray studies of Pd and Ni analogues confirm the -3 charge assignment and structure.<sup>108</sup>

Without a crystal structure, defining the symmetry and exact composition of a Zintl cluster can be quite difficult due to fluxionality. On the other hand, an immense amount of information can be gleaned about the atomic mobility within the clusters in solution if used in conjunction with a solved X-ray structure. A enlightening example can be seen through analysis of the  $\text{Sn}_9\text{M}(\text{CO})_3^{4-}$  series, where  $\text{M} = \text{Cr}, \text{Mo}, \text{W}$ .<sup>62</sup> The solid state structures of  $\text{Sn}_9\text{Cr}(\text{CO})_3^{4-}$  and

$\text{Sn}_9\text{Mo}(\text{CO})_3^{4-}$  are defined by a *closo*-type deltahedral cage in which the ligated metals are in a capping site of the cage, bonded to four tin atoms in a  $\eta^4$  manner. The tungsten cluster differs in that the transition metal is bonded in a  $\eta^5$  fashion lying along the waist of the cluster. Based on the solid state structure one would expect the  $\eta^5\text{-Sn}_9\text{W}(\text{CO})_3^{4-}$  cluster to have six unique  $^{119}\text{Sn}$  chemical shifts due to its  $C_s$  point symmetry, but instead only three signals in a 4:4:1 ratio were detected, more consistent with a  $\eta^4$  structure. This can be accounted for in an interconversion process between the two structure types in which triangular faces on the deltahedral clusters rotate fast on the NMR time scale, exchanging the position of the  $\text{W}(\text{CO})_3$  group. This effectively creates an average signal consistent with the weighted equilibrium of the two species in solution. The likelihood of this dynamic process shown in Figure 1.19 was further supported by the observation of the three signals from dissolved crystalline material possessing  $\eta^4$  and  $\eta^5$  clusters previously analyzed via IR spectroscopy.

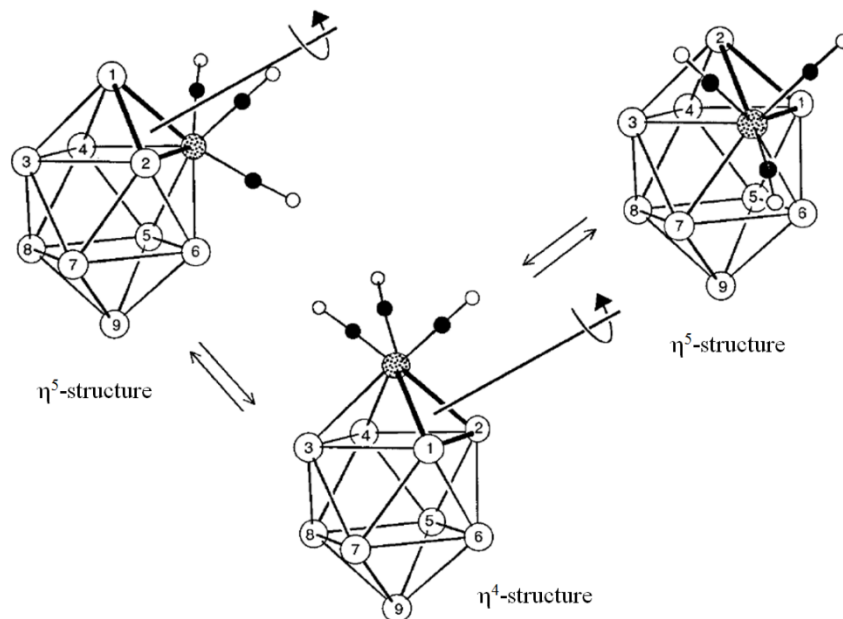


**Figure 1.19.** Proposed dynamic scheme for the interconversion between the  $\eta^4$  and  $\eta^5$  isomers of  $\text{Sn}_9\text{M}(\text{CO})_3^{4-}$ , where  $\text{M} = \text{Cr}, \text{Mo}, \text{W}$  (taken from reference[62]).

The  $\text{Sn}_9\text{Cr}(\text{CO})_3^{4-}$  and  $\text{Sn}_9\text{Mo}(\text{CO})_3^{4-}$  clusters, observed as the  $\eta^4$  isomer via crystallography, produce NMR spectra with three signals as expected though the spectrum of the molybdenum analogue looks visually much like that of tungsten with matching coupling constants and satellite patterns. Additionally, the chemical shifts and coupling constants of each cluster are very sensitive to temperature and solvent choice. This indicates that all three  $\text{Sn}_9\text{M}(\text{CO})_3^{4-}$  clusters are engaged in an isomer equilibrium process, while closer to room temperature the chromium substituted cluster equilibrium lies closer to the  $\eta^4$  structure.

The larger stannide and plumbide Zintl clusters exhibit dynamic character in solution. The  $\text{Ni}@\text{Pb}_{10}^{2-}$  cluster for example possess  $D_{4d}$  point symmetry and has two distinct  $^{207}\text{Pb}$  chemical environments, yet a lone signal is observed at a chemical shift of  $\delta = -996$  ppm.<sup>52</sup> This coupled with the broadness of the signal



with a  $\frac{1}{2}$  height of 280 Hz are indications of a dynamic exchange taking place in solution. The  $^{207}\text{Pb}$  NMR spectra of the icosahedral  $\text{M@Pb}_{12}^{2-}$  complexes are also marked by one singlet, with coupling to  $^{195}\text{Pt}$  in the case of  $\text{Pt@Pb}_{12}^{2-}$ , but no dynamic information could be obtained from the spectra as the icosahedral point symmetry renders each lead site identical, despite any possible dynamic exchange present.<sup>52</sup> The  $^{119}\text{Sn}$  NMR spectra of the  $\text{Pt}_2\text{@Sn}_{17}^{4-}$  and  $\text{Pd}_2\text{@Sn}_{18}^{4-}$  clusters have single signals at  $\delta = -742$  ppm and  $-734$  ppm respectively, with the atoms exhibiting what the authors term as liquidlike behavior.<sup>74,99</sup> The four distinct  $^{119}\text{Sn}$  chemical environments of  $\text{Ni}_2\text{@Sn}_{17}^{4-}$  can be located but require an extremely low temperature of  $-64$  °C, therefore showing dynamic effects at ambient temperatures.<sup>98</sup> As data suggests, increasing the number of atoms shows continued dynamic effects and the smaller systems lend info as to the possible types of exchange processes. This very phenomenon likely extends to small NPs, making the isolation of larger Zintlts quite desirable.

## 1.5. Intermetallic Nanoparticles

Bimetallic NPs of active Pt-group metals (PGMs) such as Rh, Ir, Pd and Pt are used in a variety of catalytic and electrocatalytic applications. While the PGMs provide the base activity of the catalyst, the secondary metals modify the PGM activity and/or impart tolerance to various poisons. For example, PtRu and PtFe bimetallic NP electrocatalysts show much higher tolerance to CO impurities in hydrogen fuel cell applications in comparison to pure Pt NPs.<sup>109,110</sup> One drawback of PtM alloy catalysts is their low chemical and electrochemical

stability relative to pure Pt. These instabilities can lead to catalyst degradation, phase separation and ion migration in electrochemical applications. In contrast, intermetallic NPs are often significantly more stable than alloys; especially in acidic media.<sup>111</sup> Alloys and intermetallics differ in their crystal structures and, usually, the degree of atomic order. Alloys typically adopt the crystal structures of one of the metallic end members and contain random distributions of atoms in homogenous solid solutions. Intermetallics adopt crystal structures distinct from the metal end members and typically contain ordered atomic lattices with higher lattice energies. Atomic ordering in intermetallic NPs can also be exploited to alter reaction pathways as has been well documented in the PtBi and PtPb intermetallic electrocatalysts used in formic acid fuel cells.<sup>111-113</sup>

Due to the unique catalytic activity and enhanced stability of intermetallic catalysts, recent efforts have been devoted to preparing small intermetallic NPs to optimize surface area and atom economy. Polyol and seeded growth methods have been employed to prepare PtM NPs where M = Bi, Pb but these methods require moderate temperature annealing steps to induce crystallographic ordering (*i.e.* intermetallic formation), which can lead to undesirable particle growth.<sup>114</sup> As a result, there are only a few known examples of small (< 8 nm) intermetallic NPs despite the promising properties of the catalysts.<sup>115-120</sup> For example, the face-centered tetragonal PtSn intermetallic electrocatalyst shows marked improvements in stability and CO tolerance in hydrogen electrooxidation applications when compared to the PtSn alloy or Pt NP catalysts of similar size.<sup>118</sup> Likewise, the 2-3 nm PtBi intermetallics recently reported by Nazar show

significantly higher mass activity for formic acid electrooxidation relative to other known catalysts.<sup>121</sup>

## 1.6. Overview of the Thesis

In the remainder of the thesis, the synthesis and characterization of bimetallic group 14 transition metal derivatives will be discussed. Additionally the details on the fabrication of intermetallic phases isolated as NPs for the first time, made from Zintl precursors will also be described.

In Chapter 2, the synthesis of three isolated  $E_9$  bimetallic clusters  $E_9Mcod^{3-}$  ( $E = Sn, Pb$ ;  $M = Rh, Ir$ ) will be discussed. The synthesis of  $Rh@Sn_{12}^{3-}$  and  $M@Pb_{12}^{3-}$  ( $M = Rh, Ir$ ) ions will be discussed in Chapter 3 as well as their solution dynamics along with that of the previously isolated  $Ir@Sn_{12}^{3-}$  as studied via NMR spectroscopy. Novel complexes synthesized due to the reducing properties of the  $E_9^{4-}$  ions will be described in Chapter 4. Lastly, Chapter 5 will focus on the fabrication of intermetallic  $PtSn_4$  and  $Ir_3Sn_7$ , and the characterization of these materials via TEM and XRD spectroscopy; and a summary of the conclusions will be discussed in Chapter 6.

## Chapter 2: Group 9 Derivatives of $\text{Sn}_9^{4-}$ : $\text{Sn}_9\text{ML}$

### 2.1. Introduction

Bimetallic clusters derived from the  $\text{E}_9^{4-}$  Zintl ions ( $\text{E} = \text{Ge}, \text{Sn}, \text{Pb}$ ) are of interest due to their unique structures and properties as well as their similarity to fullerenes.<sup>13</sup> Particularly interesting is the ability for both fullerenes and Zintl clusters to form endohedral structures<sup>13,51</sup> in which the centered elements are in highly symmetric coordination geometries (*e.g.* the  $\text{I}_h$  symmetries of La and Pt in  $\text{La@C}_{60}$  and  $\text{Pt@Pb}_{12}^{2-}$ ).<sup>52,53</sup> Numerous endohedral Zintl clusters have been synthesized from the  $\text{E}_9^{3-/4-}$  ions where  $\text{E} = \text{Ge}, \text{Sn}, \text{Pb}$ . Examples include  $\text{M@Pb}_{10}^{2-}$  and  $\text{M@Pb}_{12}^{2-}$  ( $\text{M} = \text{Ni}, \text{Pd}, \text{Pt}$ ),  $\text{Cu@E}_9^{3-}$  ( $\text{E} = \text{Sn}, \text{Pb}$ ),  $\text{Sn}_9\text{Pt}_2(\text{PPh}_3)^{2-}$ , and  $\text{Pd}_2@\text{E}_{18}^{2-}$  ( $\text{E} = \text{Ge}, \text{Sn}$ ).<sup>52,58,68,71,99,100</sup> While 9-vertex and 10-vertex clusters are known with and without endohedral atoms, structures with more than 10 vertices are expected to have interstitial atoms when prepared in solution or the solid state.<sup>13</sup> All of these complexes can be described as derivatives of Wade-Mingos type deltahedral clusters with the exception of the recent theoretical and experimental results showing the non-deltahedral structures of the  $\text{D}_{5h} - \text{M@Ge}_{10}^{3-}$  complexes ( $\text{M} = \text{Co}, \text{Fe}$ ).<sup>88-90,122</sup> Korber noted<sup>90</sup> that these structures might mark the emergence of a new class of fullerene-like clusters based on fused pentagonal rings as is predicted to exist in the  $\text{Hf@Ge}_n$  series.<sup>90,91</sup>

In the last few years, there has been a push to isolate group 9 transition metal ( $\text{Co}, \text{Rh}, \text{Ir}$ ) derivatives of the  $\text{Sn}_9^{4-}$  ion, due to the catalytic and electrocatalytic applications of bimetallic Pt-group metals ( $\text{Ru}, \text{Os}, \text{Rh}, \text{Ir}, \text{Pd}, \text{Pt}$ ).<sup>109,110</sup> Though cobalt is not traditionally regarded as a PGM, there have been

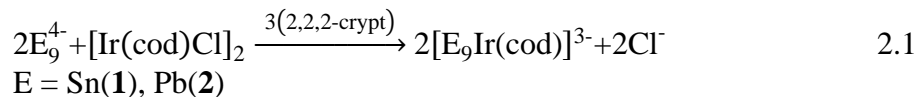
interests in incorporating it into Zintl clusters due to possible similarities in its reactivity towards the  $E_9^{4-}$  ions. The group 10 metals (Ni, Pd, & Pt) have all been incorporated into Zintl cluster anions for some time,<sup>51,52,58,74,93,94,96-100</sup> so it was therefore of interest to target Zintls containing the remaining PGMs. Therefore, to further develop the class of PGM Zintl derivatives, efforts were first placed on studying the reactions of labile Co, Ir, and Rh complexes with  $Sn_9^{4-}$  and  $Pb_9^{4-}$ .

The synthesis and characterization of  $Sn_9Ir(cod)^{3-}$ ,  $Sn_9Rh(cod)^{3-}$ , and  $Pb_9Ir(cod)^{3-}$  will be discussed in this chapter. These bimetallic  $E_9$  clusters were targeted due to their potential to act as intermediates along possible reaction pathways to access larger Zintls in a more systematic method, as well as act as precursors to intermetallic phases.

## 2.2. Results and Discussion

### 2.2.1. Synthesis

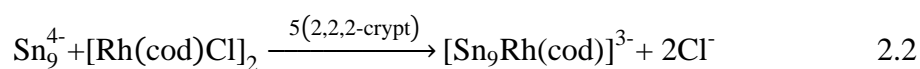
**$Sn_9Ir(cod)^{3-}$  and  $Pb_9Ir(cod)^{3-}$ :** Ethylenediamine (en) solutions of  $K_4Sn_9$  and  $K_4Pb_9$  react with toluene (tol) solutions of  $[Ir(cod)Cl]_2$  in the presence of 2,2,2-crypt to give the  $Sn_9Ir(cod)^{3-}$  (**2.1**) and  $Pb_9Ir(cod)^{3-}$  (**2.2**) ions, respectively (Eq 2.1). The  $[K(2,2,2-crypt)]^+$  salts were isolated in *ca.* 30% yield.



The  $[K(2,2,2-crypt)]^+$  salts of both clusters are air and moisture sensitive in solution and in the solid state. The salts are soluble in pyridine and DMF and have been characterized by single-crystal X-ray diffraction,  $^1H$  NMR, and  $^{13}C$

NMR. Ion **1** was also reported by Fässler and co-workers<sup>123</sup> in a concurrent study.<sup>124</sup>

**Sn<sub>9</sub>Rh(cod)<sup>3-</sup>**: Sn<sub>9</sub>Rh(cod)<sup>3-</sup> (**2.3**) is synthesized by reacting en solutions of Rb<sub>4</sub>Sn<sub>9</sub> with tol solutions of [Rh(cod)Cl]<sub>2</sub> in the presence of 5 equivalents of 2,2,2-crypt as shown in Eq 2.2. The [Rb(2,2,2-crypt)]<sup>+</sup> salt was isolated in *ca.* 55% yield and is air and moisture sensitive in solution. The salt is soluble in DMF and has been characterized by single-crystal X-ray diffraction and <sup>119</sup>Sn NMR.



### 2.2.2. Solid State Structure

The [K(2,2,2-crypt)]<sub>3</sub>[Sn<sub>9</sub>Ir(cod)] salt is triclinic, space group P $\bar{1}$ . The Sn<sub>9</sub>Ir(cod)<sup>3-</sup> cluster is depicted in Figure 2.1a. The crystallographic data for the salt is described in Table 2.1 and selected bond distances and angles for Sn<sub>9</sub>Ir(cod)<sup>3-</sup>, anion **1**, are given in and Table 2.2. The Sn<sub>9</sub>Rh(cod)<sup>3-</sup> ion detailed below is isomorphic to anion **1**.

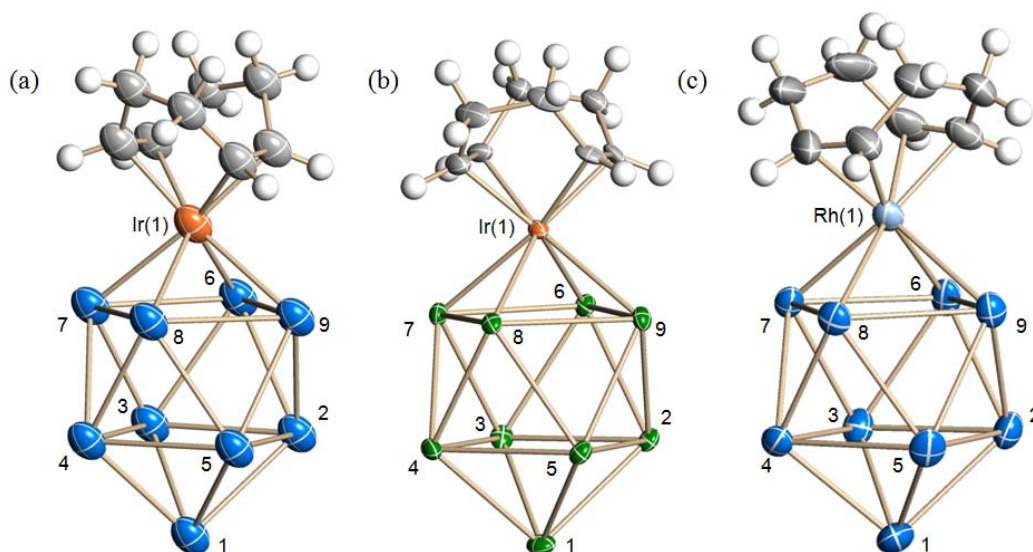


**Figure 2.1.** Structures of the  $E_9M(\text{cod})^{3-}$  cluster anions. ORTEP drawings of the (a)  $\text{Sn}_9\text{Ir}(\text{cod})^{3-}$  (**2.1**); (b)  $\text{Pb}_9\text{Ir}(\text{cod})^{3-}$  (**2.2**); (c)  $\text{Sn}_9\text{Rh}(\text{cod})^{3-}$  (**2.3**) cluster anions (blue = Sn, green = Pb, orange = Ir, light blue = Rh, gray = carbon, white = hydrogen). Thermal ellipsoids are drawn at the 50% probability level.

**Table 2.1.** Crystallographic data for the  $\text{Sn}_9M(\text{cod})^{3-}$  ions ( $M = \text{Ir}, \text{Rh}$ ).

Compound	$[\text{K}(2,2,2\text{-crypt})]_3$ $[\text{Sn}_9\text{Ir}(\text{C}_8\text{H}_{12})] \cdot 2\text{en}$	$[\text{Rb}(2,2,2\text{-crypt})]_3$ $[\text{Sn}_9\text{Rh}(\text{C}_8\text{H}_{12})] \cdot 2\text{en}$
formula weight	2735.56	3169.70
temperature (K)	150(2)	150(2)
Wavelength ( $\text{\AA}$ )	0.71073	0.71073
crystal system	triclinic	triclinic
space group	P-1	P-1
unit cell dimensions		
a ( $\text{\AA}$ )	14.8697(4)	15.065(2)
b ( $\text{\AA}$ )	14.9149(4)	15.068(2)
c ( $\text{\AA}$ )	23.6887(7)	23.103(4)
$\alpha$ ( $^\circ$ )	93.2366(5)	94.599(2)
$\beta$ ( $^\circ$ )	93.1943(5)	93.183(2)
$\gamma$ ( $^\circ$ )	112.5826(4)	111.956(2)
volume ( $\text{\AA}^3$ )	4826.0(2)	4827.4(13)
Z	2	2
$D_{\text{calc}}$ ( $\text{g}/\text{cm}^3$ )	1.883	2.181
abs. coeff. ( $\text{mm}^{-1}$ )	3.849	6.24
final R indices: $R_1,^a I > 2\sigma(I)$	0.0408	0.156
$wR_2,^a$ all data	0.0898	0.156

<sup>a</sup>  $R_1 = \Sigma ||F_o| - |F_c|| / \Sigma |F_o|$ ,  $wR_2 = [\Sigma w(F_o^2 - F_c^2)^2 / \Sigma w(F_o^2)]^{1/2}$

The structure of anion **2.1** contains an Sn<sub>9</sub> bicapped square anti-prism in which the Ir and Sn(1) atoms occupy capping sites and are bound to four Sn atoms, as illustrated in Figure 2.1a. The remaining eight Sn atoms make up the two square planes and are five coordinate in nature. According to Wade's rules<sup>59</sup>, the ion is a 10-vertex 22-electron *closo* deltahedron (each Sn = 2 e<sup>-</sup>, (cod)Ir = 1 e<sup>-</sup>, charge = 3 e<sup>-</sup>). The Ir-Sn bonds average 2.771(4) Å with a narrow range of 2.7629(4)-2.7800(4) Å. The Sn-Sn bonds are in the range 2.9258(6)-3.2072(6) Å, which is typical of Sn<sub>9</sub><sup>4-</sup> derivatives,<sup>58,62,70,73,75</sup> with the bonds of the η<sup>4</sup>-Sn(1) having the shortest average bond length of 2.950(9) Å. The square antiprism is regular in nature as shown by the narrow distribution of the Sn-Sn-Sn bond angles in the square planes (90.0° ± 1.7°). The length of the diagonals Sn(6)-Sn(8) and Sn(7)-Sn(9) are 4.3981 Å and 4.3982 Å, respectively, giving them a ratio of 1.0. These data are indicative of a regular square antiprism containing pseudo C<sub>4v</sub> symmetry. The general structure and metric parameters are similar to those of the Sn<sub>9</sub>M(CO)<sub>3</sub><sup>4-</sup> clusters where M = Cr, Mo, W.<sup>61,62</sup>



**Table 2.2.** Selected bond lengths (Å) and angles (°) for the  $\text{Sn}_9\text{Ir}(\text{cod})^{3-}$  ion.

Ir(1)-Sn(6)	2.7800(4)	Sn(5)-Sn(8)	2.9887(5)
Ir(1)-Sn(7)	2.7654(5)	Sn(5)-Sn(9)	2.9805(6)
Ir(1)-Sn(8)	2.7735(4)	Sn(6)-Sn(7)	3.1102(5)
Ir(1)-Sn(9)	2.7629(4)	Sn(6)-Sn(9)	3.1067(5)
Sn(1)-Sn(2)	2.9575(7)	Sn(7)-Sn(8)	3.1162(5)
Sn(1)-Sn(3)	2.9609(6)	Sn(8)-Sn(9)	3.1067(5)
Sn(1)-Sn(4)	2.9258(6)	Ir(1)-C(1)	2.139(6)
Sn(1)-Sn(5)	2.9549(6)	Ir(1)-C(2)	2.156(7)
Sn(2)-Sn(3)	3.0971(6)	Ir(1)-C(5)	2.146(6)
Sn(2)-Sn(5)	3.2072(6)	Ir(1)-C(6)	2.156(6)
Sn(2)-Sn(6)	2.9950(6)	C(1)-C(2)	1.419(10)
Sn(2)-Sn(9)	3.0003(5)	C(1)-C(8)	1.521(10)
Sn(3)-Sn(4)	3.1765(5)	C(2)-C(3)	1.534(9)
Sn(3)-Sn(6)	3.0073(6)	C(3)-C(4)	1.523(9)
Sn(3)-Sn(7)	2.9648(5)	C(4)-C(5)	1.501(9)
Sn(4)-Sn(5)	3.1239(6)	C(5)-C(6)	1.426(9)
Sn(4)-Sn(7)	2.9868(6)	C(6)-C(7)	1.522(10)
Sn(4)-Sn(8)	2.9873(5)	C(7)-C(8)	1.513(11)
C(1)-Ir(1)-C(2)	38.6(3)	C(1)-Ir(1)-Sn(8)	92.68(18)
C(1)-Ir(1)-C(5)	96.4(2)	C(2)-Ir(1)-Sn(8)	126.68(17)
C(5)-Ir(1)-C(2)	79.9(2)	C(5)-Ir(1)-Sn(8)	139.90(18)
C(1)-Ir(1)-C(6)	79.9(3)	C(6)-Ir(1)-Sn(8)	105.91(18)
C(5)-Ir(1)-C(6)	38.7(2)	Sn(9)-Ir(1)-Sn(6)	67.105(12)
C(2)-Ir(1)-C(6)	88.4(3)	Sn(3)-Sn(2)-Sn(5)	90.101(15)
C(1)-Ir(1)-Sn(6)	137.1(2)	Sn(2)-Sn(3)-Sn(4)	90.375(14)
C(5)-Ir(1)-Sn(6)	93.61(17)	Sn(5)-Sn(4)-Sn(3)	90.185(15)
C(2)-Ir(1)-Sn(6)	103.64(19)	Sn(4)-Sn(5)-Sn(2)	89.331(14)
C(6)-Ir(1)-Sn(6)	128.49(18)	Sn(9)-Sn(6)-Sn(7)	89.235(14)
C(1)-Ir(1)-Sn(9)	85.49(18)	Sn(6)-Sn(7)-Sn(8)	90.661(14)
C(5)-Ir(1)-Sn(9)	151.25(18)	Sn(9)-Sn(8)-Sn(7)	88.349(13)
C(2)-Ir(1)-Sn(9)	84.12(18)	Sn(6)-Sn(9)-Sn(8)	91.720(14)
C(6)-Ir(1)-Sn(9)	164.11(18)	Sn(2)-Sn(1)-Sn(3)	63.108(15)

The  $\text{Sn}_9\text{Rh}(\text{cod})^{3-}$  anion **2.3** is isostructural and isoelectronic to  $\text{Sn}_9\text{Ir}(\text{cod})\text{s}^{3-}$  (Figure 2.1c). The crystallographic data and selected bond distances and angles for anion **3** are given in Table 2.1 and Table 2.3, respectively. The Rh-Sn and Ir-Sn bonds of **2.3** and **2.1**, respectively, are virtually equivalent within experimental error, consistent with the similarity in the atomic radii of Rh and Ir. The Sn-Sn bonds are in the range 2.925(1)-3.247(1) Å. Like  $\text{Sn}_9\text{Ir}(\text{cod})^{3-}$  the Sn-Sn bonds at the capping Sn site possesses the shortest average bond length of 2.938(9) Å. The upper and lower squares of the antiprism have average bond lengths of 3.069(9) Å and 3.161(9) Å respectively, making the cluster wider about the lower waist, as summarized in Table 2.4. This differs from the iridium analogue, which has a slightly wider upper waist, as the upper and lower squares average 3.151(9) Å and 3.110(9) Å, respectively. The square antiprismatic structure of anion **3** is also regular with the Sn-Sn-Sn bond angles in the square planes measuring  $90.0^\circ \pm 1.5^\circ$ .

**Table 2.3.** Selected bond lengths (Å) and angles (°) for the Sn<sub>9</sub>Rh(cod)<sup>3-</sup> ion.

Rh(1)-Sn(6)	2.765(1)	Sn(5)-Sn(8)	3.002(1)
Rh(1)-Sn(7)	2.780(1)	Sn(5)-Sn(9)	2.963(1)
Rh(1)-Sn(8)	2.745(1)	Sn(6)-Sn(7)	3.048(1)
Rh(1)-Sn(9)	2.777(1)	Sn(6)-Sn(9)	3.091(1)
Sn(1)-Sn(2)	2.944(1)	Sn(7)-Sn(8)	3.093(1)
Sn(1)-Sn(3)	2.925(1)	Sn(8)-Sn(9)	3.042(1)
Sn(1)-Sn(4)	2.956(1)	Rh(1)-C(1)	2.15(1)
Sn(1)-Sn(5)	2.927(1)	Rh(1)-C(2)	2.17(1)
Sn(2)-Sn(3)	3.232(1)	Rh(1)-C(5)	2.16(1)
Sn(2)-Sn(5)	3.087(1)	Rh(1)-C(6)	2.17(1)
Sn(2)-Sn(6)	2.968(1)	C(1)-C(2)	1.39(2)
Sn(2)-Sn(9)	2.958(1)	C(1)-C(8)	1.47(2)
Sn(3)-Sn(4)	3.075(1)	C(2)-C(3)	1.51(2)
Sn(3)-Sn(6)	2.989(1)	C(3)-C(4)	1.50(2)
Sn(3)-Sn(7)	2.961(1)	C(4)-C(5)	1.56(2)
Sn(4)-Sn(5)	3.247(1)	C(5)-C(6)	1.37(2)
Sn(4)-Sn(7)	2.973(1)	C(6)-C(7)	1.54(2)
Sn(4)-Sn(8)	2.980(1)	C(7)-C(8)	1.52(2)
C(1)-Rh(1)-C(2)	37.5(5)	C(1)-Rh(1)-Sn(8)	150.4(4)
C(1)-Rh(1)-C(5)	96.6(5)	C(2)-Rh(1)-Sn(8)	166.9(4)
C(2)-Rh(1)-C(5)	81.6(6)	C(5)-Rh(1)-Sn(8)	86.3(4)
C(1)-Rh(1)-C(6)	80.5(5)	C(6)-Rh(1)-Sn(8)	84.5(4)
C(5)-Rh(1)-C(6)	337.0(5)	Sn(6)-Rh(1)-Sn(9)	67.80(3)
C(2)-Rh(1)-C(6)	88.7(6)	Sn(3)-Sn(2)-Sn(5)	89.93(3)
C(1)-Rh(1)-Sn(6)	89.4(4)	Sn(2)-Sn(3)-Sn(4)	90.33(3)
C(5)-Rh(1)-Sn(6)	151.4(5)	Sn(5)-Sn(4)-Sn(3)	89.88(3)
C(2)-Rh(1)-Sn(6)	86.5(4)	Sn(4)-Sn(5)-Sn(2)	89.83(3)
C(6)-Rh(1)-Sn(6)	168.6(3)	Sn(9)-Sn(6)-Sn(7)	91.41(3)
C(1)-Rh(1)-Sn(9)	83.4(3)	Sn(6)-Sn(7)-Sn(8)	88.48(2)
C(5)-Rh(1)-Sn(9)	139.1(5)	Sn(9)-Sn(8)-Sn(7)	91.47(3)
C(2)-Rh(1)-Sn(9)	126.0(4)	Sn(6)-Sn(9)-Sn(8)	55.96(3)
C(6)-Rh(1)-Sn(9)	107.2(4)	Sn(2)-Sn(1)-Sn(3)	66.84(3)

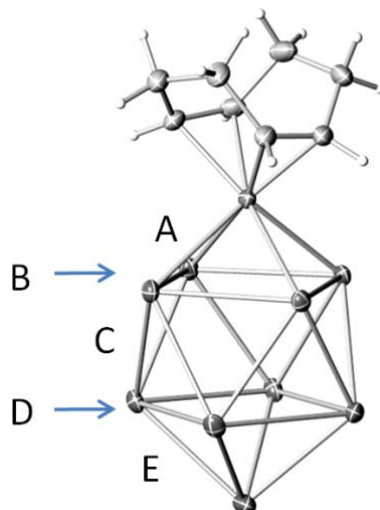


**Figure 2.2.** Structure of the  $E_9M(\text{cod})^{3-}$  cluster anions with various bonding groups defined. Group **A** describes the M-Sn bonds, while groups **B** and **D** are Sn-Sn bonds within the upper and lower square plane respectively. Group **C** is defined as the Sn-Sn bonds that make up the waist of the cluster in between the two planes. Group **E** of the cluster are the  $\eta^4$  Sn-Sn bonds involving the capping Sn atom as illustrated.

**Table 2.4.** Average Bond Distances ( $\text{\AA}$ ) of the  $\text{Sn}_9\text{M}(\text{cod})^{3-}$  clusters

Bonding groups	$\text{Sn}_9\text{Ir}(\text{cod})^{3-}$	$\text{Sn}_9\text{Rh}(\text{cod})^{3-}$	$\text{K}_4\text{Sn}_9$
<b>A</b> (M-Sn) $M = \text{Rh, Ir}$	2.770	2.767	---
<b>B</b> (Sn-Sn) upper square	3.151	3.069	3.236
<b>C</b> (Sn-Sn) waist	2.989	2.974	2.973
<b>D</b> (Sn-Sn) lower square	3.110	3.161	2.974
<b>E</b> (Sn-Sn) capping	2.950	2.938	2.960

The  $[\text{K}(2,2,2\text{-crypt})]_3[\text{Pb}_9\text{Ir}(\text{cod})]$  salt is triclinic, space group  $P\bar{1}$ , and is isomorphic to the  $\text{Sn}_9\text{Ir}(\text{cod})^{3-}$  salt. The  $\text{Pb}_9\text{Ir}(\text{cod})^{3-}$  cluster anion is illustrated above in Figure 2.1b. The crystallographic data is noted in Table 2.5, and selected bond distances and angles for  $[\text{Pb}_9\text{Ir}(\text{cod})]^{3-}$  are given in and Table 2.6.

**Table 2.5.** Crystallographic data for the  $\text{Pb}_9\text{Ir}(\text{cod})^{3-}$  ion.

Compound	$[\text{K}(2,2,2\text{-crypt})]_3[\text{Pb}_9\text{Ir}(\text{C}_8\text{H}_{12})] \cdot 2\text{en}$
formula weight	3532.06
temperature (K)	100(2)
Wavelength ( $\text{\AA}$ )	0.71073
crystal system	triclinic
space group	P-1
unit cell dimensions	
a ( $\text{\AA}$ )	14.9478(10)
b ( $\text{\AA}$ )	14.9654(10)
c ( $\text{\AA}$ )	23.5893(15)
$\alpha$ ( $^\circ$ )	93.3980(10)
$\beta$ ( $^\circ$ )	93.4440(10)
$\gamma$ ( $^\circ$ )	112.5730(10)
volume ( $\text{\AA}^3$ )	4844.4(6)
Z	2
$D_{\text{calc}}$ ( $\text{g/cm}^3$ )	2.421
abs. coeff. ( $\text{mm}^{-1}$ )	17.132
final R indices: $R_1,^a I > 2\sigma(I)$	0.0354
$wR_2,^a$ all data	0.0885

$$^a R_1 = \frac{\sum ||F_o| - |F_c||}{\sum |F_o|}, \quad wR_2 = \frac{[\sum w(F_o^2 - F_c^2)^2 / \sum w(F_o^2)^2]}{1/2}$$

The  $[\text{K}(2,2,2\text{-crypt})]_3[\text{Pb}_9\text{Ir}(\text{cod})] \cdot 2\text{en}$  crystals are isomorphous with the Sn analogue above. At the time of publication of our original paper,<sup>124</sup> the crystallographic data were weak and did not provide a high quality structure. Regardless, the connectivity between the Ir-Pb and Ir-Sn analogues is clear and the observed metric parameters are consistent with expectations. Higher quality crystals have since been isolated and characterized with an improved R-factor of 3.5%, down from 11.8%. The Ir-Pb bonds have a range of 2.836(5)-2.870(5)  $\text{\AA}$ . The Pb-Pb bonds are in the range 3.049(1)-3.355(1)  $\text{\AA}$  with the bonds of the  $\eta^4$ -Pb(1) having the shortest average bond length of 3.068(9)  $\text{\AA}$ . The square antiprism is regular in nature as shown by the narrow distribution of the Pb-Pb-Pb

bond angles in the square planes ( $90.0^\circ \pm 2.2^\circ$ ), with the square closer to the four coordinate Pb atom highly regular ( $90.0^\circ \pm 0.8^\circ$ ). The metric parameters are similar to those of  $[\text{Pb}_9\text{Mo}(\text{CO})_3]^{4-}$  and  $[\text{Pb}_9\text{Zn}(\text{C}_6\text{H}_5)]^{3-}$ .<sup>62-64,68</sup>

**Table 2.6.** Selected bond lengths (Å) and angles (°) for the  $\text{Pb}_9\text{Ir}(\text{cod})^{3-}$  ion.

Ir(1)-Pb(6)	2.8701(5)	Pb(5)-Pb(8)	3.1354(5)
Ir(1)-Pb(7)	2.8383(5)	Pb(5)-Pb(9)	3.1319(5)
Ir(1)-Pb(8)	2.8618(5)	Pb(6)-Pb(9)	3.2163(5)
Ir(1)-Pb(9)	2.8358(5)	Pb(6)-Pb(7)	3.1709(5)
Pb(1)-Pb(2)	3.0816(6)	Pb(8)-Pb(9)	3.2351(5)
Pb(1)-Pb(3)	3.0738(6)	Pb(7)-Pb(8)	3.2172(5)
Pb(1)-Pb(4)	3.0675(5)	Ir(1)-C(1)	2.139(9)
Pb(1)-Pb(5)	3.0493(5)	Ir(1)-C(2)	2.143(9)
Pb(2)-Pb(3)	3.2471(5)	Ir(1)-C(5)	2.136(10)
Pb(2)-Pb(5)	3.3024(5)	Ir(1)-C(6)	2.119(10)
Pb(2)-Pb(6)	3.1567(5)	C(1)-C(2)	1.413(14)
Pb(2)-Pb(9)	3.1012(5)	C(1)-C(8)	1.535(16)
Pb(3)-Pb(4)	3.3551(5)	C(2)-C(3)	1.539(14)
Pb(3)-Pb(6)	3.1407(5)	C(3)-C(4)	1.526(15)
Pb(3)-Pb(7)	3.1361(5)	C(4)-C(5)	1.534(13)
Pb(4)-Pb(5)	3.2756(5)	C(5)-C(6)	1.439(14)
Pb(4)-Pb(7)	3.1264(5)	C(6)-C(7)	1.535(15)
Pb(4)-Pb(8)	3.1410(5)	C(7)-C(8)	1.520(17)
C(1)-Ir(1)-C(2)	38.5(4)	C(1)-Ir(1)-Pb(8)	105.6(3)
C(1)-Ir(1)-C(5)	89.2(4)	C(2)-Ir(1)-Pb(8)	139.4(3)
C(5)-Ir(1)-C(2)	81.0(4)	C(5)-Ir(1)-Pb(8)	125.8(3)
C(1)-Ir(1)-C(6)	80.2(4)	C(6)-Ir(1)-Pb(8)	91.1(3)
C(5)-Ir(1)-C(6)	39.5(4)	Pb(7)-Ir(1)-Pb(6)	67.485(12)
C(2)-Ir(1)-C(6)	97.4(4)	Pb(3)-Pb(2)-Pb(5)	90.566(12)
C(1)-Ir(1)-Pb(6)	128.0(3)	Pb(2)-Pb(3)-Pb(4)	89.920(12)
C(5)-Ir(1)-Pb(6)	103.0(3)	Pb(3)-Pb(4)-Pb(5)	89.153(12)
C(2)-Ir(1)-Pb(6)	93.1(3)	Pb(2)-Pb(5)-Pb(4)	90.357(12)
C(6)-Ir(1)-Pb(6)	137.6(3)	Pb(7)-Pb(6)-Pb(9)	88.914(13)
C(1)-Ir(1)-Pb(7)	164.2(3)	Pb(6)-Pb(7)-Pb(8)	92.213(13)
C(5)-Ir(1)-Pb(7)	83.1(3)	Pb(7)-Pb(8)-Pb(9)	87.787(12)
C(2)-Ir(1)-Pb(7)	151.3(3)	Pb(6)-Pb(9)-Pb(8)	91.054(13)
C(6)-Ir(1)-Pb(7)	85.0(3)	Pb(2)-Pb(1)-Pb(5)	65.181(13)

The  $[\text{Sn}_9\text{Ir}(\text{cod})]^{3-}$  and  $[\text{Pb}_9\text{Ir}(\text{cod})]^{3-}$  clusters described herein are the first Ir-Sn and Ir-Pb bimetallic clusters and are also examples of Sn-Pb homologues. Previous homologues include Fässler's  $[\text{Cu}@\text{Sn}_9]^{3-}$  and  $[\text{Cu}@\text{Pb}_9]^{3-}$  ions, the  $\text{E}_9\text{Mo}(\text{CO})_3^{4-}$  complexes,<sup>62-64</sup> and the *closo* clusters  $[\text{Sn}_9\text{M}(\text{Ar})]^{3-}$  and  $[\text{Pb}_9\text{M}(\text{Ar})]^{3-}$  where M = Zn, Cd; Ar = aryl, that also have silicon and germanium homologues.<sup>68,70</sup> The  $[\text{E}_9\text{Ir}(\text{cod})]^{3-}$  clusters described here are Wadian 10-vertex, 22-electron *closo* structures and are isostructural and isoelectronic to the  $\text{E}_9\text{M}(\text{CO})_3^{4-}$  series where M = Cr, Mo, W and to  $\{\text{Ge}_9[\text{Si}(\text{SiMe}_3)_3]_3\text{Cr}(\text{CO})_3\}^-$ .<sup>62-64,70,125</sup> Therefore, the clusters can be understood as  $\text{E}_9^{4-}$  ions bonded to  $\text{ML}_n^+$  capping groups.

It is informative to compare the  $[\text{E}_9\text{Ir}(\text{cod})]^{3-}$ ,  $[\text{Cu}@\text{E}_9]^{3-}$  and  $[\text{E}_9\text{Zn}(\text{C}_6\text{H}_5)]^{3-}$  clusters where E = Sn, Pb. While all 3 can be viewed as  $\text{ML}_n^+$  derivatives of the  $\text{E}_9^{4-}$  parent, the  $\text{Cu}^+$  ion occupies an interstitial site whereas the  $\text{Ir}(\text{cod})^+$  and  $\text{Zn}(\text{C}_6\text{H}_5)^+$  units occupy vertex sites. However, in each case, the  $\text{ML}_n^+$  units donate zero electrons to cluster bonding due to the fact that interstitial ions contribute valence electrons minus  $10 e^-$  and vertex units contribute valence electrons minus  $12 e^-$ . As such, the Cu complexes are best viewed as 22-electron 9-vertex *nido*- $\text{Cu}@\text{E}_9^{3-}$  clusters whereas the  $[\text{E}_9\text{Ir}(\text{cod})]^{3-}$  and  $[\text{E}_9\text{Zn}(\text{C}_6\text{H}_5)]^{3-}$  complexes form 22-electron 10-vertex *closo*- $\text{E}_9\text{ML}_n^{3-}$  structures. Interestingly, displacement of the neutral cod ligands from the  $[\text{E}_9\text{Ir}(\text{cod})]^{3-}$  clusters would give  $\text{E}_9\text{Ir}^{3-}$  binary complexes, which would presumably have 20-electron *closo* structure with two fewer electrons than the  $\text{Cu}@\text{E}_9^{3-}$  systems. However, such species have not been observed to date.

### 2.2.3. NMR Spectroscopic Studies

The  $^{13}\text{C}\{^1\text{H}\}$  NMR spectrum of the  $\text{Pb}_9\text{Ir}(\text{cod})^{3-}$  cluster (**2**) displays the resonances of crypt, the en solvates and residual toluene. The two cod signals appear at  $\delta = 34.6$  ppm and 70.6 ppm, which correspond to the methylene and olefinic carbons A and B, respectively (Figure 2.3). The assignments were aided by observing the proton-coupled spectrum in which the methylene carbon split into a triplet ( $^1J(^{13}\text{C}, ^1\text{H}) = 123$  Hz) and the alkenyl resonance split into a doublet ( $^1J(^{13}\text{C}, ^1\text{H}) = 151$  Hz) of similar intensity. The latter is obscured in the  $^{13}\text{C}\{^1\text{H}\}$  spectrum due to the similar chemical shift of the crypt resonance at  $\delta = 70.5$  ppm. Both resonances are deshielded relative to those of  $[\text{Ir}(\text{cod})\text{Cl}]_2$  at  $\delta = 32.3$  ppm and 62.2 ppm, respectively.

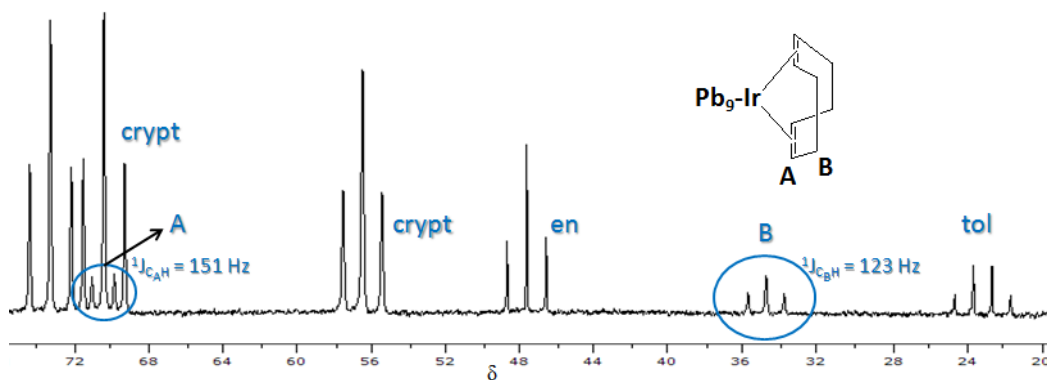


**Figure 2.3.**  $^{13}\text{C}$  NMR spectrum for the  $[\text{K}(2,2,2\text{-crypt})]_3[\text{Pb}_9\text{Ir}(\text{cod})]\cdot 2\text{en}$  salt. Data were recorded at 300 K at 125.8 MHz in Pyr- $d_5$ .

The  $^{13}\text{C}$  NMR spectrum of  $\text{Sn}_9\text{Ir}(\text{cod})^{3-}$  in pyridine shows a methylene chemical shift of  $\delta = 34.7$  ppm, which is very similar to that of  $\text{Pb}_9\text{Ir}(\text{cod})^{3-}$ . The second signal for A is obscured by the crypt resonance and has not been located.

The  $^1\text{H}$  NMR spectrum for the  $[\text{K}(2,2,2\text{-crypt})]_3[\text{Pb}_9\text{Ir}(\text{cod})]\cdot 2\text{en}$  salt contains three signals for the  $\text{Pb}_9\text{Ir}(\text{cod})^{3-}$  cluster as expected. The olefinic proton,



**a**, of the cod ligand has a chemical shift of  $\delta = 4.38$  ppm while the two diastereotopic protons, **b** and **c**, of the methylene carbon produce signals at 2.38 and 3.11 ppm. Because the proton signals were broad, the chemical shifts and peak assignments were made through the use of the  $^1\text{H}$ - $^{13}\text{C}$  HSQC spectrum as shown in Figure 2.4. Attempts to observe  $^{119}\text{Sn}$  and  $^{207}\text{Pb}$  NMR signals at various temperatures were unsuccessful despite the obvious diamagnetism of the compound.

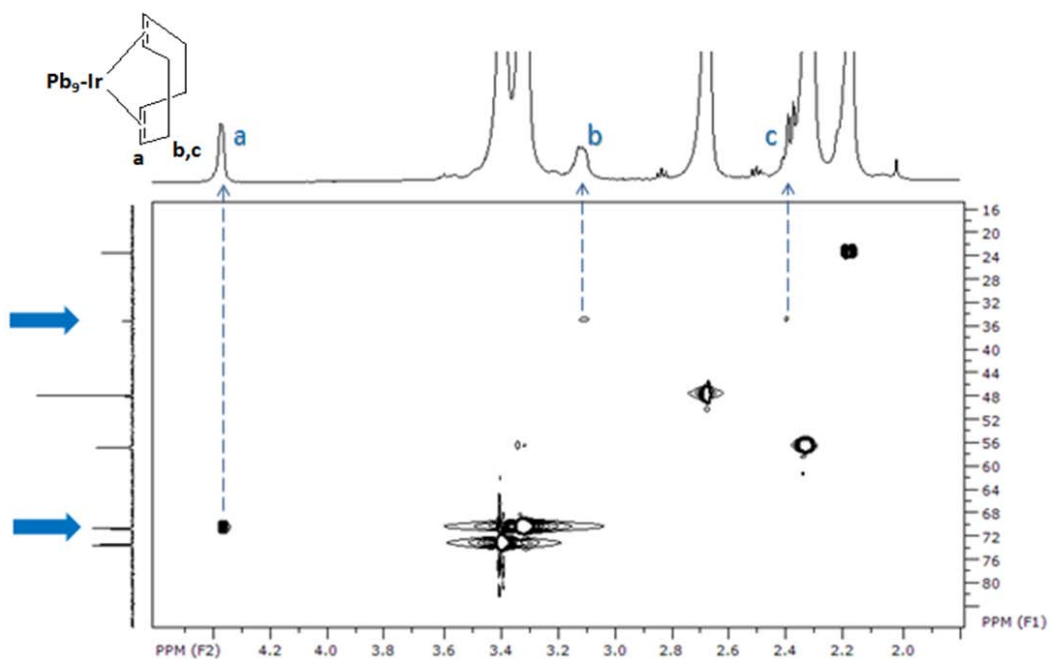


**Figure 2.4.** HSQC spectrum for the  $[\text{Pb}_9\text{Ir}(\text{cod})]^{3-}$  (**2**). Data was recorded at 300 K at 125.8 MHz in Pyr-d5.

Information on the charge distribution in the  $\text{E}_9\text{Ir}(\text{cod})^{3-}$  complex can be discerned from examination of the carbon-carbon bond distances of the cod ligands and their  $^{13}\text{C}$  NMR chemical shifts. Formal  $\pi$  back bonding interactions between the occupied Ir d-orbitals and the  $\text{C}=\text{C}$   $\pi^*$  anti-bonding orbitals effectively weakens the  $\text{C}=\text{C}$  bonds of the cod ligands and lengthens the olefinic bond.

Compared to other Ir(I)-cod complexes listed in Table 2.7, the average C=C bond length is quite long at 1.423(4) Å and is comparable with the [Ir(2,6-dioxo-1,2,3,6-tetrahydropyrimidino-4-carboxylato)(cod)]<sup>-1</sup> anion.<sup>126</sup> In addition, the <sup>13</sup>C NMR chemical shift of the olefinic carbons are shifted downfield relative to those of typical cod ligands. Collectively, these data are indicative of significant charge transfer to the cod ligands and denote a highly activated C=C double bond.

**Table 2.7.** Bond lengths (Å) and <sup>13</sup>C NMR Data of E<sub>9</sub>Ir(cod)<sup>3-</sup> and additional Ir-cod complexes.

	Ir-C	C=C	C-C	δ COD (ppm)	
				CH	CH <sub>2</sub>
[Sn <sub>9</sub> Ir(cod)] <sup>3-</sup> [124]	2.150	1.423	1.520	---	34.7
[Pb <sub>9</sub> Ir(cod)] <sup>3-</sup> [124]	---	---	---	70.6	34.6
[(hfac)Ir(cod)] [127]	2.101	1.409	1.511	62.0	30.9
[Ir(1,4-κ-CH=C(Ph)CH=CPh)(cod)(NCCH <sub>3</sub> )(PMe <sub>3</sub> )]BF <sub>4</sub> [128]	2.306	1.369	1.520	---	---
[(cod)Ir(κ <sup>2</sup> - <i>P,N</i> -indene)] <sup>+</sup> [129,130]	2.176	1.399	1.511	59.8, 93.4	28.8, 33.0
[(cod)Ir(κ <sup>2</sup> - <i>P,N</i> -indene)] [130]	---	---	---	54.6, 84.7	28.7, 32.8
[Ir(cod)(pyr)(PCy <sub>3</sub> )]PF <sub>6</sub> [131]	2.170	1.406	1.519	---	---
[NEt <sub>3</sub> H][Ir(HL)(cod)] [126]	2.115	1.428	1.513	---	---
[Ir(cod){Ph <sub>2</sub> Sb(CH <sub>2</sub> ) <sub>3</sub> SbPh <sub>2</sub> }]BF <sub>4</sub> [132]	---	---	---	63.8	36.5
[Ir(cod){ <i>o</i> -C <sub>6</sub> H <sub>4</sub> (CH <sub>2</sub> SbMe <sub>2</sub> ) <sub>2</sub> }]BF <sub>4</sub> [132]	---	---	---	59.2	33.6

cod = 1,5-cyclooctadiene; hfac = 1,1,1,5,5,5-hexafluoroacetylacetonate; pyr = pyridine; cy = cyclohexyl; H<sub>3</sub>L = 2,6-dioxo-1,2,3,6-tetrahydropyrimidine-4-carboxylic acid

Sn<sub>9</sub>Ir(cod)<sup>3-</sup> and Pb<sub>9</sub>Ir(cod)<sup>3-</sup> are both isostructural and isoelectronic to the previously studied group 6 metallated Sn<sub>9</sub>M(CO)<sub>3</sub><sup>4-</sup> ions (M = Cr, Mo, W),<sup>61,62</sup> and are therefore diamagnetic as shown by the observation of <sup>1</sup>H and <sup>13</sup>C NMR chemical shifts. The inability to locate <sup>119</sup>Sn and <sup>207</sup>Pb NMR signals in this study is quite possibly due to fluxionality within the two clusters; the fast molecular exchange of the atoms with respect to the NMR time scale can broaden or completely obscure the signals. Attempts to slow or stop the probable exchange via low temperature studies were unsuccessful, although Fässler and coworkers

reported that a  $^{119}\text{Sn}$  chemical shift of  $-1149$  ppm for  $\text{Sn}_9\text{Ir}(\text{cod})^{3-}$  is “sometimes” observed.<sup>123</sup>

The  $\text{Sn}_9\text{Rh}(\text{cod})^{3-}$  ion has been characterized by  $^{119}\text{Sn}$  NMR spectroscopy giving three broad signals at  $-542$ ,  $-380$ , and  $2472$  ppm (Figure 2.5). The chemical shifts of the signals are consistent with other known metallated  $\text{Sn}_9^{4-}$  cluster derivatives as summarized in Table 2.8. As in the case of the  $\text{Sn}_9\text{M}(\text{CO})_3^{4-}$  group 6 derivatives ( $\text{M} = \text{Cr}, \text{Mo}, \text{W}$ )<sup>62</sup> it is possible that the three signals are time-averaged signals resulting from the dynamic behavior of the cluster anion. The broadness of the signal also supports the possibility of fluxionality within the cluster, as the peak width at  $1/2$  height values range from  $135$ - $267$  Hz. The inability to discern  $^{119}\text{Sn}$ - $^{117}\text{Sn}$  and  $^{119}\text{Sn}$ - $^{103}\text{Rh}$  coupling constants is a result of the broadness of the signals.

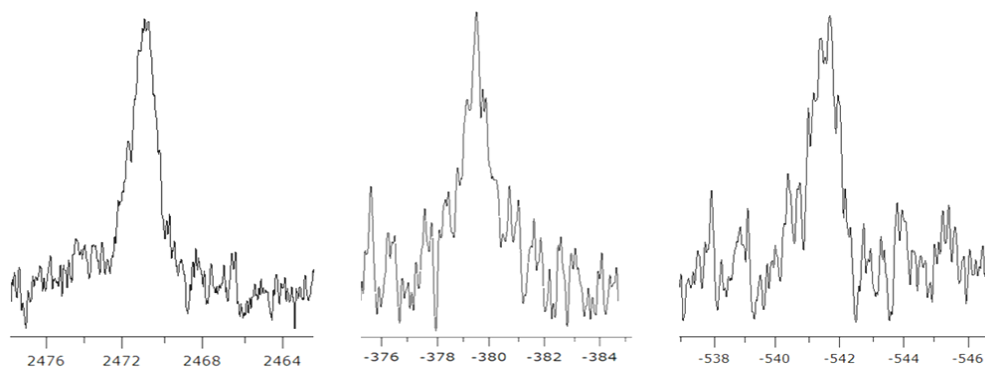


**Figure 2.5.**  $^{119}\text{Sn}$  NMR spectra of the  $\text{Sn}_9\text{Rh}(\text{cod})^{3-}$  (3). Data was recorded at  $298$  K at  $125.8$  MHz in an en/tol solution. The signals with a chemical shift  $\delta = +2471.7$ ,  $-379.5$ , and  $-541.7$  ppm possess peak widths at half-height  $\nu_{1/2} = 267$ ,  $135$ , and  $183$  Hz respectively.

**Table 2.8.** NMR studies of metallated derivatives of  $\text{Sn}_9^{4-}$ .

Cluster	$^{207}\text{Pb}$ $\delta$ (ppm)
$\text{Sn}_9\text{Rh}(\text{cod})^{3-}$	-552, -378, +2475
$\text{Sn}_9\text{Ir}(\text{cod})^{3-}$ [123]	-1149
$\text{Sn}_9\text{Cr}(\text{CO})_3^{4-}$ [62]	-440, -180, +2330
$\text{Sn}_9\text{Mo}(\text{CO})_3^{4-}$ [62]	-606, -361, +1988
$\text{Sn}_9\text{W}(\text{CO})_3^{4-}$ [62]	-660, -440, +2280
$\text{Sn}_9\text{Pt}_2(\text{PPh}_3)^{2-}$ [58]	-860

The dynamic process of the previously mentioned  $\text{Sn}_9\text{M}(\text{CO})_3^{4-}$  ions is described by the rotation of the triangular faces of the cluster, effectively exchanging the position of the  $\text{M}(\text{CO})_3$  units and creating  $\eta^4$  and  $\eta^5$  isomers.<sup>62</sup> The  $\text{Sn}_9\text{Rh}(\text{cod})^{3-}$  and  $\text{Sn}_9\text{Ir}(\text{cod})^{3-}$  ions are likely both involved in this mechanism. The three signals of the rhodium cluster indicate that it is engaged in a slower dynamic process than the iridium analogue. The erratic nature of the signal associated with the  $\text{Sn}_9\text{Ir}(\text{cod})^{3-}$  ion is not typical, nor is the chemical shift with respect to the other isostructural complexes. These irregularities were not discussed at length by Fässler, but the signal was simply described as a time-averaged signal.

### 2.3. Conclusion

Various group 9 derivatives of  $\text{Sn}_9^{4-}$  were synthesized and characterized by NMR spectroscopy and single crystal X-ray crystallography.  $\text{Sn}_9\text{Ir}(\text{cod})^{3-}$  and  $\text{Pb}_9\text{Ir}(\text{cod})^{3-}$  were the first Ir-Sn and Ir-Pb analogues studied, and both polyanions are isostructural to the previously studied  $\text{Sn}_9\text{M}(\text{CO})_3^{4-}$  group 6 derivatives where  $\text{M} = \text{Cr}, \text{Mo}, \text{W}$ .<sup>61,62</sup>  $^{119}\text{Sn}$  and  $^{207}\text{Pb}$  NMR signals for the analogues have yet to be located in these studies, although Fässler and coworkers explain that a signal

for  $\text{Sn}_9\text{Ir}(\text{cod})^{3-}$  is “sometimes” observed at -1149 ppm.<sup>123</sup> The clusters are unequivocally diamagnetic due to the electron count, which is also validated by  $^1\text{H}$  and  $^{13}\text{C}$  NMR studies; but it is likely that the clusters are highly fluxional in nature, in a manner similar to the  $\eta^4$ - $\eta^5$  interconversion process of  $\text{Sn}_9\text{W}(\text{CO})_3^{4-}$  which could hinder the observation of the signals. Conversely, the  $\text{Sn}_9\text{Rh}(\text{cod})^{3-}$  ion has been characterized via  $^{119}\text{Sn}$  NMR spectroscopy. The chemical shifts are similar to those of the aforementioned  $\text{Sn}_9\text{M}(\text{CO})_3^{4-}$  group 6 derivatives. It is likely that the three signals observed for the  $\text{Sn}_9\text{Rh}(\text{cod})^{3-}$  ion are of the cluster engaging in a slower dynamic process than the iridium analogue.

The  $\text{Sn}_9^{4-}$  transition metal derivatives described herein are precursors to the isolated  $\text{M}@\text{E}_{12}$  icosahedral Zintl clusters described next in Chapter 4, where  $\text{E} = \text{Sn}, \text{Pb}$  and  $\text{M} = \text{Rh}, \text{Ir}$ . Additionally, the oxidation of the  $\text{Sn}_9\text{Ir}(\text{cod})^{3-}$  ion to give the fabrication of the  $\text{Ir}_3\text{Sn}_7$  intermetallic phase as NPs for the first time will be discussed at length in Chapter 5.

## 2.4. Experimental Section

### 2.4.1. General Data

All reactions were performed in a nitrogen atmosphere dry box.  $^1\text{H}$  and  $^{13}\text{C}$  NMR spectra were recorded on a Bruker DRX 500 AVANCE spectrometer operating at 500.1 MHz and 125.8 MHz respectively.  $^{119}\text{Sn}$  spectra were recorded on a Bruker DRX500 AVANCE spectrometer at 186.5 MHz. The pulse sequence used for the  $^{119}\text{Sn}$  studies were the standard Bruker pulse programs with  $90^\circ$  pulse strength and 1.0 s relaxation delays were used. The  $^{119}\text{Sn}$  signals were confirmed

and verified by repeating the final measurements with different transmitter offsets. The  $^{119}\text{Sn}$  chemical shifts were referenced to the external  $\text{Me}_4\text{Sn}$  standard in  $\text{C}_6\text{D}_6$  (0 ppm) and at room temperature. The percentage yields were calculated by relative to the amount of  $\text{K}_4\text{Sn}_9$  or  $\text{K}_4\text{Pb}_9$  alloy precursor utilized.

#### **2.4.2. Chemicals**

$\text{K}_4\text{Sn}_9$ ,  $\text{Rb}_4\text{Sn}_9$ , and  $\text{K}_4\text{Pb}_9$  were made by the high-temperature fusion (~1000 °C) of stoichiometric amounts of the elements. The chemicals were loaded into evacuated, quartz tubes and carefully heated with a natural gas/oxygen flame behind a blast shield. Bis(1,5-cyclooctadiene)dirhodium(I) dichloride and bis(1,5-cyclooctadiene)diiridium(I) dichloride were purchased from Aldrich. 4,7,13,16,21,24-Hexaoxa-1,10-diazobicyclo[8.8.8]hexacacosane (2,2,2-crypt) and tetracobalt dodecacarbonyl were purchased from Fisher. Anhydrous ethylenediamine (en) and dimethylformamide (dmf) were purchased from Fisher, vacuum distilled from  $\text{K}_4\text{Sn}_9$ , and stored under dinitrogen. Toluene was purchased from Fisher and distilled from sodium/benzophenone under dinitrogen and stored under dinitrogen.

#### **2.4.3. Synthesis**

##### **Preparation of $[\text{K}(2,2,2\text{-crypt})]_3[\text{Sn}_9\text{Ir}(\text{cod})]\cdot 2\text{en}$**

In vial 1,  $\text{K}_4\text{Sn}_9$  (73 mg, 0.056 mmol) was dissolved in en (~2 mL), giving a dark red solution. Three equivalents of solid crypt (67 mg, 0.179 mmol) were added to the solution and allowed to stir for an hour. In vial 2,  $[\text{Ir}(\text{C}_8\text{H}_{12})\text{Cl}]_2$  (20 mg, 0.030 mmol) was dissolved in toluene (~2 mL) to produce an orange-yellow

solution. The contents of vial 2 were slowly added to vial 1 and the reaction mixture was stirred for 2 h to yield a dark brown solution. The reaction mixture was then filtered through tightly packed glass wool in a pipet. Black crystals formed in the reaction vessel after 2 weeks (44 mg, 27% yield).  $^{13}\text{C}$  NMR (125.8 MHz, Pyr-d<sub>5</sub>, 25 °C)  $\delta$  = 34.7 ppm.

#### **Preparation of [K(2,2,2-crypt)]<sub>3</sub>[Pb<sub>9</sub>Ir(cod)]•2en**

In vial 1, K<sub>4</sub>Pb<sub>9</sub> (179 mg, 0.089 mmol) was dissolved in en (~4 mL), giving a dark red solution. Three equivalents of solid crypt (100 mg, 0.266 mmol) were added to the solution and allowed to stir for an hour. In vial 2, [Ir(C<sub>8</sub>H<sub>12</sub>)Cl]<sub>2</sub> (30 mg, 0.044 mmol) was dissolved in toluene (~4 mL) to produce an orange-yellow solution. The contents of vial 2 were slowly added to vial 1 and the reaction mixture was stirred for 2 h to yield a dark brown solution. The reaction mixture was then filtered through tightly packed glass wool in a pipet. Black crystals formed in the reaction vessel after 1 week (100 mg, 32% yield).  $^1\text{H}$  NMR (500 MHz, Pyr-d<sub>5</sub>, 25 °C)  $\delta$  = 2.38, 3.11, 4.38;  $^{13}\text{C}$  NMR (125.8 MHz, Pyr-d<sub>5</sub>, 25 °C)  $\delta$  = 34.6 ( $^1\text{J}(^{13}\text{C}, ^1\text{H}) = 123$  Hz), 70.6 ( $^1\text{J}(^{13}\text{C}, ^1\text{H}) = 151$  Hz).

#### **Preparation of [Rb-crypt]<sub>3</sub>[Sn<sub>9</sub>Rh(cod)]•2en**

In vial 1, Rb<sub>4</sub>Sn<sub>9</sub> (94 mg, 0.066 mmol) and five equivalents of crypt were dissolved in en (~2 mL) and stirred about one hour minutes, giving a dark green solution. In vial 2, [Rh(C<sub>8</sub>H<sub>12</sub>)Cl]<sub>2</sub> (16 mg, 0.033 mmol) was dissolved in toluene (~2 mL) to produce a yellow solution. The contents of vial 2 were slowly added to vial 1 and the reaction mixture was stirred for 2 h to yield a dark brown

solution. The reaction mixture was then filtered through tightly packed glass wool in a pipet. Black crystals formed in the reaction vessel after 3 days (100 mg, 55% yield).  $^{119}\text{Sn}$  NMR (en, 25 °C)  $\delta$  (ppm) -541.7 ( $\Delta\nu_{1/2} = 183$  Hz), -379.5 ( $\Delta\nu_{1/2} = 135$  Hz), 2471.7 ( $\Delta\nu_{1/2} = 267$  Hz).

### **Crystallographic Studies**

The crystal structures of the clusters were determined at the single crystal X-ray facility by Dr. Peter Zavalij at the Department of Chemistry and Biochemistry, University of Maryland, College Park.



## Chapter 3: The Icosahedral $M@E_{12}^{3-}$ clusters ( $E = Sn, Pb$ ; $M = Ir, Rh$ )

### 3.1. Introduction

Large, naked MGE clusters have been of interest for their use as precursors to nanomaterials, with the ligand-free discrete clusters giving a precise handle on these potential materials for greater tunability.<sup>76,121,133</sup> Synthesizing and isolating clusters larger than the nine-atom, group 14 parent complexes  $E_9^{4-}$  ( $E = Ge, Sn, Pb$ ) has been a major goal in the field.<sup>77-84</sup> Computational studies suggested that the stable, icosahedral  $E_{12}^{4-}$  and bicapped antiprismatic  $E_{10}^{2-}$  ( $E = Si, Ge, Sn, Pb$ ) clusters could potentially be isolated.<sup>77-84</sup> The endohedral group 10 transition metal derivatives were also predicted to be stable and  $Ni@Pb_{10}^{2-}$  and  $M@Pb_{12}^{2-}$  ( $M = Ni, Pd, Pt$ ) were isolated shortly thereafter.<sup>52,85</sup> The fused deltahedra  $Pd_2@Sn_{18}^{4-}$  and  $M_2@Sn_{17}^{4-}$  ( $M = Ni, Pt$ ) are the largest stannide clusters isolated to date.<sup>74,98-100</sup>

This chapter describes our efforts to synthesize additional bimetallic Zintl clusters with nuclearities greater than nine, by targeting the incorporation of interstitial transition metals to add stability to larger clusters. This approach was carried out by first synthesizing novel bimetallic  $Sn_9ML_n$  clusters (see Chapter 2) to act as precursors to the high symmetry anions. As stated previously, the series of group 10 transition metals ( $Ni, Pd, Pt$ ) have all been incorporated into larger Zintl cluster anions, including the icosahedral  $M@Pb_{12}^{2-}$  cluster anions ( $M = Ni, Pd, Pt$ ) which are particularly reminiscent of the  $La@C_{60}$  fullerene.<sup>52,53,85</sup> This chapter describes our successes in expanding the series to include group 9 transition metal derivatives of the  $Sn_{12}^{2-}$  and  $Pb_{12}^{2-}$  ion, which are of interest due

to their catalytic and electrocatalytic applications of bimetallic Pt-group metals (Ru, Os, Rh, Ir, Pd, Pt).<sup>109,110</sup>

Recently, cobalt and iridium have been successfully incorporated into Zintl clusters to give  $\text{Co@Ge}_{10}^{3-}$ , the previously described  $\text{E}_9\text{Ir}(\text{cod})^{3-}$  ( $\text{E} = \text{Sn, Pb}$ ;  $\text{cod} = 1,5\text{-cyclooctadiene}$ ),  $\text{Sn}_9\text{Rh}(\text{cod})^{3-}$ , and  $\text{Ir@Sn}_{12}^{3-}$  all within the last two years.<sup>88,123,124</sup> In 2010, Fässler reported the synthesis and crystallographic characterization of the  $\text{Ir@Sn}_{12}^{3-}$  ion, showing the ability to synthesize the icosahedral cluster via the oxidation of crystalline  $\text{Sn}_9\text{Ir}(\text{cod})^{3-}$ , though NMR studies were not detailed at the time of publication.<sup>123</sup>

Each of the *closo* 12-atom Zintl clusters make up the so-called plumbaspherenes, and stannaspherenes for Pb and Sn derivatives, respectively. These cluster anions are remarkable because of their  $\sigma$ -aromaticity, which is a direct result of the ultra-high symmetry of the clusters. The  $I_h$  point symmetry of the clusters leads to degenerate d-orbitals over the equivalent 12 atoms. This degeneracy leaves the electrons free to circulate each d-orbital, making plumbaspherenes and stannaspherenes capable of sustaining diatropic ring currents and therefore making them aromatic by definition.<sup>134-137</sup> In the case of the previously isolated  $\text{M@Pb}_{12}^{2-}$  cluster anions ( $\text{M} = \text{Ni, Pd, Pt}$ ), the  $\sigma$ -aromaticity was witnessed by the extreme downfield chemical shift (1167-1780 ppm) of the  $^{207}\text{Pb}$  nuclei compared to other known lead-containing complexes (0 to -4000 ppm).<sup>52</sup>

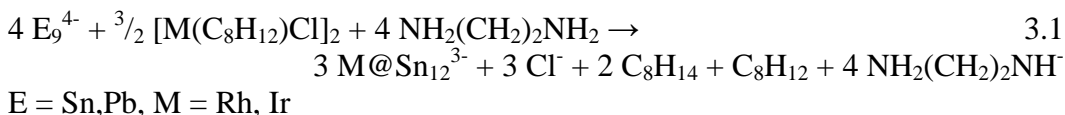
This chapter describes the synthesis and characterization of the high symmetry group 9 Zintl cluster derivatives  $\text{M@E}_{12}^{3-}$ , where  $\text{M} = \text{Rh, Ir}$  and  $\text{E} =$

Sn, Pb. The plumbaspherenes and rhodium stannaspherene are new members of the growing class of icosahedral Zintl clusters.  $^{119}\text{Sn}$  and  $^{207}\text{Pb}$  NMR studies of these clusters in addition to the  $\text{Ir@Sn}_{12}^{3-}$  cluster are also reported for the first time.

## 3.2. Results and Discussion

### 3.2.1. Synthesis

**Rh@Sn<sub>12</sub><sup>3-</sup> (3.1):** En solutions of  $\text{K}_4\text{Sn}_9$  react with tol solutions of  $[\text{Rh}(\text{cod})\text{Cl}]_2$  at 80 °C in the presence of five equivalents of crypt to give  $\text{Rh@Sn}_{12}^{3-}$  (**3.1**) ions as the  $[\text{K}(2,2,2\text{-crypt})]^+$  salt in *ca.* 68% yield (Eq. 3.1). Maximum yields are obtained by adding an en solution of  $[\text{Na}(2,2,2\text{-crypt})]\text{Cl}$  to the reaction solution to give a  $\text{K}^+$  to  $\text{Na}^+$  ratio of 4:3. A similar reaction involving Wilkinson's catalyst failed to produce ion **3.1**. Ion **3.1** is likely synthesized through the oxidation of the  $\text{Sn}_9\text{Rh}(\text{cod})^{3-}$  ion (Chapter 2). This synthetic pathway is akin to the step-by-step synthesis of the  $[\text{Ir@Sn}_{12}]^{3-}$  stannaspherene via the oxidation of crystalline  $\text{Sn}_9\text{Ir}(\text{cod})^{3-}$  as described by Fässler.<sup>123</sup>



**Rh@Pb<sub>12</sub><sup>3-</sup> (3.2):** En solutions of  $\text{K}_4\text{Pb}_9$  react with tol solutions of  $[\text{Rh}(\text{cod})\text{Cl}]_2$  in the presence of 2,2,2-crypt to give the  $\text{Rh@Pb}_{12}^{3-}$  (**3.2**) ion (Eq. 3.1). The  $[\text{K}(2,2,2\text{-crypt})]^+$  salt was isolated in *ca.* 53% yield. Though the  $[\text{Rh@Pb}_{12}]^{3-}$  cluster is likely formed through an intermediate such as  $\text{Pb}_9\text{Rh}(\text{cod})^{3-}$

, no such intermediate has been isolated to date. The  $[\text{K}(2,2,2\text{-crypt})]^+$  salt of **3.2** is air and moisture sensitive in solution and in the solid state. The salt is moderately soluble in en and dmf and has been characterized by single-crystal X-ray diffraction and  $^{207}\text{Pb}$  NMR spectroscopy.  $\text{Rh@Pb}_{12}^{3-}$  is the first isolated group 9 plumbaspherenes.

**Ir@Pb<sub>12</sub><sup>3-</sup> (3.3):** En solutions of  $\text{K}_4\text{Pb}_9$  react with tol solutions of  $[\text{Ir}(\text{cod})\text{Cl}]_2$  at 80 °C in the presence of excess 2,2,2-crypt to give the  $\text{Ir@Pb}_{12}^{3-}$  (**3.3**) ion presumably through a similar thermal oxidation of the previously reported  $\text{Pb}_9\text{Ir}(\text{cod})^{3-}$  intermediate.<sup>124</sup> The synthesis of  $\text{Ir@Pb}_{12}^{3-}$  also follows Eq 3.1 but the ion has not been isolated in the solid state. However,  $^{207}\text{Pb}$  NMR experiments of the reaction solutions provide compelling evidence for the plumbaspherene, with a markedly downfield chemical shift similar to that of **3.2**.

Fässler and coworkers reported the synthesis of  $\text{Ir@Sn}_{12}^{3-}$  as the oxidation of  $\text{Sn}_9\text{Ir}(\text{cod})^{3-}$  with 1,2-bis(diphenylphosphino)ethane (DPPE) as an oxidizing agent at elevated temperatures.<sup>123</sup> Attempts to use DPPE as an oxidizing agent in the synthesis of the  $\text{Ir@Pb}_{12}^{3-}$  ion led to a side reaction yielding the  $\text{Ir}(\text{DPPE})_2$  compound as the only isolated product. No reaction was observed in the attempted synthesis of  $\text{Rh@Pb}_{12}^{3-}$  with DPPE. Subsequent reactions at elevated temperatures (~80 °C), omitting DPPE, produced  $\text{Rh@Pb}_{12}^{3-}$  salts as the only product observable via crystallography and NMR spectroscopy. Additionally, the observation of  $[\text{Ir@Pb}_{12}]^{3-}$  via NMR suggests that the cluster is synthesized through the thermal oxidation of  $\text{Pb}_9\text{Ir}(\text{cod})^{3-}$ .

### 3.2.2. Solid State Structure

The  $[\text{K}(2,2,2\text{-crypt})]_3[\text{Rh@Sn}_{12}] \cdot \text{tol}$  salt is monoclinic, space group Cm. The  $\text{Rh@Sn}_{12}^{3-}$  ion (**3.1**) is shown in Figure 3.1. The crystallographic data for the  $\text{Rh@Sn}_{12}^{3-}$  anion is described in Table 3.1 and selected bond distances and angles are summarized in and Table 3.2. Anion **3.1** possesses a 12 vertex icosahedral cage with a formal Rh(-1) centered ion. The structure and electronics of **1** are therefore very similar to the  $I_h$   $\text{Ir@Sn}_{12}^{3-}$  ion reported by Fässler.<sup>123</sup> The icosahedral ions have 26 cluster bonding electrons, indicative of a *closo* structure according to Wade's rules (each Sn = 2 e-, Rh = -1 e-, charge = 3 e-).<sup>59</sup> The Sn-Sn bonds are in the range of 2.7243(8)- 3.3038(6) Å, averaging 3.035 Å (*d*). The Rh-Sn bonds are in the range of 2.7664(6)-3.0558(6) Å, with an average bond length of 2.890 Å (*R*). This gives a calculated *R/d* ratio of 0.952, which is close to the ideal value of 0.951 for icosahedra.<sup>13</sup> The data compares well to the  $\text{Ir@Sn}_{12}^{3-}$  ion, which has an average Ir-Sn and Sn-Sn bond length of 3.065 Å and 2.922 Å, respectively, and an *R/d* ratio of 0.953.<sup>123</sup>

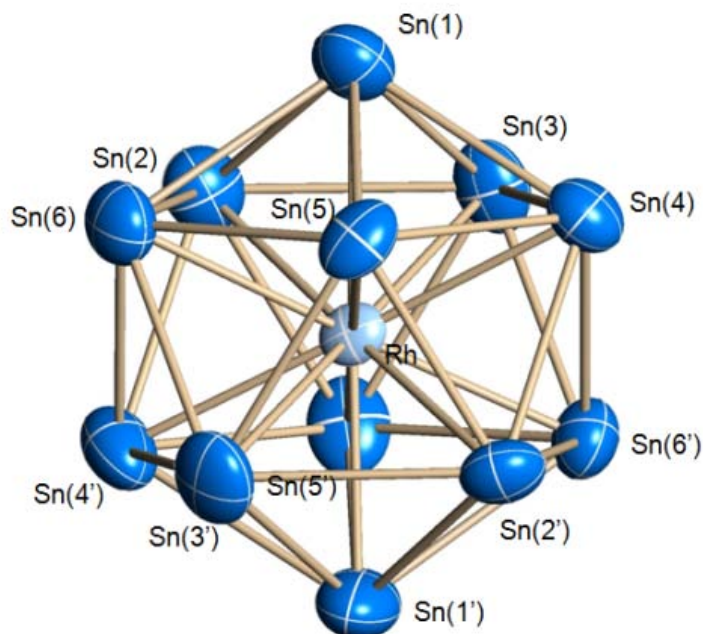


**Figure 3.1.** Preliminary structure of the  $\text{Rh@Sn}_{12}^{3-}$  ion (**3.1**). Thermal ellipsoids drawn at the 50% probability level.

**Table 3.1.** Crystallographic Data for  $\text{Rh@Sn}_{12}^{3-}$  and  $\text{Rh@Pb}_{12}^{3-}$ .

Compound	$[\text{K}(2,2,2\text{-crypt})]_3$ [ $\text{Rh@Sn}_{12}$ ]	$[\text{K}(2,2,2\text{-crypt})]_3$ [ $\text{Rh@Pb}_{12}$ ]
temperature (K)	150(2)	150(2)
Wavelength ( $\text{\AA}$ )	0.71073	0.71073
crystal system	monoclinic	monoclinic
space group	Cm	C2/c
unit cell dimensions		
a ( $\text{\AA}$ )	29.773(9)	22.816(3)
b ( $\text{\AA}$ )	42.27(1)	18.419(2)
c ( $\text{\AA}$ )	30.36(1)	48.796(6)
$\alpha$ ( $^\circ$ )	90	90
$\beta$ ( $^\circ$ )	96.567(5)	92.863(1)
$\gamma$ ( $^\circ$ )	90	90
volume ( $\text{\AA}^3$ )	37965.2	20481.4

**Table 3.2.** Selected Bond Lengths (Å) and Angles (°) for the Rh@Sn<sub>12</sub><sup>3-</sup> Ion.<sup>a</sup>

Rh(1)-Sn(1)	2.8325(8)	Sn(1)-Sn(2)	3.2862(8)
Rh(1)-Sn(2)	2.957(1)	Sn(1)-Sn(3)	3.1443(7)
Rh(1)-Sn(3)	2.9105(7)	Sn(1)-Sn(4)	2.8735(6)
Rh(1)-Sn(4)	2.9461(5)	Sn(1)-Sn(5)	2.8362(8)
Rh(1)-Sn(5)	2.8882(5)	Sn(1)-Sn(6)	2.9999(7)
Sn(1)-Rh(1)-Sn(1')	178.83	Sn(2)-Rh(1)-Sn(4)	113.28
Sn(1)-Rh(1)-Sn(2)	69.12	Sn(2)-Sn(1)-Sn(3)	60.34
Sn(1)-Rh(1)-Sn(2')	113.71	Sn(2)-Sn(1)-Sn(4)	106.16
Sn(2)-Rh(1)-Sn(3)	66.89	Rh(1)-Sn(2)-Sn(1)	53.65

<sup>a</sup> Preliminary data. Refinement in progress.

The [K(2,2,2-crypt)]<sub>3</sub>[Rh@Pb<sub>12</sub>] salt is monoclinic, space group C2/c. The [Rh@Pb<sub>12</sub>]<sup>3-</sup> ion (**3.2**) is shown in Figure 3.2. The crystallographic data for [Rh@Pb<sub>12</sub>]<sup>3-</sup> is described in Table 3.1 and selected bond distances and angles for the ion are given in Table 3.3. The structure of anion **3.2** is made up of a *closo*-12 vertex icosahedral framework containing an encapsulated Rh(-1) ion, as in the case of the stannaspherene analogue. The icosahedral cage of **3.2** is therefore similar to the *I<sub>h</sub>* M@Pb<sub>12</sub><sup>2-</sup> ions.<sup>52,85</sup> The *closo*-12 vertex deltahedron possess 26 cluster electrons, consistent with Wade's rules (each Pb = 2 e-, Rh = -1 e-, charge = 3 e-).<sup>59</sup> The Pb-Pb bonds are in the narrow range of 3.1454(2)-3.1936(4) Å, averaging 3.170 Å (*d*) with a narrow range as expected for the nearly spherical plumbaspherene. Likewise, the Rh-Pb bonds are in a precise range of 2.9861(2)-3.0346(3) Å with an average bond length of 3.014 Å (*R*). These metric parameters give a calculated *R/d* ratio of 0.951, which is very close to the ideal value of 0.951.<sup>13</sup>

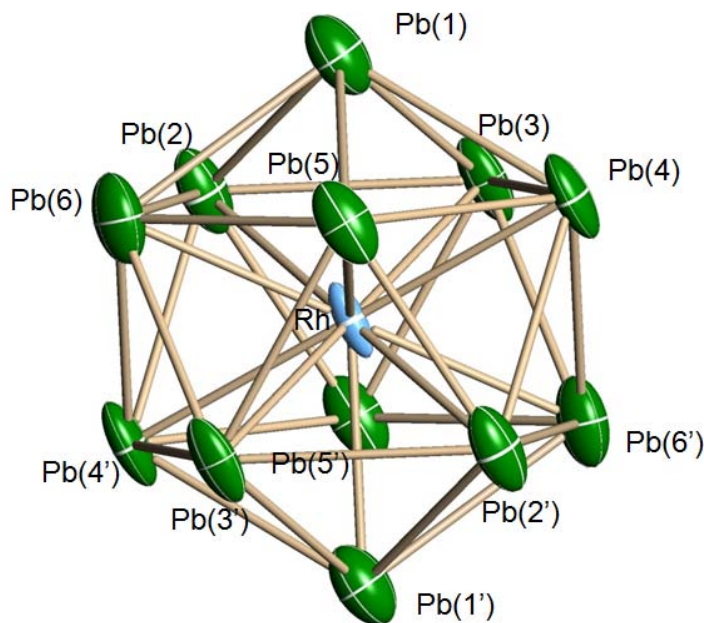


**Figure 3.2.** Preliminary structure of the  $\text{Rh@Pb}_{12}^{3-}$  ion (1). Thermal ellipsoids drawn at the 50% probability level.

**Table 3.3.** Selected Bond Lengths [Å] and Angles [deg] for the  $\text{Rh@Pb}_{12}^{3-}$  Ion.<sup>a</sup>

Rh(1)-Pb(1)	3.0228(3)	Pb(1)-Pb(2)	3.1464(3)
Rh(1)-Pb(2)	2.9861(2)	Pb(1)-Pb(3)	3.1557(3)
Rh(1)-Pb(3)	3.0230(3)	Pb(1)-Pb(4)	3.1761(3)
Rh(1)-Pb(4)	3.0346(3)	Pb(1)-Pb(5)	3.1722(3)
Rh(1)-Pb(5)	3.0048(3)	Pb(1)-Pb(6)	3.1936(4)
Pb(1)-Rh(1)-Pb(1')	180.00	Pb(2)-Rh(1)-Pb(4)	116.42
Pb(1)-Rh(1)-Pb(2)	57.86	Pb(2)-Pb(1)-Pb(3)	60.28
Pb(1)-Rh(1)-Pb(2')	116.35	Pb(2)-Pb(1)-Pb(4)	108.08
Pb(2)-Rh(1)-Pb(3)	63.55	Rh(1)-Pb(2)-Pb(1)	59.00

<sup>a</sup> Preliminary data. Refinement in progress.

The icosahedral  $\text{Pb}_{12}^{2-}$  framework of  $\text{Rh@Pb}_{12}^{3-}$  is consistent with the group 10 (Ni, Pd, Pt) derivatives, where the average Pb-Pb bond length falls in the average range of 3.078(9)-3.216(12) Å with the  $\text{Pb}_{12}^{2-}$  cage contracting when housing a smaller atom.<sup>52</sup> The average Pb-Pb bond distance of 3.170 Å (ave) in  $\text{Rh@Pb}_{12}^{3-}$  falls in between the Pb-Pb bonds of  $\text{Ni@Pb}_{12}^{3-}$  and  $\text{Pd@Pb}_{12}^{3-}$ . Likewise, the Rh-Pb bond follows the same trend where the various M-Pb bonds



are 3.001(24)-3.058(7) Å in length. The formal Rh(-1) ion forms a 3.014 Å (ave) Rh-Pb bond that is shorter than the 3.033(7) Å Pd-Pb bond of Pd@Pb<sub>12</sub><sup>3-</sup>.

### 3.2.3. NMR Spectroscopic Studies

The <sup>207</sup>Pb NMR spectroscopy experiments reveal a single signal for Rh@Pb<sub>12</sub><sup>3-</sup> and Ir@Pb<sub>12</sub><sup>3-</sup>, as expected from the 12 chemically equivalent Pb atoms of the two M@Pb<sub>12</sub><sup>3-</sup> icosahedra. The Rh complex gives rise to a broad signal at +2293 ppm, located downfield relative to the known group 10 M@Pb<sub>12</sub><sup>2-</sup> clusters (Figure 3.3). The J<sub>207Pb-103Rh</sub> coupling could not be resolved with certainty ( $\Delta\nu_{1/2} = 804$  Hz, at 25 °C, <sup>103</sup>Rh, I = 1/2, 100% abund.) and can be assumed to be less than 150 Hz. The coupling resolution is limited due to the broadness of the signal and the small coupling constant, although no Rh-Pb coupling constants have been reported in the literature for comparison.

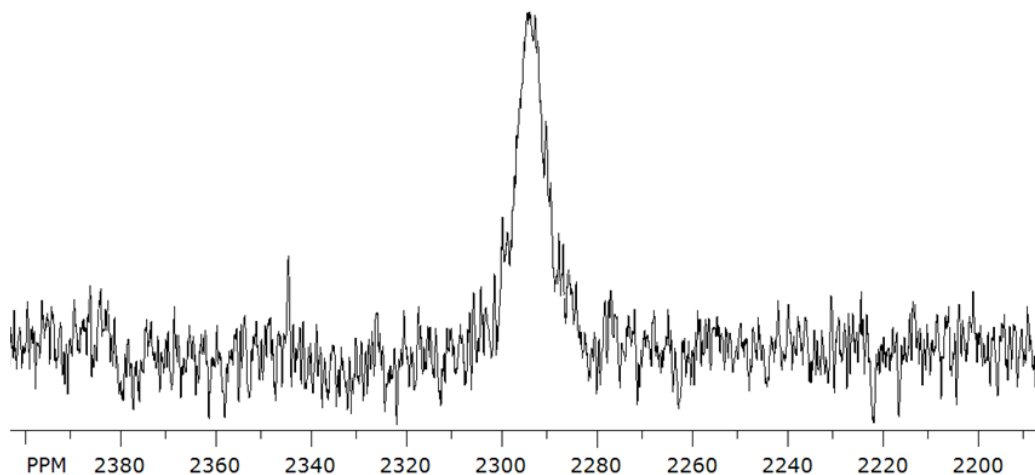


**Figure 3.3.** <sup>207</sup>Pb NMR spectrum for the Rh@Pb<sub>12</sub><sup>3-</sup> (**3.2**) ion. Data was recorded at 104.9 MHz from an en solution at room temperature.

The Ir@Pb<sub>12</sub><sup>3-</sup> anion was observed via <sup>207</sup>Pb NMR at +2650 ppm (Figure 3.4) as a broad signal ( $\Delta\nu_{1/2} = 324$  Hz, at 25 °C). While the two spin-active iridium nuclei are both quadrupolar (<sup>191</sup>Ir, I = 3/2, 38.5% abund.; <sup>193</sup>Ir, I = 3/2, 61.5% abund.), coupling to iridium is expected due to the icosahedral environment of the cluster anion. The Ir@Pb<sub>12</sub><sup>3-</sup> anion has not yet been isolated in the solid state, but the similarity in chemical shift to the rhodium analogue allows the identification of the plumbide with confidence. It is the most downfield <sup>207</sup>Pb NMR signal known to date.

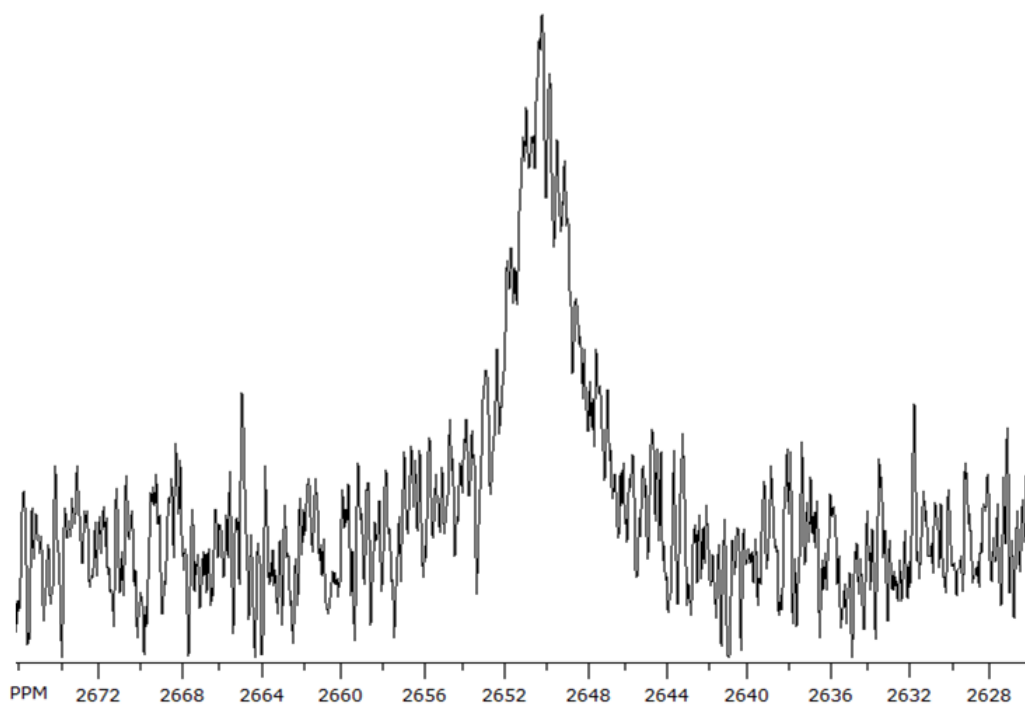


**Figure 3.4.** <sup>207</sup>Pb NMR spectrum for the Ir@Pb<sub>12</sub><sup>3-</sup> (**3.3**) ion. Data was recorded at 104.9 MHz from an en solution at room temperature.

Like the other 12-vertex plumbides, the Rh and Ir icosahedra are tremendously downfield compared to other known lead compounds, due to the presumed  $\sigma$ -aromaticity of the high symmetry cluster cage.<sup>52,87,134,135</sup> The <sup>207</sup>Pb chemical shifts of the group 10 M@Pb<sub>12</sub><sup>2-</sup> icosahedra range from +1167-1780

ppm, giving the complexes isolated in this work the most downfield  $^{207}\text{Pb}$  NMR chemical shift to date to our knowledge. Lower symmetry Zintl plumbides fall in the typical range for lead compounds of  $\sim 0$  to  $-4500$  ppm as summarized in Table 3.4.

**Table 3.4.**  $^{207}\text{Pb}$  NMR Data for  $\text{Rh@Pb}_{12}^{3-}$ ,  $\text{Ir@Pb}_{12}^{3-}$ , and other Plumbides.

Cluster Anion	$^{207}\text{Pb}$ $\delta$ (ppm)
$[\text{Ir@Pb}_{12}]^{3-}$	+2650
$[\text{Rh@Pb}_{12}]^{3-}$	+2293
$[\text{Pt@Pb}_{12}]^{2-}$ [85]	+ 1780
$[\text{Pd@Pb}_{12}]^{2-}$ [52]	+ 1520
$[\text{Ni@Pb}_{12}]^{2-}$ [52]	+ 1167
$[\text{Ni@Pb}_{10}]^{2-}$ [52]	-996
$[\text{Pb}_9]^4$ [138]	- 4098
$[\text{Pb}_9\text{Mo}(\text{CO})_3]^4$ [64]	-3450, -1934, +27

$\text{Ir@Sn}_{12}^{3-}$  has also been synthesized by using elevated temperatures to oxidize  $\text{Sn}_9\text{Ir}(\text{cod})^{3-}$  precursors *in situ*. The  $\text{Ir@Sn}_{12}^{3-}$  anion was observed via  $^{119}\text{Sn}$  NMR at  $-4$  ppm as a broad 2<sup>nd</sup> order signal ( $\Delta\nu_{1/2} = 530$  Hz, at  $25$  °C) and is also devoid of any apparent  $^{191/193}\text{Ir}$  coupling (Figure 3.5a). No  $^{119}\text{Sn}$  NMR chemical shifts have been observed for the  $\text{Rh@Sn}_{12}^{3-}$  ion to date.

In attempt to reduce the 2<sup>nd</sup> order effects in the  $\text{Ir@Sn}_{12}^{3-}$   $^{119}\text{Sn}$  NMR spectrum and resolve the  $^{119}\text{Sn}$ - $^{191/193}\text{Ir}$  coupling, a custom-made Bruker Quad nuclei inverse probe was employed to perform a  $^{119}\text{Sn}\{^{117}\text{Sn}\}$  NMR experiment (Figure 3.5b). The probe contains a  $^1\text{H}$  inner observe coil while there are two outer coils, one being a standard broad band coil and the second coil is fixed for  $^{117}\text{Sn}$  nuclei. The broad band coil is tunable to the desired  $^{119}\text{Sn}$  frequency, allowing the observation of  $^{119}\text{Sn}$  spectra using the probe, while the  $^{117}\text{Sn}$  coil

provides the ability to produce  $^{119}\text{Sn}\{^{117}\text{Sn}\}$  NMR spectra. This is a powerful tool that has been used in successfully solving the structure of  $\text{Pt@Sn}_9\text{H}^{3-}$  via the use of  $^1\text{H}\{^{119/117}\text{Sn}\}$  and  $^1\text{H}\{^{195}\text{Pt}\}$  NMR experiments (broad band coil tuned to  $^{119}\text{Sn}$  and  $^{195}\text{Pt}$ , respectively).<sup>74</sup>

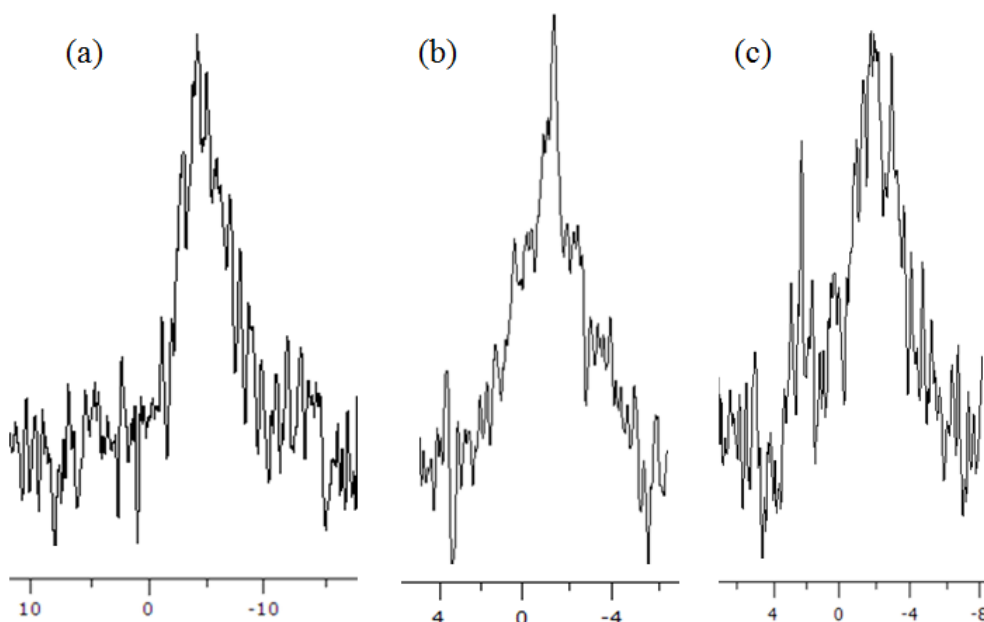


**Figure 3.5.** (a)  $^{119}\text{Sn}$ , (b)  $^{119}\text{Sn}\{^{117}\text{Sn}\}$ , and (c)  $^{117}\text{Sn}$  NMR experiments of the  $\text{Ir@Sn}_{12}^{3-}$  ion.  $^{119}\text{Sn}\{^{117}\text{Sn}\}$  and  $^{117}\text{Sn}$  spectra recorded using a custom-made Quad-inverse probe.

The  $^{119}\text{Sn}\{^{117}\text{Sn}\}$  NMR spectrum of  $\text{Ir@Sn}_{12}^{3-}$  is still particularly broad but resembles that of the  $\text{Ir@Pb}_{12}^{3-}$  ion and is still marked by 2<sup>nd</sup> order effects. The similarity in the spectra stems from the fact that the two clusters are isostructural. Neither spectra show coupling to  $^{191/193}\text{Ir}$  nuclei, which would give a 1:1:1:1 4-line multiplet exhibited by both nuclei. The 2<sup>nd</sup> order effects possibly arise from the clusters having a static structure, which differs from the previously isolated  $\text{M@Pb}_{12}^{2-}$  ( $\text{M} = \text{Ni}, \text{Pd}, \text{Pt}$ ) plumbaspherenes. The group 10 analogues

are highly dynamic and give relatively narrow spectra with observable coupling to  $^{195}\text{Pt}$  in the case of  $\text{Pt}@\text{Pb}_{12}^{2-}$ .

### 3.3. Conclusion

The synthesis and characterization of the high symmetry  $\text{M}@\text{E}_{12}^{3-}$  ( $\text{M} = \text{Rh}, \text{Ir}$  and  $\text{E} = \text{Sn}, \text{Pb}$ ) Zintl ions have been described. The  $\text{Rh}@\text{Sn}_{12}^{3-}$  and  $\text{Rh}@\text{Pb}_{12}^{3-}$  ions were isolated in the solid state and characterized crystallographically, showing the  $I_h$  point symmetry of the clusters common to the previously isolated group 10 dianionic lead analogues. This symmetry gives the ions aromatic character due to the ability of the electrons in the valence shell to circulate freely over the 12 degenerate d-orbitals in the icosahedral clusters. The  $\text{Rh}@\text{Pb}_{12}^{3-}$  and  $\text{Ir}@\text{Pb}_{12}^{3-}$  ions were both observed in solution via  $^{207}\text{Pb}$  NMR spectroscopy, giving chemical shifts of +2293 ppm and +2650 ppm, respectively. The extreme downfield chemical shifts are indicative of the expected  $\sigma$ -aromatic character of the ions. The  $\text{Rh}@\text{Sn}_{12}^{3-}$  ion has not yet been observed by  $^{119}\text{Sn}$  NMR spectroscopy but the chemical shift of the  $\text{Ir}@\text{Sn}_{12}^{3-}$  anion, previously isolated by Fässler,<sup>123</sup> has been located at -4 ppm. The  $\text{Ir}@\text{Sn}_{12}^{3-}$  anion is the first stannaspherene characterized via NMR spectroscopy. As a result, it is not clear if the chemical shift is in the optimal region for  $\sigma$ -aromatic stannides, although there are stannides with chemical shifts downfield relative to  $\text{Ir}@\text{Sn}_{12}^{3-}$ . The  $\text{Sn}_9\text{M}(\text{CO})_3^{4-}$  clusters where  $\text{M} = \text{Cr}, \text{Mo}, \text{W}$  for example each have one tin atom in the cluster with a chemical shift above +2300 pm though the weighted average chemical shifts of the clusters are upfield relative to the  $\text{Ir}@\text{Sn}_{12}^{3-}$  chemical shift.<sup>62</sup>

## 3.4. Experimental Section

### 3.4.1. General Data

All reactions were performed in a nitrogen atmosphere dry box.  $^{119}\text{Sn}$  and  $^{207}\text{Pb}$  NMR spectra were recorded on a Bruker DRX500 AVANCE spectrometer at 186.5 MHz and 104.6 MHz respectively. The pulse sequence used for the  $^{119}\text{Sn}$  and  $^{207}\text{Pb}$  NMR studies were the standard Bruker pulse programs with  $90^\circ$  pulse strength and 1.0 s relaxation delays were used. The signals were confirmed and verified by repeating the final measurements with different transmitter offsets. The  $^{119}\text{Sn}$  chemical shifts were referenced to the external  $\text{Me}_4\text{Sn}$  standard in  $\text{C}_6\text{D}_6$  (0 ppm) and the  $^{207}\text{Pb}$  shifts were referenced to 1 M  $\text{Pb}(\text{NO}_3)_2$  (0 ppm) at room temperature. Selective  $^{119}\text{Sn}/^{117}\text{Sn}$  decoupling experiments were conducted on a Bruker DRX 500 AVANCE spectrometer with a custom-made Bruker Quad nuclei inverse probe in which the inner observe coil is fixed for  $^1\text{H}$  observation. One of the outer coils is fixed for  $^{117}\text{Sn}$ , and the other outer coil is a broad band (tunable to  $^{119}\text{Sn}$ ) depending on the desirable decoupling nucleus. The pulse sequence used was modified from the standard Bruker “zgdc” by adding a third nucleus for simultaneous decoupling. The percentage yields were calculated relative to the amount of  $\text{K}_4\text{Sn}_9$  or  $\text{K}_4\text{Pb}_9$  alloy precursor utilized.

### 3.4.2. Chemicals

$\text{K}_4\text{Sn}_9$  and  $\text{K}_4\text{Pb}_9$  were made by the high-temperature fusion ( $\sim 1000^\circ\text{C}$ ) of stoichiometric amounts of the elements. The chemicals were loaded into

evacuated, quartz tubes and carefully heated with a natural gas/oxygen flame behind a blast shield. Bis(1,5-cyclooctadiene)dirhodium(I) dichloride, bis(1,5-cyclooctadiene)diiridium(I) dichloride, and tris(triphenylphosphine)rhodium(I) chloride (Wilkinson's catalyst) were purchased from Aldrich. 4,7,13,16,21,24-Hexaoxa-1,10-diazobicyclo[8.8.8]hexacacosane (2,2,2-crypt) was purchased from Fisher. Anhydrous ethylenediamine (en) and dimethylformamide (dmf) were purchased from Fisher, vacuum distilled from  $K_4Sn_9$ , and stored under dinitrogen. Toluene was purchased from Fisher and distilled from sodium/benzophenone under dinitrogen and stored under dinitrogen.

### 3.4.3. Synthesis

#### Preparation of $[K(2,2,2-crypt)]_3[Rh@Sn_{12}]^{3-}$

In vial 1,  $K_4Sn_9$  (81 mg, 0.066 mmol) was dissolved in en (~2 mL), giving a dark red solution. Five equivalents of solid crypt (125 mg, 0.332 mmol) were added to the solution and allowed to stir for about 10 minutes. In vial 2,  $[Rh(C_8H_{12})Cl]_2$  (25 mg, 0.050 mmol) was dissolved in toluene (~2 mL) to produce a yellow solution. The contents of vial 2 were slowly added to vial 1 and the reaction mixture was stirred for 2 h at room temperature to yield a dark greenish-brown solution. The solution was then heated to 80 °C and stirred for an additional hour. The reaction mixture was then filtered through tightly packed glass wool and a solution of NaCl (11 mg, 0.199 mmol) and crypt (75 mg, 0.199 mmol) in en (~1 mL) was added and stirred for 10 min. Dark crystals were isolated in the reaction vessel (135 mg, 68% yield).

### Preparation of [Ir@Sn<sub>12</sub>]<sup>3-</sup>

Synthesis adapted from reaction reported by Fässler *et al.* In vial 1, K<sub>4</sub>Pb<sub>9</sub> (179 mg, 0.086 mmol) was dissolved in en (~2 mL), giving a dark red solution. Three equivalents of solid crypt (100 mg, 0.266 mmol) were added to the solution and allowed to stir for about 10 minutes. In vial 2, [Ir(C<sub>8</sub>H<sub>12</sub>)Cl]<sub>2</sub> (30 mg, 0.044 mmol) was dissolved in toluene (~2 mL) to produce an orange solution. The contents of vial 2 were slowly added to vial 1 and the reaction mixture was stirred for 2 h at room temperature to yield a dark brown solution. The solution was then heated to ~90 °C and stirred for an additional hour. The reaction mixture was then filtered through tightly packed glass wool. <sup>119</sup>Sn NMR (en, 25 °C) δ (ppm) -4, Δv<sub>1/2</sub> = 530 Hz.

### Preparation of [K(2,2,2-crypt)]<sub>3</sub>[Rh@Pb<sub>12</sub>]

In vial 1, K<sub>4</sub>Pb<sub>9</sub> (134 mg, 0.066 mmol) was dissolved in en (~2 mL), giving a dark brown solution. Five equivalents of solid crypt (125 mg, 0.332 mmol) were added to the solution and allowed to stir for about 10 minutes. In vial 2, [Rh(C<sub>8</sub>H<sub>12</sub>)Cl]<sub>2</sub> (16 mg, 0.033 mmol) was dissolved in toluene (~2 mL) to produce a yellow solution. The contents of vial 2 were slowly added to vial 1 and the reaction mixture was stirred for 2 h to yield a dark greenish-brown solution. The reaction mixture was then filtered through tightly packed glass wool. Dark crystals formed in the reaction vessel after 3 weeks (99.5 mg, 53% yield). <sup>207</sup>Pb NMR (en, 25 °C) δ (ppm) 2293, Δv<sub>1/2</sub> = 804 Hz.



### **Preparation of [Ir@Pb<sub>12</sub>]<sup>3-</sup>**

In vial 1, K<sub>4</sub>Pb<sub>9</sub> (179 mg, 0.089 mmol) was dissolved in en (~2 mL), giving a dark red solution. Three equivalents of solid crypt (100 mg, 0.266 mmol) were added to the solution and allowed to stir for about 10 minutes. In vial 2, [Ir(C<sub>8</sub>H<sub>12</sub>)Cl]<sub>2</sub> (30 mg, 0.044 mmol) was dissolved in toluene (~2 mL) to produce a yellow solution. The contents of vial 2 were slowly added to vial 1 and the reaction mixture was stirred for 2 h at room temperature to yield a dark brown solution. The solution was then heated to 80 °C and stirred for an additional hour. The reaction mixture was then filtered through tightly packed glass wool. <sup>207</sup>Pb NMR (en, 25 °C) δ (ppm) 2650, Δ<sub>v<sub>1/2</sub></sub> = 324 Hz.

### **Crystallographic Studies**

The crystal structures of the clusters were determined at the single crystal X-ray facility by Dr. Peter Zavalij at the Department of Chemistry and Biochemistry, University of Maryland, College Park.

# Chapter 4: The Use of the $E_9^{4-}$ and $E_7^{3-}$ Zintl Ions as Electron Transfer Reagents: The Synthesis of the Novel $[\text{Rh}_2\text{H}(\text{PPh}_2)_2(\text{PPh}_3)_3]^-$ , $\text{Co}_3(\text{CO})_7^{3-}$ , and $[(\text{C}_3\text{H}_7\text{N}_2\text{O})_3\text{Ir}_4(\text{CO})_9]^{3-}$ Ions

## 4.1. Introduction

Interesting new clusters involving the group 9 transition metals such as  $\text{Co@Ge}_{10}^{3-}$ ,<sup>88</sup>  $E_9\text{Ir}(\text{cod})^{3-}$  ( $E = \text{Sn}, \text{Pb}$ ),<sup>123,124</sup>  $\text{Sn}_9\text{Rh}(\text{cod})^{3-}$ ,  $\text{Ir@Sn}_{12}^{3-}$ ,<sup>123</sup> and  $\text{M@Pb}_{12}^{3-}$  ( $M = \text{Rh}, \text{Ir}$ ) have been isolated or targeted recently by our group and others as detailed in the previous chapters. The parent Zintl ions behave as electrophiles in these reactions. However, it is known that the  $E_9^{4-}$  and  $E_7^{3-}$  ions can be reducing, such as in the case of the reduction of  $\text{M}(\text{CO})_6$  to  $\text{M}(\text{CO})_5^{2-}$  ( $M = \text{Cr}, \text{Mo}, \text{W}$ ). Therefore we generally attempt to incorporate “non-reducible precursors” such as  $\text{Ni}(\text{cod})_2$ ,  $\text{M}(\text{arene})(\text{CO})_3$ , and  $\text{M}(\text{PR}_3)_4$  ( $M = \text{Pt}, \text{Pd}$ ) to circumvent electron transfer chemistry. However a number of “byproducts” were isolated as the major product due to the reductive degeneration of the group 9 precursors.

Rhodium-substituted Zintl clusters were targeted via the reaction of  $\text{K}_4\text{Sn}_9$  and  $\text{K}_4\text{Pb}_9$  with various Rh complexes, namely  $\text{Rh}_4(\text{CO})_{12}$ ,  $[\text{Rh}(\text{cod})\text{Cl}]_2$ , and  $\text{RhCl}(\text{PPh}_3)_3$ . While  $\text{Sn}_9\text{Rh}(\text{cod})^{3-}$ ,  $\text{Rh@Sn}_{12}^{3-}$ , and  $\text{Rh@Pb}_{12}^{3-}$  were eventually isolated from the reaction of  $E_9^{4-}$  and  $[\text{Rh}(\text{cod})\text{Cl}]_2$  or  $\text{RhCl}(\text{PPh}_3)_3$  (see Chapters 2 and 3); early experiments first resulted in the isolation of the new  $[\text{Rh}_2\text{H}(\text{PPh}_2)_2(\text{PPh}_3)_3]^-$  complex with the use of Wilkinson’s catalyst in ethylenediamine (en) solution. Likewise, the reaction of  $\text{Sn}_9^{4-}$  with  $\text{Co}_4(\text{CO})_{12}$  afforded the previously unknown  $\text{Co}_3(\text{CO})_7^{3-}$  as the only detectable product, and

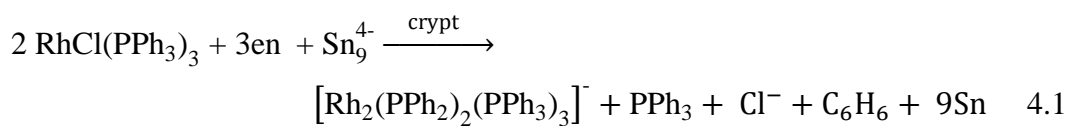
the reaction of  $\text{As}_7^{3-}$  and  $\text{Ir}_4(\text{CO})_{12}$  readily produced the  $[(\text{C}_3\text{H}_7\text{N}_2\text{O})_3\text{Ir}_4(\text{CO})_9]^{3-}$  carbamoyl. These reactions are highly reproducible and highlight that the  $\text{Sn}_9^{4-}$  and  $\text{As}_7^{3-}$  Zintl clusters are strong, soluble reducing agents.

The synthesis of these anionic complexes exploits the reducing properties of Zintl clusters, namely  $\text{Sn}_9^{4-}$  and  $\text{As}_7^{3-}$ . Although the Zintl ions are generally utilized as electrophiles, these cluster anions may react to reduce phosphines, amines, and cobalt under specific conditions. The synthesis and crystallographic characterization of the novel  $[\text{Rh}_2\text{H}(\text{PPh}_2)_2(\text{PPh}_3)_3]^-$ ,  $\text{Co}_3(\text{CO})_7^{3-}$ , and  $[(\text{C}_3\text{H}_7\text{N}_2\text{O})_3\text{Ir}_4(\text{CO})_9]^{3-}$  ions are detailed below.

## 4.2. Results and Discussion

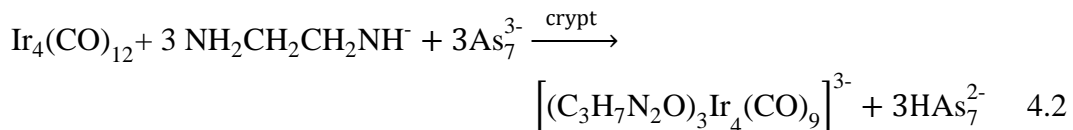
### 4.2.1. Synthesis

**$[\text{Rh}_2\text{H}(\text{PPh}_2)_2(\text{PPh}_3)_3]^-$  (4.1):** Ethylenediamine (en) solutions of  $\text{K}_4\text{Sn}_9$  and  $\text{K}_4\text{Pb}_9$  react with toluene (tol) solutions of  $\text{RhCl}(\text{PPh}_3)_3$  in the presence of 2,2,2-crypt to give the  $[\text{Rh}_2\text{H}(\text{PPh}_2)_2(\text{PPh}_3)_3]^-$  ion. The  $[\text{K}(2,2,2\text{-crypt})]^+$  salt is isolated in *ca.* 30% yield. The cluster is air and moisture sensitive in solution and in the solid state. The salts are soluble in pyridine and DMF and have been characterized by single-crystal X-ray diffraction, and various  $^1\text{H}$  and  $^{31}\text{P}$  NMR experiments. With additional 2,2,2-crypt and  $\text{K}^+$  in the original reaction mixture, the  $\text{Rh}@\text{Sn}_{10}^{3-}$  ion eventually forms as discussed in the Appendix.



**[Co<sub>3</sub>(CO)<sub>7</sub>]<sup>3-</sup> (4.2):** En solutions of K<sub>4</sub>Sn<sub>9</sub> react with en/tol solutions of Co<sub>4</sub>(CO)<sub>12</sub> in the presence of 2,2,2-crypt to give [Co<sub>3</sub>(CO)<sub>7</sub>]<sup>3-</sup>. The [K(2,2,2-crypt)]<sup>+</sup> salt is soluble in DMF and has been characterized by single-crystal X-ray diffraction.

**[(C<sub>3</sub>H<sub>7</sub>N<sub>2</sub>O)<sub>3</sub>Ir<sub>4</sub>(CO)<sub>9</sub>]<sup>3-</sup> (4.3):** En solutions of Na<sub>3</sub>As<sub>7</sub> react with tol solutions of Ir<sub>4</sub>(CO)<sub>12</sub> in the presence of 2,2,2-crypt to give the iridium-carbamoyl. The [Na(2,2,2-crypt)]<sup>+</sup> salt is isolated in *ca.* 72% yield. The cluster is air and moisture sensitive in solution and in the solid state. The salt is soluble in DMF and has been characterized by single-crystal X-ray diffraction.



#### 4.2.2. Solid State Structure

The [K(2,2,2-crypt)][Rh<sub>2</sub>H(PPh<sub>2</sub>)<sub>2</sub>(PPh<sub>3</sub>)<sub>3</sub>] crystal is triclinic, space group P $\bar{1}$ . A summary of the crystallographic data and selected bond distances and angles are given in Table 4.1 and Table 4.2, respectively. The crystal structure of the complex is shown in Figure 4.1.

**Table 4.1.** Crystallographic data for the  $[\text{Rh}_2\text{H}(\text{PPh}_2)_2(\text{PPh}_3)_3]^-$  ion.

Compound	$[\text{K}(2,2,2\text{-crypt})][\text{Rh}_2\text{H}(\text{PPh}_2)_2(\text{PPh}_3)_3]\cdot\text{tol}$
formula weight	1870.69
temperature (K)	150(2)
Wavelength ( $\text{\AA}$ )	0.71073
crystal system	triclinic
space group	P-1
unit cell dimensions	
a ( $\text{\AA}$ )	14.6047(12) $\text{\AA}$
b ( $\text{\AA}$ )	16.4872(14) $\text{\AA}$
c ( $\text{\AA}$ )	19.4784(16) $\text{\AA}$
$\alpha$ ( $^\circ$ )	89.8857(14) $^\circ$
$\beta$ ( $^\circ$ )	75.5620(13) $^\circ$
$\gamma$ ( $^\circ$ )	86.6712(13) $^\circ$
volume ( $\text{\AA}^3$ )	4534.0(7)
Z	2
$D_{\text{calc}}$ ( $\text{g/cm}^3$ )	1.370
abs. coeff. ( $\text{mm}^{-1}$ )	0.554
final R indices: $R_1$ , <sup>a</sup> $I > 2\sigma(I)$	0.0422
$wR_2$ , <sup>a</sup> all data	0.0891

$$^a R_1 = \frac{\sum ||F_o| - |F_c||}{\sum |F_o|}, \quad wR_2 = \left[ \frac{\sum w(F_o^2 - F_c^2)^2}{\sum w(F_o^2)^2} \right]^{1/2}$$

The structure of the anion contains two rhodium atoms with different ligands and coordinate geometries, giving the structure  $C_s$  point symmetry. The core of the structure includes two rhodium atoms bridged by two diphenylphosphido groups. The ion is a 32-electron complex (each Rh = 9 e-, each  $\text{PPh}_2$  = 3 e-, each  $\text{PPh}_3$  = 2 e-, H = 1 e-, charge = 1 e-). Formally, the complex has a  $\text{Rh}_2^{2+}$  core and can be viewed as a Rh(I)-Rh(I) dimer. The rhodium atoms are separated by 2.7533(4)  $\text{\AA}$ , which is consistent with the presence of a Rh-Rh single bond.<sup>139-141</sup>

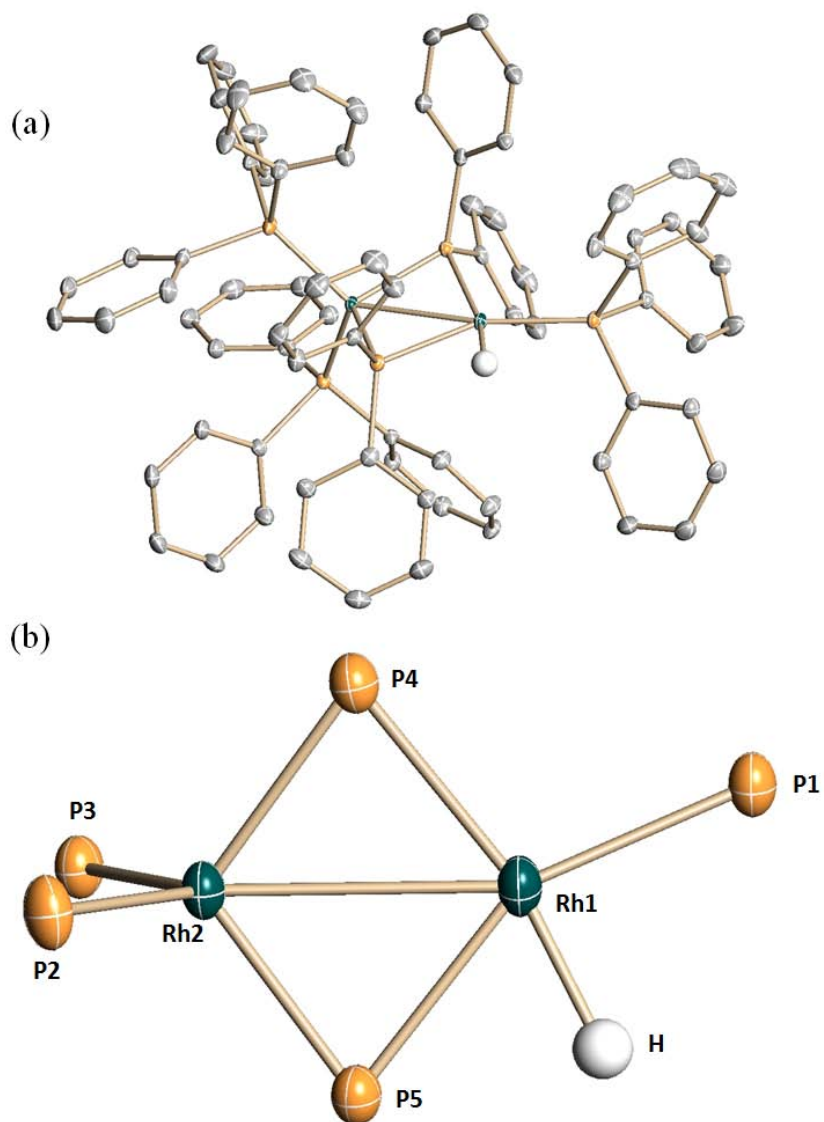


**Figure 4.1.** Crystal structure of (a)  $[\text{Rh}_2\text{H}(\text{PPh}_2)_2(\text{PPh}_3)_3]^-$  and (b) the dirhodium core omitting the phenyl groups for clarity. Thermal ellipsoids are drawn at the 50% probability level.

**Table 4.2.** Selected Bond Lengths (Å) and Angles (°) for [Rh<sub>2</sub>H(PPh<sub>2</sub>)<sub>2</sub>(PPh<sub>3</sub>)<sub>3</sub>].

Rh(1)–Rh(2)	2.7533(4)	Rh(2)–P(2)	2.2641(10)
Rh(1)–P(1)	2.2298(10)	Rh(2)–P(3)	2.2931(10)
Rh(1)–P(4)	2.3213(10)	Rh(2)–P(4)	2.2419(10)
Rh(1)–P(5)	2.3040(10)	Rh(2)–P(5)	2.2231(10)
Rh(1)–H(1)	1.59(4)		
P(1)–Rh(1)–H(1)	86.5(1)	P(5)–Rh(2)–P(4)	107.53(4)
P(1)–Rh(1)–P(5)	150.87(4)	Rh(2)–P(4)–Rh(1)	74.20(3)
P(5)–Rh(2)–Rh(1)	53.89(3)	P(2)–Rh(2)–Rh(1)	130.54(3)
P(5)–Rh(1)–H(1)	65.1(14)	P(5)–Rh(2)–P(2)	109.65(4)
P(4)–Rh(1)–Rh(2)	51.58(2)	Rh(2)–P(5)–Rh(1)	74.89(3)
P(4)–Rh(2)–P(2)	108.74(4)	P(2)–Rh(2)–P(3)	115.42(4)
P(4)–Rh(1)–H(1)	163.9(14)	P(5)–Rh(2)–P(3)	107.36(4)
P(5)–Rh(1)–Rh(2)	51.22(3)	P(1)–Rh(1)–Rh(2)	156.83(3)
P(4)–Rh(2)–P(3)	107.87(4)	P(3)–Rh(2)–Rh(1)	114.04(3)
Rh(2)–Rh(1)–H(1)	116.2(14)	P(1)–Rh(1)–P(4)	106.81(4)
P(5)–Rh(1)–P(4)	102.27(4)	P(4)–Rh(2)–Rh(1)	54.22(3)

Rh(1) is in a square planar environment with two phosphido ligands, a hydride, and a terminal phosphine. The hydride ligand is trans to one of the bridging phosphido ligands and was located crystallographically. The phosphorus atoms around Rh(1) are arranged in a planar arrangement with the sum of the P–Rh–P angles about the rhodium atom of 359.9°. Rh(2) is in a pseudo-tetrahedral geometry. The distorted tetrahedron has P–Rh(2)–P bond angles ranging from 107.36(4)°–115.42(4)°. In addition to geometry, there are also differences in bond lengths observed around Rh(1) and Rh(2). The rhodium-phosphido bonds about Rh(1) have an average bond length of 2.31(1) Å while the two involving Rh(2) are somewhat shorter at 2.23(1) Å. Of the two longer Rh(1)-phosphido bonds, the longest is the Rh–P bond trans to the hydride ligand, as expected due to the high trans influence of hydrides.<sup>142</sup> The rhodium-phosphine bonds to Rh(2) average

2.28(2) Å while the Rh(1)-P(1) bond is 2.230 (1) Å. All of these bonds fall within the range of other Rh(I)-phosphine bonds (see Table 4.3).

**Table 4.3.** Bond lengths (Å) and oxidation states of various rhodium complexes.

Rhodium Dimer	Oxidation State	Average Rh-PR <sub>3</sub>	Rh-Rh
Rh <sub>2</sub> H(PPh <sub>2</sub> ) <sub>2</sub> (PPh <sub>3</sub> ) <sub>3</sub>	Rh <sub>2</sub> (I,I)	2.28, 2.23	2.75
Rh <sub>2</sub> (PPh <sub>2</sub> ) <sub>2</sub> (cod)(PEt <sub>3</sub> ) <sub>2</sub> <sup>[139]</sup>	Rh <sub>2</sub> (I,I)	2.32	2.75
Rh(C <sub>7</sub> H <sub>3</sub> Cl <sub>2</sub> O <sub>2</sub> )(C <sub>18</sub> H <sub>15</sub> P)(CO) <sup>[143]</sup>	Rh(I)	2.24	---
[RhCl(η <sup>4</sup> -cod)-(P(2-CH <sub>3</sub> C <sub>6</sub> H <sub>4</sub> ) <sub>3</sub> )] <sup>[144]</sup>	Rh(I)	2.36	---
Rh <sub>2</sub> (OAc) <sub>4</sub> (PPh <sub>3</sub> ) <sub>2</sub> <sup>[145]</sup>	Rh <sub>2</sub> (II,II)	2.47	2.45
[Rh(CO)(PPh <sub>3</sub> )Tp'] <sup>[146]</sup>	Rh(I)	2.27	---
[Rh(CO)(PPh <sub>3</sub> )Tp'] <sup>+</sup> <sup>[146]</sup>	Rh(II)	2.33	---

Tp' = HB(3,5-dimethylpyrazolyl)<sub>3</sub>

There are several known diphenylphosphido-bridged rhodium dimers including [(Et<sub>3</sub>P)<sub>2</sub>Rh(PPh<sub>2</sub>)Rh(cod)], [(PPh<sub>3</sub>)<sub>2</sub>Rh(PPh<sub>2</sub>)Rh(cod)], [Rh<sub>2</sub>(μ-Cl)(μ-PPh<sub>2</sub>)(cod)<sub>2</sub>], and [Rh<sub>2</sub>(μ-Cl)(μ-PMePh)(cod)<sub>2</sub>].<sup>139,147,148</sup> These complexes all possess Rh(I) oxidation states with Rh-Rh single bonds. Rhodium dimer **4.1** differs from the other dimers in that it is an unsymmetrical complex containing two metal centers with a pseudo-tetrahedral and square planar geometries, a hydride ligand at the square planar site, and a Rh-Rh single bond.

The [K(2,2,2-crypt)]<sub>3</sub>[Co<sub>3</sub>(CO)<sub>7</sub>]·solvent crystal is monoclinic, space group P2<sub>1</sub>/c. Crystallographic data and selected bond distances and angles are summarized in Table 4.4 and Table 4.5, respectively. The crystal structure of the complex is shown in three orientations in Figure 4.2.



**Table 4.4.** Crystallographic data for the  $[\text{Co}_3(\text{CO})_7]^{3-}$  ion.

Compound	$[\text{K}(2,2,2\text{-crypt})]_3[\text{Co}_3(\text{CO})_7]\cdot\text{solvent}$
temperature (K)	150(2)
Wavelength ( $\text{\AA}$ )	0.71073
crystal system	monoclinic
space group	$P2_1/c$
unit cell dimensions	
a ( $\text{\AA}$ )	23.307(3)
b ( $\text{\AA}$ )	15.417(2)
c ( $\text{\AA}$ )	23.102(3)
$\alpha$ ( $^\circ$ )	90
$\beta$ ( $^\circ$ )	103.318(4)
$\gamma$ ( $^\circ$ )	90
volume ( $\text{\AA}^3$ )	8077.75

The  $[\text{Co}_3(\text{CO})_7]^{3-}$  cluster possesses distorted  $C_{3v}$  point symmetry and seven carbonyl groups bonded in three distinct ways. The structure is comprised of three cobalt atoms with pseudo-tetrahedral coordination, each of which is bonded to a terminal carbonyl ligand. Three  $\mu^2$ -carbonyls are bonded to the core of the cluster around the periphery of the cluster, while the  $\mu^3$ -carbonyl ligand is bonded to each cobalt atom. The heptacarbonyl cluster is a 44-electron complex (each Co = 9  $e^-$ , each CO = 2  $e^-$ , charge = 3  $e^-$ ). The formal oxidation state of cobalt can be described as Co(-1) due to the 3- charge of the tricobalt complex. The Co-Co interactions therefore likely have a bond order of  $1\frac{2}{3}$ , with a mean Co-Co bond distance of 2.356  $\text{\AA}$ .

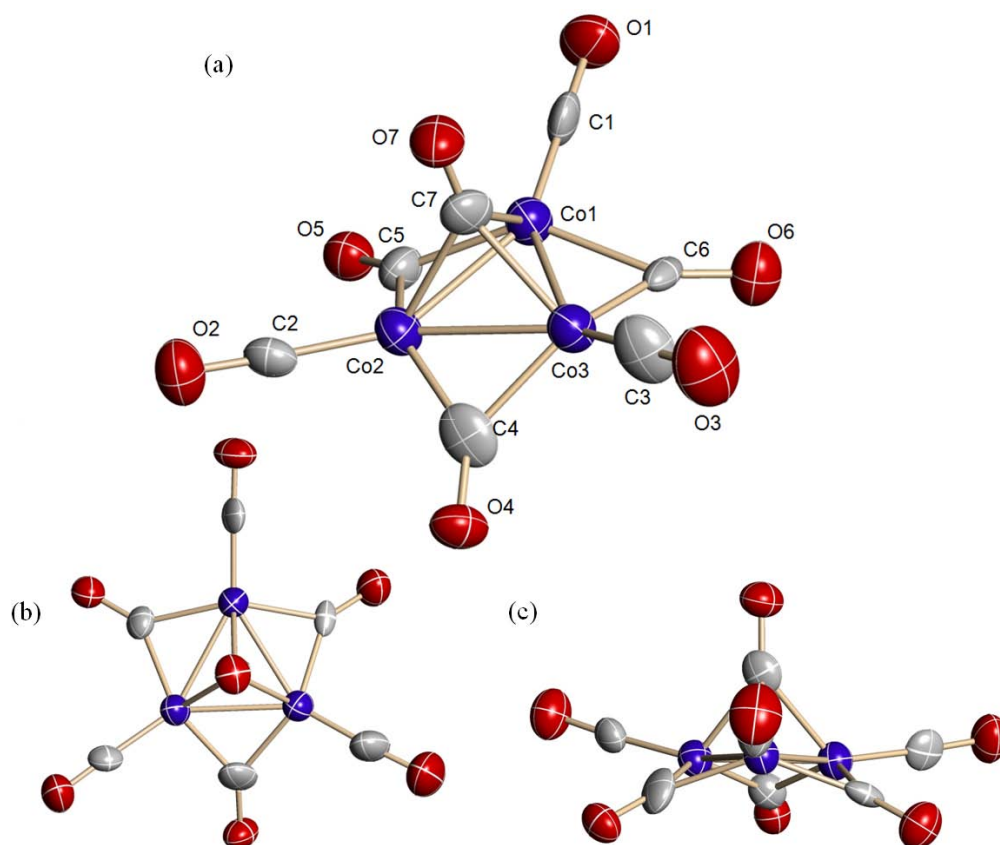


**Figure 4.2.** Crystal structure of the  $[\text{Co}_3(\text{CO})_7]^{3-}$  carbonyl cluster (blue = Co, red = O, gray = C). The  $C_{3v}$  symmetry is highlighted by views of the cluster (b) down the  $C_3$  axis and (c) perpendicular to the  $C_3$  axis. Thermal ellipsoids are drawn at the 50% probability level.

**Table 4.5.** Selected Bond Lengths (Å) and Angles ( $^\circ$ ) for  $[\text{Co}_3(\text{CO})_7]^{3-}$ .<sup>a</sup>

Co(1)–Co(2)	2.3548(2)	Co(2)–C(2)	1.6863(1)
Co(1)–Co(3)	2.3498(2)	Co(2)–C(4)	1.8515(2)
Co(2)–Co(3)	2.3631(2)	Co(3)–C(3)	1.6256(1)
Co(1)–C(1)	1.6822(2)	Co(3)–C(4)	1.8795(2)
Co(1)–C(5)	1.8870(2)	C(1)–O(1)	1.2174(1)
Co(1)–C(6)	1.8955(2)	C(4)–O(4)	1.2293(1)
Co(1)–C(7)	2.0235(2)	C(7)–O(7)	1.2221(1)
Co(3)–Co(1)–Co(2)	60.30	Co(1)–C(5)–Co(2)	77.49
Co(1)–Co(2)–Co(3)	59.74	Co(1)–C(5)–O(5)	138.91
Co(2)–Co(3)–Co(1)	59.95	Co(1)–C(7)–Co(2)	72.41
Co(1)–C(1)–O(1)	177.14	Co(1)–C(7)–O(7)	136.02

<sup>a</sup> Preliminary data. Refinement in progress.

The cobalt atoms form a regular triangle with the Co-Co-Co angles in the precise range of  $60.0^\circ \pm 0.3^\circ$ . Each Co is in a distorted tetrahedral environment with average C-Co-C angles of  $104.1^\circ$ ; the largest disorder is associated with the bond angles involving the face-capping carbonyl, ranging from  $98.4^\circ$  to  $119.7^\circ$ . The terminal ligands possess the shortest Co-C bonds with a  $1.665 \text{ \AA}$  mean distance while the longest Co-C bonds are those of the face-capping  $\mu^3$ -carbonyls with a mean distance of  $1.989 \text{ \AA}$ . The terminal CO ligands lie above the plane of the cobalt atoms, with a torsion angle of  $23.1^\circ \pm 6.4^\circ$  with respect to the cobalt plane. The edge-bridging carbonyl Co-C bonds have an average bond length of  $1.877 \text{ \AA}$  (ave). These  $\mu^2$ -carbonyl ligands are positioned slightly closer to the plane of cobalt atoms with a torsion angle of  $\phi(\text{Co}(1)\text{-Co}(2)\text{-Co}(3)\text{-C}_{\mu 2}) = 18.7^\circ \pm 3.1^\circ$ , angled below the  $\text{Co}_3$  plane (Figure 4.3c).

The Co-Co bonds are short in length compared to other known cobalt carbonyl complexes.<sup>149-152</sup> The Co-Co bonds in the  $\text{Co}_4(\text{CO})_{12}$  precursor have a mean distance of  $2.490 \text{ \AA}$  and the terminal and edge-bridging carbonyls have mean Co-C bond lengths of  $1.798 \text{ \AA}$  and  $1.963 \text{ \AA}$ , respectively.<sup>149</sup> The discrepancies in bond lengths between  $\text{Co}_3(\text{CO})_7^{3-}$  and the  $\text{Co}(0)$  cluster may be attributed to a higher bond order in the bonds of the electron rich cobalt(-I) cluster. The electron rich cluster has stronger Co-C bonds due to formal  $\pi$  back bonding interactions between the Co d-orbitals and the C=O  $\pi^*$  anti-bonding orbitals. This interaction also effectively weakens the C=O bonds of the carbonyl ligands, as the C-O bonds show an increase in bond length from  $1.13 \text{ \AA}$  to  $1.23 \text{ \AA}$  (Table 4.6).

Though rare, cobalt-cobalt double bonds have been reported in the literature.<sup>153-155</sup> In 1983 Geoffrey and coworkers reported the synthesis and characterization of  $\text{Co}_2(\mu\text{-PPh}_2)_2(\text{CO})_2(\text{PEt}_2\text{Ph})_2$ .<sup>153</sup> The phosphido-carbonyl complex has a Co-Co bond distance of 2.343(2) Å. The short bond distance and an achievable 18-electron count via a double bond formation make the double bond a reasonable bond-order assignment for the 32 e- complex. The average Co-Co bond distance of the  $\text{Co}_3(\text{CO})_7^{3-}$  ion is only 0.013 Å longer than that of  $\text{Co}_2(\mu\text{-PPh}_2)_2(\text{CO})_2(\text{PEt}_2\text{Ph})_2$ , making it more similar in length to the cobalt dimer than to the  $\text{Co}_4(\text{CO})_{12}$  precursor. This similarity is consistent with a bond order of  $1\frac{2}{3}$ , predicted using the electron count.

**Table 4.6.** Bond lengths (Å) of  $\text{Co}_3(\text{CO})_7^{3-}$  & additional cobalt carbonyl complexes.

Complex	Oxidation	Bond Order	Co-Co	Co-C			C-O
				$\mu^1$	$\mu^2$	$\mu^3$	
$\text{Co}_3(\text{CO})_7^{3-}$	-1	$1\frac{2}{3}$	2.356	1.665	1.877	1.989	1.21-1.23
Cobalt-carbonyls <sup>a</sup> [152]	---	---	---	1.780	1.914	1.950	1.15-1.19
$\text{Co}_2(\mu\text{-PPh}_2)_2(\text{CO})_2(\text{PEt}_2\text{Ph})_2$ [153]	-1	2	2.343	1.731	---	---	1.148 <sup>b</sup>
$\text{Co}_4(\text{CO})_{12}$ [149]	0	1	2.490	1.789	1.963	---	1.13 <sup>b</sup>
$\text{Co}_4(\text{CO})_{11}^{2-}$ [150]	- $\frac{1}{2}$	1	2.494	1.756	1.945	1.985	1.14-1.19
$\text{Co}_6(\text{CO})_{15}^{2-}$ [151]	- $\frac{1}{3}$	1	2.49	1.74	1.90	2.00	1.15-1.19
$\text{Co}(\text{CO})_4^{-}$ [156]	-1	---	---	1.779	---	---	1.15-1.16
$[\text{Co}_3(\text{CO})_7\text{Se}]_2\text{Se}_2$ [157]	+ $\frac{4}{3}$	1	2.551	1.777	---	---	1.10-1.20

<sup>a</sup> Table of X-ray data from known carbonyl complexes

<sup>b</sup> Only a mean C-O bond reported

Like  $\text{Co}_3(\text{CO})_7^{3-}$ ,  $\text{Co}_4(\text{CO})_{11}^{2-}$  and other cobalate clusters have face-capping  $\mu^3$ -carbonyls, which is a normal occurrence in negatively charged clusters.<sup>150,151</sup> The  $\text{Co}_3(\text{CO})_7^{3-}$  terminal and  $\mu^2$  Co-C bond lengths are on the shorter end of the range of the average bonds of known cobalt-carbonyls while  $\mu^3$  is slightly longer (1.780 Å, 1.914 Å, and 1.950 Å respectively).<sup>152</sup> There is a

considerable increase in C-O bond lengths across each carbonyl group due to back-bonding from Co(-1). It is important to note that  $[(\mu_3\text{-Se})\text{Co}_3(\text{CO})_7]_2\mu_4\text{-}(\text{Se}_2)$  was reported in 1995 but there are little structural similarities between the two structures.<sup>157</sup> The two  $\text{Co}_3$  moieties of the selenide are capped to give two  $\text{Co}_3\text{Se}$  pyramids linked by a diselenide linker, in which each carbonyl is terminal in nature. The two complexes also possess very different oxidation states and bond orders as summarized in Table 4.6.

The  $[\text{Na}(2,2,2\text{-crypt})]_3[(\text{C}_3\text{H}_7\text{N}_2\text{O})_3\text{Ir}_4(\text{CO})_9]\cdot\text{en}$  crystal is triclinic, space group P-1. The crystallographic data is summarized in Table 4.7 and selected bond distances and angles are tabulated in Table 4.8, respectively. The crystal structure of the complex is illustrated in Figure 4.3.

**Table 4.7.** Crystallographic data for the  $[(\text{C}_3\text{H}_7\text{N}_2\text{O})_3\text{Ir}_4(\text{CO})_9]^{3-}$  ion.

Compound	$[\text{Na}(2,2,2\text{-crypt})]_3[(\text{C}_3\text{H}_7\text{N}_2\text{O})_3\text{Ir}_4(\text{CO})_9]\cdot\text{en}$
formula weight	2540.75
temperature (K)	220(2)
Wavelength (Å)	0.71073
crystal system	triclinic
space group	P-1
unit cell dimensions	
a (Å)	15.115(2)
b (Å)	15.781(2)
c (Å)	22.153(3)
$\alpha$ (°)	79.999(2)
$\beta$ (°)	83.817(3)
$\gamma$ (°)	66.589(2)
volume (Å <sup>3</sup> )	4771.1(13)
Z	2
$D_{\text{calc}}$ (g/cm <sup>3</sup> )	1.769
abs. coeff. (mm <sup>-1</sup> )	5.656
final R indices: $R_1$ , <sup>a</sup> $I > 2\sigma(I)$	0.0290
$wR_2$ , <sup>a</sup> all data	0.0695

<sup>a</sup>  $R_1 = \sum ||F_o| - |F_c|| / \sum |F_o|$ ,  $wR_2 = [\sum w(F_o^2 - F_c^2)^2 / \sum w(F_o^2)^2]^{1/2}$

The  $[(C_3H_7N_2O)_3Ir_4(CO)_9]^{3-}$  ion has virtual  $C_{3v}$  point symmetry and possesses six terminal carbonyl groups, three edge-bridging carbonyls, and three  $-C(O)NH(CH_2)_2NH_3$  carbamoyl ligands. The iridium atoms are arranged in an elongated tetrahedron, similar to the  $Ir_4(CO)_{12}$  precursor, and the carbamoyl ligands are bonded to the three basal iridium atoms (Figure 4.3). The cluster is a  $60 e^-$  cluster (each Ir =  $9 e^-$ , each CO =  $2 e^-$ , each CO-en =  $1 e^-$ , charge =  $3 e^-$ ), giving singly bonded singly bonded Ir(0) centers. The tetrairidium cluster is 12 e- short of the 72 e- count possible for 18 e- metal centers, leaving the possibility of 6 Ir-Ir bonds which is observed in the tetrairidium cluster with six edges.

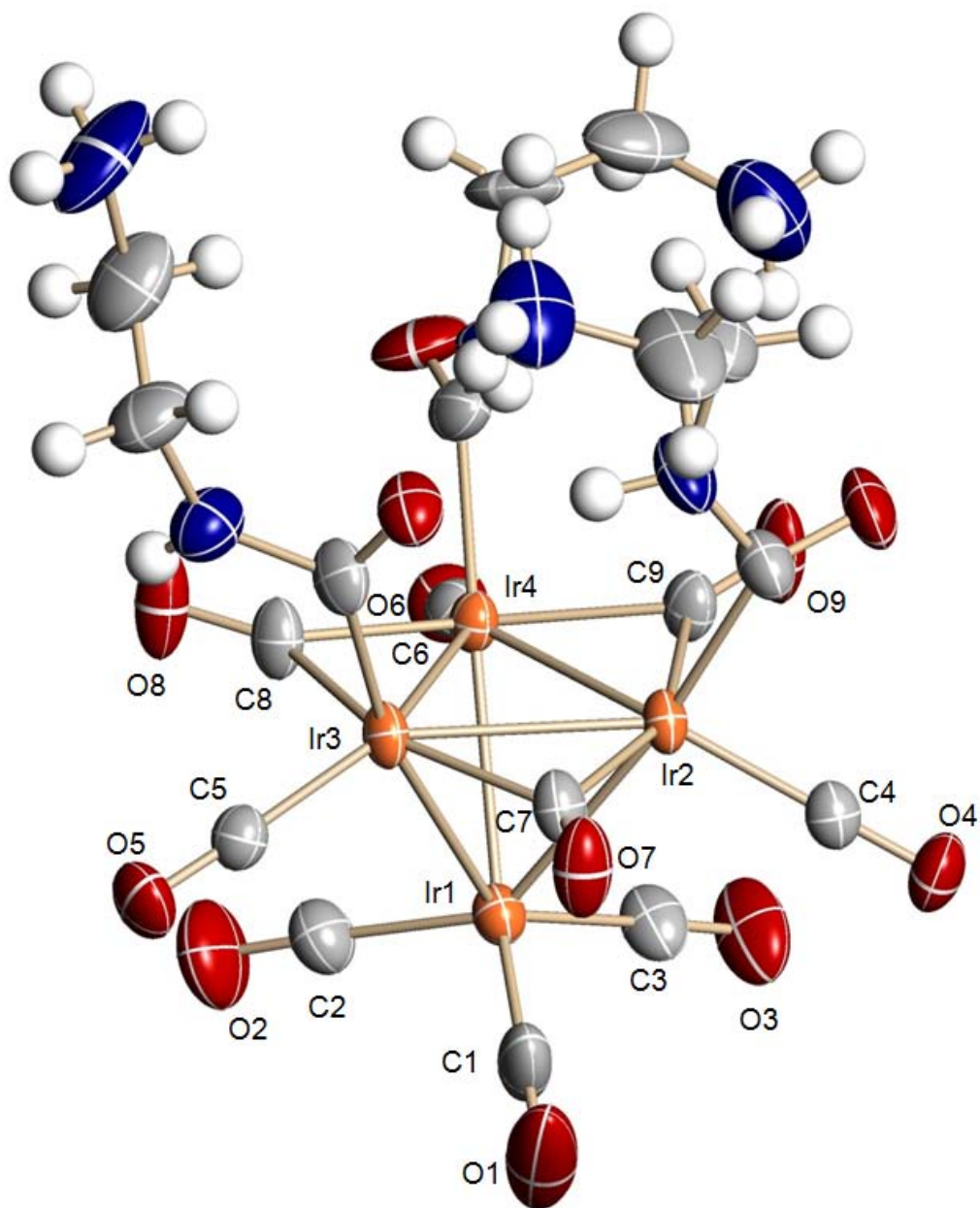


**Figure 4.3.** Crystal structure of the  $[(C_3H_7N_2O)_3Ir_4(CO)_9]^{3-}$  carbamoyl cluster. Thermal ellipsoids are drawn at the 50% probability level.

**Table 4.8.** Selected Bond Lengths (Å) and Angles (°) of  $[(C_3H_7N_2O)_3Ir_4(CO)_9]^{3-}$ .

Ir(1)–Ir(2)	2.8366(5)	Ir(2)–C(22)	2.075(4)
Ir(1)–Ir(3)	2.8470(4)	C(1)–O(1)	1.163(6)
Ir(1)–Ir(4)	2.8378(4)	C(4)–O(4)	1.141(5)
Ir(2)–Ir(3)	2.7365(4)	C(7)–O(7)	1.173(5)
Ir(2)–Ir(4)	2.7472(4)	C(22)–O(21)	1.243(5)
Ir(3)–Ir(4)	2.7248(4)	C(22)–N(23)	1.353(6)
Ir(1)–C(1)	1.866(5)	C(24)–N(23)	1.452(6)
Ir(2)–C(4)	1.846(4)	C(25)–N(26)	1.450(9)
Ir(2)–C(9)	2.081(4)	C(24)–C(25)	1.472(8)
<hr/>			
Ir(2)–Ir(1)–Ir(3)	57.562(10)	Ir(1)–C(1)–O(1)	177.6(6)
Ir(1)–Ir(2)–Ir(3)	61.409(6)	Ir(2)–C(4)–O(4)	176.6(4)
Ir(3)–Ir(2)–Ir(4)	59.589(8)	Ir(2)–C(7)–O(7)	140.0(3)
Ir(2)–C(7)–Ir(3)	81.56(15)	N(23)–C(22)–O(21)	116.4(5)

The  $Ir_4$  core forms a distorted tetrahedron, creating two distinct environments. The apical iridium atom is bonded to the remaining three iridium atoms with a mean bond length of 2.841 Å, while the basal atoms have a shorter mean Ir-Ir bond length of 2.736 Å. The apical Ir(1) has three terminal carbonyls with a mean Ir(1)-C bond of 1.874 Å. The basal iridium atoms are bonded by a terminal carbonyl each and are all connected by edge-bridging carbonyl ligands in addition to the CO-en carbamoyl ligated to each. The terminal carbonyls of the basal metals have a mean 1.841 Å Ir-C bond and the  $\mu^2$ -carbonyls have 2.069 Å bond lengths. The carbamoyl ligands are bonded to the iridium centers with a mean Ir-C bond length of 2.063 Å, much longer than the Ir-C bonds of the terminal carbonyls. The basal terminal C-O bonds are shorter than those of Ir(1), possessing a mean average length of 1.151 Å and 1.160 Å respectively. The  $\mu^2$ -carbonyls and carbamoyls have a mean C-O bond length of 1.175 Å and 1.247 Å the  $\mu^2$ -carbonyls have 2.069 Å respectively. The carbamoyl C-O bond length is consistent with the 1.25(1) Å carbamoyl bond of the  $[Ir_2(\mu-CO)(\mu-$



$\text{H})(\text{C}(\text{O})\text{NHR})_2(\text{CNR})_2(\text{Me}_2\text{PCH}_2\text{PMe}_2)_2]^+$  cation, an iridium-carbamoyl complex where  $\text{R} = 2,6\text{-Me}_2\text{C}_6\text{H}_3$ .<sup>158</sup>

It is unknown how the  $[(\text{C}_3\text{H}_7\text{N}_2\text{O})_3\text{Ir}_4(\text{CO})_9]^{3-}$  cluster is formed, but there are two likely synthetic pathways: 1) CO insertion into the Ir-N bond of a coordinated amide or 2) the nucleophilic addition of the  $\text{NH}_2\text{CH}_2\text{CH}_2\text{NH}^-$  amide anion to three carbonyls of the cluster. The most commonly evoked mechanism of carbamoyl synthesis in the literature is the migratory insertion of a coordinated carbon monoxide ligand into a metal-amide bond, but the nucleophilic addition of amides to afford carbamoyl ligands has also been considered.<sup>159</sup> In the case of the Zintl cluster route described herein, it is plausible that the iridium carbamoyl is synthesized via the nucleophilic addition of amide anions to the carbonyl ligands of  $\text{Ir}_4(\text{CO})_{12}$ . It has been well established that  $\text{Sn}_9^{4-}$  dissolves in en to give the  $\text{HSn}_9^{3-}$  ion via the deprotonation of en.<sup>73</sup> Additionally, the  $\text{HP}_7^{2-}$  ion has been isolated in the solid state which also supports the probability of the equilibrium occurring in an en solution of the  $\text{As}_7^{3-}$  anion.<sup>160</sup>

#### 4.2.3. NMR Spectroscopic Studies

The  $^{31}\text{P}\{^1\text{H}\}$  NMR spectrum of the rhodium dimer includes three phosphorus signals with chemical shifts of  $\delta = 23.5$  ppm, 29.6 ppm, and 197.9 ppm as shown in Figure 4.4. The three signals have relative intensities of 1:2:2, which is consistent with the number of phosphorus atoms in the complex. However, four signals are expected from the  $\text{A}_2\text{MNX}$  phosphorus spin system based on the solid state structure. The unexpected splitting patterns in the

spectrum suggest that the complex is dynamic in solution, generating an  $A_2M_2X$  phosphorus spin system.

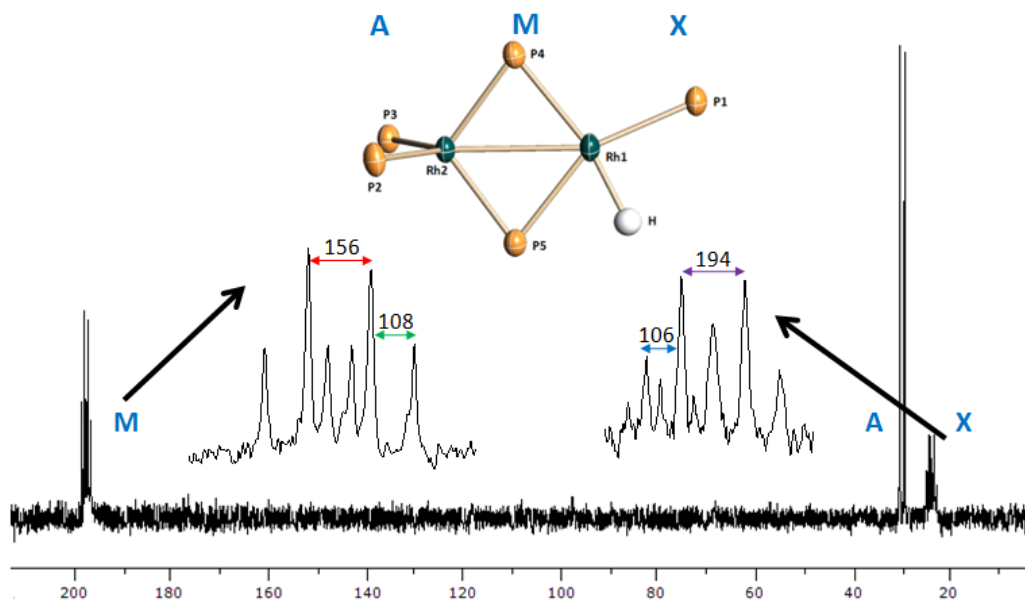


**Figure 4.4.**  $^{31}\text{P}\{^1\text{H}\}$  NMR spectrum for the  $[\text{Rh}_2\text{H}(\text{PPh}_2)_2(\text{PPh}_3)_3]^-$  ion. Data were recorded at 298 K at 202.46 MHz in Pyr.  $\delta = 23.5$  ppm ( $^1J(^{31}\text{P}, ^{103}\text{Rh}) = 194$  Hz,  $^2J(^{31}\text{P}, ^{31}\text{P}) = 106$  Hz), 29.6 ppm ( $^1J(^{31}\text{P}, ^{103}\text{Rh}) = 208$  Hz), and 197.9 ppm ( $^1J(^{31}\text{P}, ^{103}\text{Rh}) = 156$  Hz,  $^1J(^{31}\text{P}, ^{103}\text{Rh}) = 110$  Hz,  $^2J(^{31}\text{P}, ^{31}\text{P}) = 106$  Hz).

The exchange process is clearly intramolecular since all of the ligands maintain coupling to  $^{103}\text{Rh}$  in the room temperature spectrum. A doublet is observed for the equivalent  $\text{PPh}_3$  ligands, **A**, with a chemical shift of  $\delta = 29.6$  ppm ( $^1J(^{31}\text{P}_M, ^{103}\text{Rh}) = 208$  Hz), while the other two signals are more complex. The  $\text{PPh}_3$  signal at 23.5 ppm, **X**, appears to be a doublet of triplets with  $^1J(^{31}\text{P}_X, ^{103}\text{Rh})$  and  $^2J(^{31}\text{P}_X, ^{31}\text{P}_M)$  coupling constants of 194 Hz and 106 Hz respectively. The two  $\text{PPh}_2$  phosphido ligands give rise to a single resonance at 198 ppm. The resonance appears to be a virtual triplet with 108 coupling that presumably arises from an actual doublet of doublets with coupling constants of  $^2J(^{31}\text{P}_M, ^{31}\text{P}_X) = 106$

Hz and  $^1J(^{31}\text{P}_M-^{103}\text{Rh}) = 110$  Hz. A  $^{31}\text{P}$ - $^{31}\text{P}$  COSY experiment (Figure 4.5) shows a correlation between  $\text{P}_A$  and  $\text{P}_M$ . Couplings to other phosphorus nuclei were not detected. The observed  $^1J(^{31}\text{P}-^{103}\text{Rh})$  values for phosphine resonances **A** and **X** are within the 190-231 Hz range observed for the closely related rhodium-phosphine complexes  $[(\text{PR}_3)_2\text{Rh}(\text{PPh}_2)\text{Rh}(\text{cod})]$  where  $\text{R}_3 = \text{Et}_3, \text{Cy}_3, \text{MePh}_2, \text{Ph}_3$ ). Rh-P coupling constants for the  $\mu\text{-PPh}_2$  ligands in these compounds fall in the range 87 – 202 Hz, which is also consistent with the observed data for  $[\text{Rh}_2\text{H}(\text{PPh}_2)_2(\text{PPh}_3)_3]^-$ .

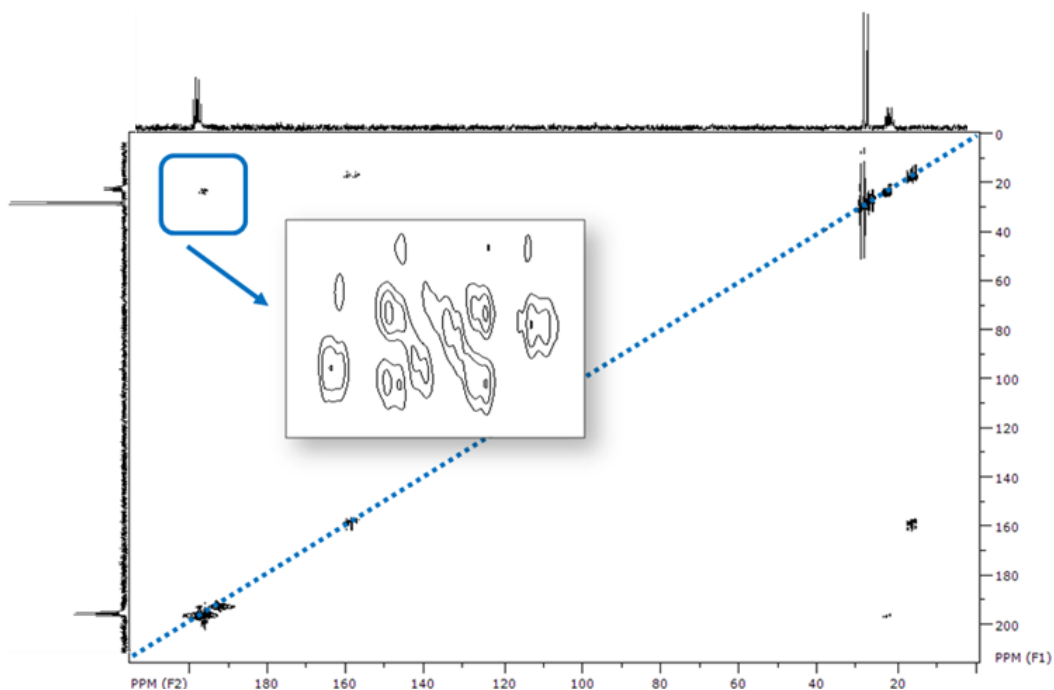
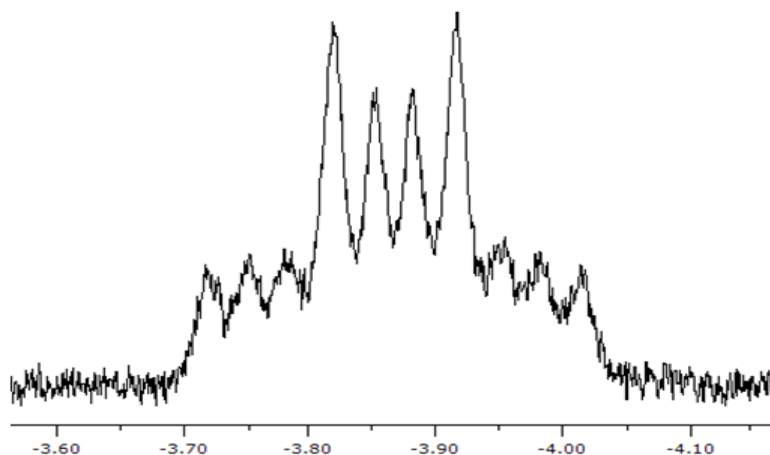


Figure 4.5.  $^{31}\text{P}$ - $^{31}\text{P}$  COSY of the  $[\text{Rh}_2\text{H}(\text{PPh}_2)_2(\text{PPh}_3)_3]^-$  ion.

The lack of coupling between the two phosphido ligands and the two equivalent phosphines on Rh(2) is presumably due to the tetrahedral geometry at the metal center. Meek and coworkers reported a  $^{31}\text{P}$  -  $^{31}\text{P}$  coupling constant of zero for a phosphine and phosphide ligand at a pseudo-tetrahedral Rh center on

$\text{Rh}(\text{Ph}_2\text{P}(\text{CH}_2)_3\text{P}(\text{Ph})(\text{CH}_2)_2\text{PPh}_2)\text{NO}$ .<sup>161</sup> The small coupling was attributed to the P-Rh-P bond angle being near the critical angle of sign change in the Karplus Equation, resulting in a coupling constant near zero. The closely related  $[(\text{Et}_3\text{P})_2\text{Rh}(\mu\text{-PPh}_2)_2\text{Rh}(\text{cod})]$  was subsequently reported and also has a negligible P-P coupling constant between the phosphines and phosphido ligands at the pseudo-tetrahedral Rh.<sup>139</sup>

The existence of the hydride ligand was confirmed by  $^1\text{H}$  NMR, which shows a second order signal at  $\delta = -3.9$  ppm (Figure 4.6). A proton-coupled  $^{31}\text{P}$  NMR experiment shows splitting of the  $\text{P}_A$  resonance into doublets ( $^2J(^1\text{P}_A, ^1\text{H}) = 52$  Hz) (Figure 4.7). This value is consistent with known phosphido-hydride coupling constants.<sup>162,163</sup> Proton coupling is not observed for signals **A** and **X**.



**Figure 4.6.**  $^1\text{H}$  NMR spectrum for  $[\text{Rh}_2\text{H}(\text{PPh}_2)_2(\text{PPh}_3)_3]^+$ . Data were recorded at 300 K at 500.1 MHz in Pyr.

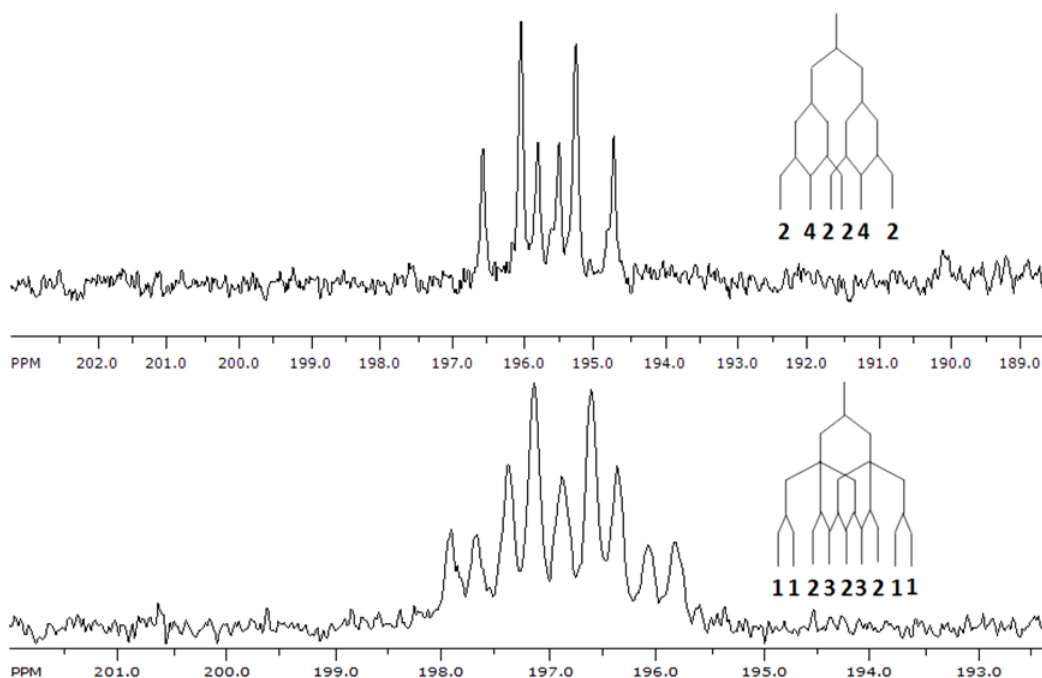


**Figure 4.7.** Phosphido signal in  $^{31}\text{P}\{^1\text{H}\}$  NMR (top) and  $^{31}\text{P}$  NMR (bottom) spectra for  $[\text{Rh}_2\text{H}(\text{PPh}_2)_2(\text{PPh}_3)_3]^-$ . Data were recorded at 300 K at 202.5 MHz in Pyr. Bottom spectrum shows coupling to hydride ligand.

The  $^{31}\text{P}$  NMR experiments provide information about both the structure of the complex and the dynamic properties. A proposed dynamic process is shown in Figure 4.8 in which the phosphine and hydride on Rh(1) undergo a pseudo-rotation through a tetrahedral intermediate. The tetrahedral-tetrahedral transition state contains a mirror plane that renders the two phosphido groups equivalent on the NMR time scale.



**Figure 4.8.** Dynamic exchange mechanism scheme for  $[\text{Rh}_2\text{H}(\text{PPh}_2)_2(\text{PPh}_3)_3]^-$ .

While it is possible to assign the present complex as a (II,0) or  $\text{Rh}_2(\text{I,I})$  dinuclear complex, a comparison with general structural parameters and rhodium-

phosphine bond lengths reported in the literature (Table 4.3) suggests that it is a Rh<sub>2</sub>(I,I) system. It is possible to maintain Rh<sub>2</sub>(II,0) mixed-valency with a dative metal-metal interaction between two asymmetric Rh centers. Meek and coworkers considered this electron counting scheme for the phosphido-bridged rhodium(II) dimer [(Et<sub>3</sub>P)<sub>2</sub>Rh(μ-PPh<sub>2</sub>)<sub>2</sub>Rh(cod)], where cod = 1,5-cyclooctadiene.<sup>139</sup> It was noted that if a dative bond is formed due to electron donation from the Rh(0) atom to the Rh(II) center, the difference in oxidation states should effectively cancel. Nocera reported the synthesis of Rh<sub>2</sub>[(F<sub>2</sub>P)-N(CH<sub>3</sub>)-(PF<sub>2</sub>)]Cl<sub>2</sub>(PF<sub>3</sub>), a rhodium dimer with an octahedral Rh(II) and trigonal bipyramidal Rh(0) metal center.<sup>164</sup> The system is described as a mixed valence Rh<sub>2</sub>(II,0) complex, but contains bidentate spanning fluorophosphine ligands rather than bridging organophosphides. Similarly, there is a single bond between the two rhodium atoms with a bond length of 2.785 Å. The mixed valency of the complex was confirmed by electronic absorption. The 2.75 Å Rh-Rh bond length of [Rh<sub>2</sub>H(PPh<sub>2</sub>)<sub>2</sub>(PPh<sub>3</sub>)<sub>3</sub>]<sup>-</sup> is shorter in length and is more consistent with a Rh<sub>2</sub>(I,I) dinuclear complex, as compared to other dirhodium complexes (Table 4.3).

### 4.3. Conclusion

The [Rh<sub>2</sub>H(PPh<sub>2</sub>)<sub>2</sub>(PPh<sub>3</sub>)<sub>3</sub>]<sup>-</sup> dimer results from the coupling of two RhCl(PPh<sub>3</sub>)<sub>3</sub> units by way of a multistep process. Triphenylphosphine is known to dissociate from Wilkinson's catalyst and is also known to react with K<sub>4</sub>Sn<sub>9</sub> to give PPh<sub>2</sub><sup>-</sup> and benzene after the extraction of a hydrogen atom; the reducing power of Sn<sub>9</sub><sup>4+</sup> allows the generation of phosphides that initiate the reaction. It is

also likely that Rh could abstract a hydrogen atom from the en solvent, which is frequently observed in low oxidation state Rh chemistry. However, the exact steps in the formation of the rhodium dimer are not known.

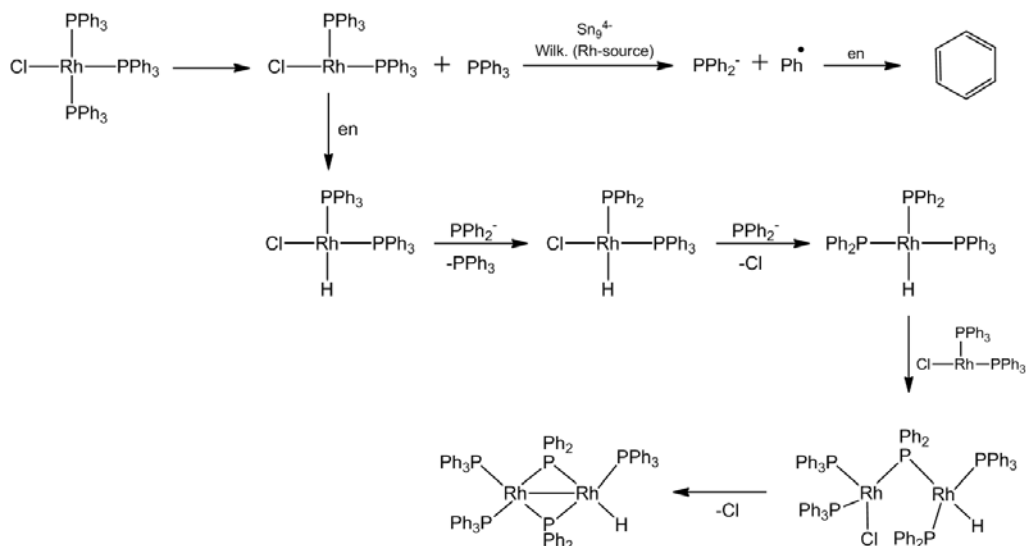


**Figure 4.9.** Proposed reaction pathway for the synthesis of  $[\text{Rh}_2\text{H}(\text{PPh}_2)_2(\text{PPh}_3)_3]^-$  anions.

Rhodium-substituted Zintl clusters were eventually isolated after considering the possible reaction pathway of  $[\text{Rh}_2\text{H}(\text{PPh}_2)_2(\text{PPh}_3)_3]^-$ . The reaction of  $\text{Sn}_9^{4-}$  and Wilkinson's catalyst in dmf solvent produced the  $\text{Rh}@ \text{Sn}_{10}^{3-}$  ion by eliminating en as a possible hydride source as detailed in Chapter 3. Additionally, replacing Wilkinson's catalyst with  $[\text{Rh}(\text{cod})\text{Cl}]_2$  in the presence of excess crypt afforded the  $\text{Sn}_9\text{Rh}(\text{cod})^{3-}$ ,  $\text{Rh}@ \text{Sn}_{10}^{3-}$ ,  $\text{Rh}@ \text{Sn}_{12}^{3-}$ , and  $\text{Rh}@ \text{Pb}_{12}^{3-}$  ions. This method was fruitful because it prevented the production of the highly reactive phosphides by completely removing the source of phosphides from the reactions.

The  $\text{Co}_3(\text{CO})_7^{3-}$  ion was synthesized in the reaction of  $\text{Co}_4(\text{CO})_{12}$  with  $\text{K}_4\text{Sn}_9$  in the presence of 2,2,2-crypt. Carbonylate ions of various transition metals are typically synthesized by placing neutral carbonyl complexes under the influence of a reducing agent.<sup>165</sup> The  $\text{Sn}_9^{4-}$  ion is the reducing agent in this reaction leading to the novel heptacarbonyl complex, as the alkali metal in this reaction is in its cationic form. To date, the  $\text{Sn}_9^{4-}$  ion is the only reducing agent capable of synthesizing the unusual  $\text{Co}_3(\text{CO})_7^{3-}$  complex. Efforts were placed in isolating the tricobalt cluster by employing sodium metal as a reducing agent, but to no avail. It is possible that the formation of  $\text{Co}_3(\text{CO})_7^{3-}$  in the presence of  $\text{Sn}_9^{4-}$  may be accompanied by the synthesis of a cobalt-substituted Zintl cluster from the  $\text{Co}_4(\text{CO})_{12}$  precursor; the isolation of the co-crystallized cobalt-tin Zintl clusters described in the appendix could potentially comprise the additional cobalt atom from the starting material.

The novel  $[(\text{C}_3\text{H}_7\text{N}_2\text{O})_3\text{Ir}_4(\text{CO})_9]^{3-}$  ion was synthesized in the reaction of  $\text{Ir}_4(\text{CO})_{12}$  with  $\text{Na}_4\text{As}_7$  in the presence of 2,2,2-crypt. This reaction also exploits the ability of Zintl ions to act as reducing agents, as  $\text{As}_7^{3-}$  likely reduces en to the  $\text{NH}_2\text{CH}_2\text{CH}_2\text{NH}^-$  amide, which we have unequivocally shown the  $\text{Sn}_9^{4-}$  ion to do.<sup>73</sup> In en solution, the amide reacts with the  $\text{Ir}_4(\text{CO})_{12}$  precursor to give a rare iridium-carbamoyl complex. The carbamoyl may form as a result of the nucleophilic addition of amide anions to the carbonyl ligands of  $\text{Ir}_4(\text{CO})_{12}$  or via CO insertion into the bond of a coordinated metal amide. No iridium-substituted Zintl cluster has been isolated to date from a reaction involving the  $\text{Ir}_4(\text{CO})_{12}$  complex.



## 4.4. Experimental Section

### 4.4.1. General Data

All reactions were performed in a nitrogen atmosphere dry box (Innovative Technology, Incorporated).  $^{31}\text{P}$  NMR spectra were recorded on a Bruker DRX 500 AVANCE spectrometer operating at 202.46 MHz.  $^{31}\text{P}$  chemical shifts were referenced against an external 85%  $\text{H}_3\text{PO}_4/\text{CD}_2\text{Cl}_2$  standard (0 ppm).

### 4.4.2. Chemicals

$\text{K}_4\text{Sn}_9$ ,  $\text{K}_4\text{Pb}_9$ , and  $\text{Na}_3\text{As}_7$  were made by high-temperature fusion (~1000 °C) of stoichiometric amounts of the elements. The chemicals were loaded into quartz tubes and carefully heated under  $\text{N}_2$  atmospheres with a natural gas/oxygen flame behind a blast shield. 4,7,13,16,21,24-Hexaoxa-1,10-diazobicyclo[8.8.8]hexacacosane (2,2,2-crypt) was purchased from Fisher. Tris(triphenylphosphine)rhodium(I) chloride (Wilkinson's Catalyst) and tetrairidium dodecacarbonyl were purchased from Aldrich. Tetracobalt dodecacarbonyl was purchased from Fisher. Anhydrous ethylenediamine (en) and pyridine (pyr) was purchased from Fisher, vacuum distilled from  $\text{K}_4\text{Sn}_9$ , and stored under dinitrogen. Toluene was distilled from sodium/benzophenone under dinitrogen and stored under dinitrogen.

#### 4.4.3. Synthesis

##### Preparation of $[\text{K}(\text{2,2,2-crypt})][\text{Rh}_2\text{H}(\text{PPh}_2)_2(\text{PPh}_3)_3]\cdot\text{tol}$

In vial 1,  $\text{K}_4\text{Sn}_9$  (163 mg, 0.133 mmol) was dissolved in en (~2 mL) and allowed to stir for 30 min, giving a dark red solution. Four equivalents of solid crypt (200 mg, 0.531 mmol) were added to the solution and allowed to stir for an hour. In vial 2, Wilkinson's Catalyst (246 mg, 0.266 mmol) was dissolved in toluene (~2 mL) to produce a red solution. The contents of vial 2 were slowly added to vial 1 and the reaction mixture was stirred for 2 h at room temperature to yield a dark brown solution. The reaction mixture was then filtered through tightly packed glass wool in a pipet. Red crystals formed in the reaction vessel after 2 days.  $^{31}\text{P}$  NMR (202.5 MHz, Pyr, 25 °C)  $\delta = 23.5$  ppm ( $^1J(^{31}\text{P}, ^{103}\text{Rh}) = 194$  Hz,  $^2J(^{31}\text{P}, ^{31}\text{P}) = 106$  Hz), 29.6 ppm ( $^1J(^{31}\text{P}, ^{103}\text{Rh}) = 208$  Hz), and 197.9 ppm ( $^1J(^{31}\text{P}, ^{103}\text{Rh}) = 156$  Hz,  $^1J(^{31}\text{P}, ^{103}\text{Rh}) = 110$  Hz,  $^2J(^{31}\text{P}, ^{31}\text{P}) = 106$  Hz). A similar procedure using  $\text{K}_4\text{Pb}_9$  gives the same results.

##### Preparation of $[\text{K}(\text{2,2,2-crypt})]_3[\text{Co}_3(\text{CO})_7]\cdot\text{solvent}$

In vial 1,  $\text{K}_4\text{Sn}_9$  (81 mg, 0.066 mmol) was dissolved in en (~2 mL), giving a dark red solution. Four equivalents of solid crypt (75 mg, 0.332 mmol) were added to the solution and allowed to stir for about 1hr. In vial 2,  $\text{Co}_4(\text{CO})_{12}$  (10 mg, 0.017 mmol) was mixed in toluene (~2 mL) to produce a light brown solution. The contents of vial 2 were slowly added to vial 1 and the reaction mixture was stirred for 6 h to yield a dark brown solution. The reaction mixture was then filtered through tightly packed glass wool. Brown crystals formed in the reaction vessel after two weeks.

### **Preparation of [Na(2,2,2-crypt)]<sub>3</sub>[(C<sub>3</sub>H<sub>7</sub>N<sub>2</sub>O)<sub>3</sub>Ir<sub>4</sub>(CO)<sub>9</sub>]•en**

In vial 1, Na<sub>3</sub>As<sub>7</sub> (39 mg, 0.066 mmol) was dissolved in en (~2 mL), giving a dark red solution. Three equivalents of solid crypt (75 mg, 0.332 mmol) were added to the solution and allowed to stir for about 10 minutes. In vial 2, Ir<sub>4</sub>(CO)<sub>12</sub> (37 mg, 0.033 mmol) was dissolved in toluene (~2 mL) to produce a yellow solution. The contents of vial 2 were slowly added to vial 1 and the reaction mixture was stirred for 2 h to yield a dark brown solution. The reaction mixture was then filtered through tightly packed glass wool in a pipet. Orange crystals formed in the reaction vessel after three weeks (61 mg, 72% yield).

### **Crystallographic Studies**

The crystal structures of the clusters were determined at the single crystal X-ray facility by Dr. Peter Zavalij at the Department of Chemistry and Biochemistry, University of Maryland, College Park.

## **Chapter 5: Fabrication of PtSn<sub>4</sub> and Ir<sub>3</sub>Sn<sub>7</sub> Intermetallic Nanoparticles From Bimetallic Zintl Cluster Precursors**

### **5.1. Introduction**

Bimetallic nanoparticles (NPs) of active Pt-group metals (PGMs) such as Rh, Ir, Pd and Pt are used in a variety of catalytic and electrocatalytic applications. While the PGMs provide the base activity of the catalyst, the secondary metals modify the PGM activity and/or impart tolerance to various poisons. For example, PtRu and PtFe bimetallic NP electrocatalysts show much higher tolerance to CO impurities in hydrogen fuel cell applications in comparison to pure Pt NPs.<sup>109,110</sup> One drawback of PtM alloy catalysts is their low chemical and electrochemical stability relative to pure Pt. These instabilities can lead to catalyst degradation, phase separation and ion migration in electrochemical applications.

In contrast, intermetallic NPs are often significantly more stable than alloys; especially in acidic media.<sup>111</sup> Alloys and intermetallics differ in their crystal structures and, usually, the degree of atomic order. Alloys typically adopt the crystal structures of one (or both) of the metallic end members and contain random distributions of atoms in homogenous solid solutions. Intermetallics adopt crystal structures distinct from the metal end members and typically contain ordered atomic lattices with higher lattice energies. Atomic ordering in intermetallic NPs can also be exploited to alter reaction pathways as has been well documented in the PtBi and PtPb intermetallic electrocatalysts used in formic acid fuel cells.<sup>111-113</sup> The semiconducting properties of the GaAs and InAs

monoarsenide intermetallics have also been described and are currently used in various applications such as infrared light-emitting devices, infrared detection, and solar cell technology.<sup>166-168</sup>

Bulk-phase Pt-Sn bimetallics have high activity in several catalytic systems<sup>169</sup> but Pt-Sn nanoparticles especially the Sn-rich NPs such as PtSn<sub>4</sub>, are difficult to prepare due to differences in reduction potentials. In 2000, Jeitschko reported the single-crystal X-ray structure of PtSn<sub>4</sub> using crystals obtained from the reaction between powdered platinum and tin metal.<sup>170</sup> The fabrication requires heating the elements in a Sn flux at 500 °C. The PtSn<sub>4</sub> intermetallic is isolated by dissolving the excess tin flux in dilute hydrochloric acid, resulting in low yields of PtSn<sub>4</sub> single crystals. PtSn<sub>4</sub> NPs are particularly difficult to isolate in pure form due to the presence of competing Pt<sub>3</sub>Sn, PtSn, Pt<sub>2</sub>Sn<sub>3</sub> and PtSn<sub>2</sub> phases.<sup>116,170</sup> While Schaak has successfully prepared the Pt-rich intermetallic NPs,<sup>171,172</sup> the corresponding PtSn<sub>4</sub> NPs have not previously been reported to our knowledge. It would be advantageous to develop a new PtSn<sub>4</sub> fabrication method requiring a more reasonable stoichiometry of platinum and tin and that did not require such high temperatures or a controlled cooling rate.

Similarly, other PGMs alloys are traditionally isolated from the high temperature reaction of the elements in reactions approaching 1000 °C. As a result of these conditions, bulk materials are isolated as the agglomeration of particles is favored. Due to the unique catalytic activity and enhanced stability of intermetallic catalysts, recent efforts have been devoted to preparing small intermetallic NPs to optimize surface area and atom economy, making the

development of low temperature reactions desirable. Polyol and seeded growth methods have been employed to prepare PtM NPs where M = Bi, Pb but these methods require moderate temperature annealing steps to induce crystallographic ordering (*i.e.* intermetallic formation), which can lead to undesirable particle growth.<sup>114</sup> Ultrasonically mixing transition metal chlorides and arsenic in the presence of potassium borohydride at a relatively low temperature of 100 °C has also shown marked success in affording FeAs, CoAs, and NiAs NPs, though the NPs are very large at 20-35 nm.<sup>173</sup> As a result, there are only a few known examples of small (< 8 nm) intermetallic NPs despite the promising properties of the catalysts.<sup>115-120</sup> For example, the face-centered tetragonal PtSn intermetallic electrocatalyst shows marked improvements in stability and CO tolerance in hydrogen electrooxidation applications when compared to the PtSn alloy or Pt NP catalysts of similar size.<sup>118</sup> Likewise, the 2-3 nm PtBi intermetallics recently reported by Nazar show significantly higher mass activity for formic acid electrooxidation relative to other known catalysts.<sup>121</sup>

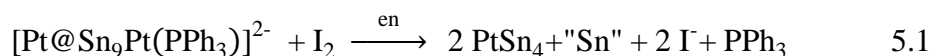
This chapter will discuss the use of  $\text{Sn}_9\text{Pt}_2(\text{PPh}_3)^{2-}$  and  $\text{Sn}_9\text{Ir}(\text{cod})^{3-}$  molecular Zintl cluster precursors<sup>58,123,124</sup> that give sub-8 nm intermetallic particles of PtSn<sub>4</sub> and Ir<sub>3</sub>Sn<sub>7</sub>. The structures of the cluster precursors are remarkably similar to the M<sub>9</sub>Sn<sub>8</sub> subunits that define the respective intermetallic crystal lattices. While the  $\text{Sn}_9\text{Pt}_2(\text{PPh}_3)^{2-}$  cluster is also compositionally close to the PtSn<sub>4</sub> intermetallic (Pt:Sn = 1 : 4.5 versus 1 : 4), the  $\text{Sn}_9\text{Ir}(\text{cod})^{3-}$  precursor is significantly tin rich relative to the Ir<sub>3</sub>Sn<sub>7</sub> phase (Ir:Sn = 1 : 9 versus 1 : 2.33). Although the composition of  $\text{Sn}_9\text{Ir}(\text{cod})^{3-}$  is much closer to the known IrSn<sub>4</sub>

intermetallic,<sup>174</sup> its structure is more akin to that of Ir<sub>3</sub>Sn<sub>7</sub>. These results suggest that structural pre-organization of cluster precursors can be exploited to produce phase specific small intermetallic NPs.

## 5.2. Results

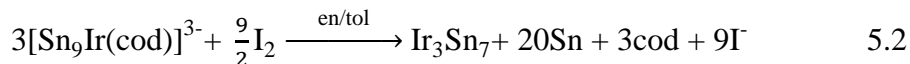
### 5.2.1. Synthesis

**PtSn<sub>4</sub>:** Ordered PtSn<sub>4</sub> intermetallic NPs were fabricated via the oxidation of the Pt<sub>2</sub>Sn<sub>9</sub>(PPh<sub>3</sub>)<sup>2-</sup> cluster with elemental iodine at room temperature (eq. 1). The cluster precursor was prepared from a 1:1 mole ratio of K<sub>4</sub>Sn<sub>9</sub> and Pt(PPh<sub>3</sub>)<sub>4</sub> in ethylenediamine (en) in the presence of 2,2,2-crypt as previously reported by the Eichhorn group under a nitrogen atmosphere.<sup>14</sup> The PtSn<sub>4</sub> NPs were simply washed with hexanes, collected by centrifugation and characterized by TEM, EDX and XRD analysis. These characterization methods confirmed the identity of the small PtSn<sub>4</sub> intermetallic NPs and that the mild hexanes rinse was sufficient to obtain clean material.



**Ir<sub>3</sub>Sn<sub>7</sub>:** Similarly, ordered Ir<sub>3</sub>Sn<sub>7</sub> intermetallic NPs were prepared via the oxidation of en solutions of [Sn<sub>9</sub>Ir(cod)]<sup>3-</sup> with toluene solutions of iodine at room temperature (eq. 2). The [Sn<sub>9</sub>Ir(cod)]<sup>3-</sup> precursor was prepared *in situ* through the reaction of ethylenediamine solutions of K<sub>4</sub>Sn<sub>9</sub> and toluene solutions of [Ir(cod)Cl]<sub>2</sub> in the presence of 2,2,2-crypt under a nitrogen atmosphere, as the Zintl precursor is air and moisture sensitive.<sup>15</sup> The synthesis and characterization of the [Sn<sub>9</sub>Ir(cod)]<sup>3-</sup> cluster were carried out as detailed in Chapter 2. The Ir<sub>3</sub>Sn<sub>7</sub>

NPs were washed with acetone, collected by centrifugation and characterized by XRD and TEM.



Unlike the clean fabrication of PtSn<sub>4</sub>, the as-prepared Ir<sub>3</sub>Sn<sub>7</sub> NPs contain a preponderance of Sn metal as expected from the stoichiometry of Eq. 5.2 (Figure 5.3b). 20 equivalents of excess tin metal are generated per mole of intermetallic, which must be removed to obtain pure material. The Sn metal was removed with a nitric acid wash (0.1 M) giving essentially amorphous Ir<sub>3</sub>Sn<sub>7</sub> NPs as observed via XRD analysis (Figure 5.5). Annealing the NPs at 450 °C gives pseudo crystalline samples that retain their small size as illustrated by TEM (Figure 5.5a). The annealed samples remain amorphous by XRD analysis, making TEM a reliable tool to observe and identify the particles by measuring the lattice spacings of the material.

### ***5.2.2. Powder X-ray Diffraction and Transition Microscopy Studies***

The XRD data of the as-prepared NPs clearly show the distinctive reflections associated with the PtSn<sub>4</sub> intermetallic (Figure 5.1b). EDX analysis gives a 1 : 4 ratio of Pt to Sn and, although the cluster precursor is slightly Sn rich, the excess tin in either the XRD studies or the TEM / EDX analysis is not detectable. Thus, the excess tin is likely washed away in the hexanes rinse as there is very little tin waste as compared to the Ir<sub>3</sub>Sn<sub>7</sub> fabrication process. The particles form agglomerates, most likely due to the absence of particle stabilizers



that aid in colloidal dispersion. Though agglomerated, the particles are discernible as sub-10 nm particles. The 2.32 Å d-spacing associated with the 213 facet at 39.7° is observed on a NP depicted in Figure 5.1a.

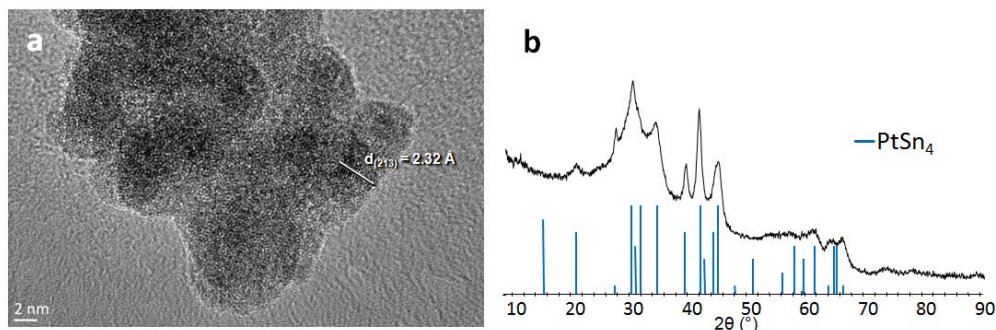


**Figure 5.1.** (a) The High resolution TEM image and (b) X-ray diffraction experiment of ‘as-prepared’ sub-10 nm ordered  $\text{PtSn}_4$  nanoparticles ( $\text{PtSn}_4$  04-0744). The 2.32 Å d-spacing is associated with the 213 facet at 39.7°.

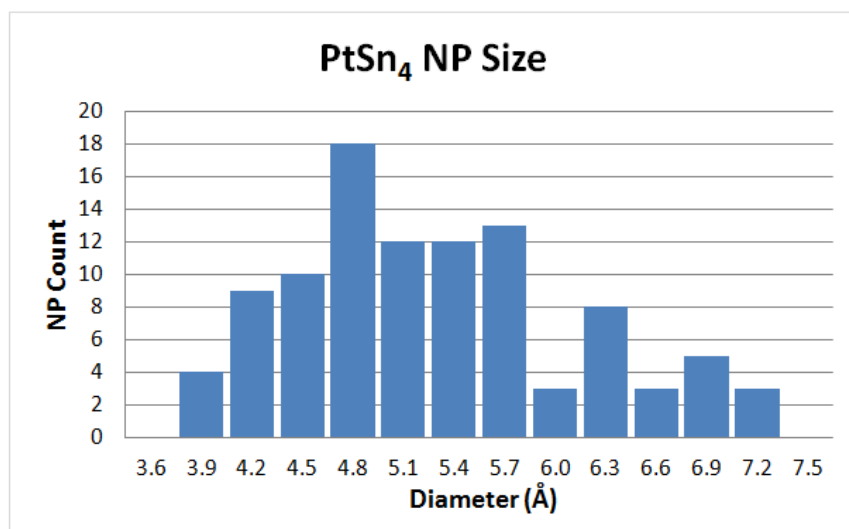


**Figure 5.2.** Nanoparticle size distribution of  $\text{PtSn}_4$  particles.

The  $\text{Ir}_3\text{Sn}_7$  NPs form aggregates of 6-13 nm particles. The agglomeration presumably results from the lack of capping agents used in the synthesis process. The XRD analysis of the crude NP product clearly shows the presence of the  $\text{Ir}_3\text{Sn}_7$  phase in the presence of the strong reflections of Sn metal (Figure 5.3b).

After the HNO<sub>3</sub> wash, some of the Ir<sub>3</sub>Sn<sub>7</sub> diffraction lines are discernible by TEM (Figure 5.3a) but the sample is essentially amorphous to X-rays. However, the TEM image shows only Ir<sub>3</sub>Sn<sub>7</sub> NPs as indicated by the distinctive lattice fringes with 200, 211, 222, and 330 facets (19.0°, 23.3°, 33.2°, and 40.9° respectively); the most prominent corresponding to the 4.71 Å d-spacing associated with the 200 lattice plane.

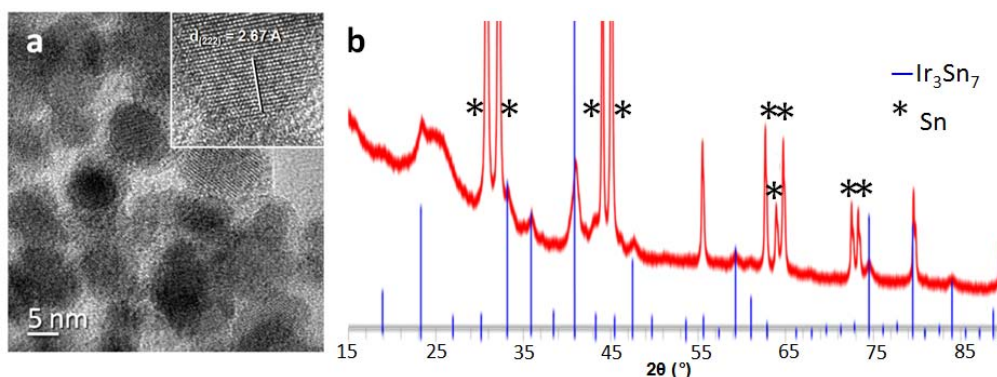


**Figure 5.3.** (a) The high-resolution TEM image and (b) X-ray diffraction data of annealed intermetallic Ir<sub>3</sub>Sn<sub>7</sub> nanoparticles. The particles for the TEM experiments were washed with nitric acid to remove the excess Sn (Ir<sub>3</sub>Sn<sub>7</sub> 00-004-0673).

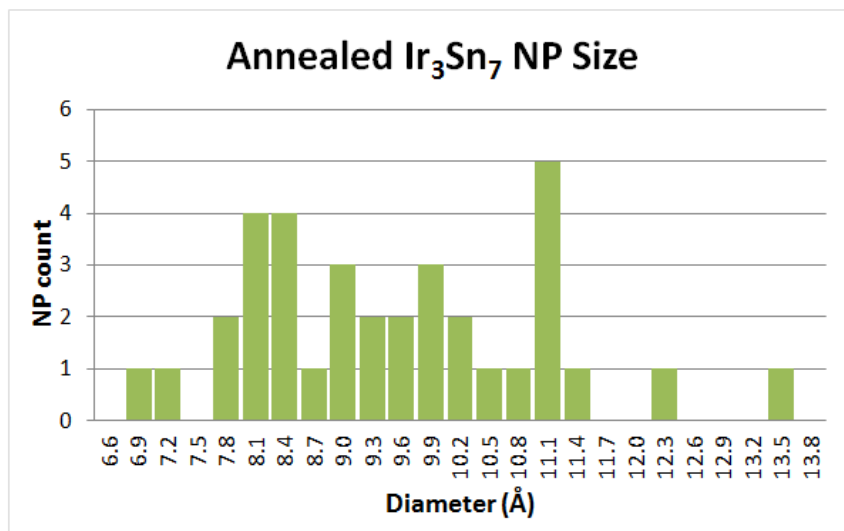


**Figure 5.4.** Nanoparticle size distribution of Ir<sub>3</sub>Sn<sub>7</sub> particles.

Since the  $[\text{Sn}_9\text{Ir}(\text{cod})]^{3-}$  precursor is closer in composition to the  $\text{IrSn}_4$  intermetallic, which is not observed in our experiments, we studied the effect of stoichiometry to see if alternate phases could be produced. In all cases, the  $\text{K}_4\text{Sn}_9$  and  $[\text{Ir}(\text{cod})\text{Cl}]_2$  precursors were pre-mixed in the presence of 2,2,2-crypt prior to oxidation, as is required for  $[\text{Sn}_9\text{Ir}(\text{cod})]^{3-}$  cluster formation. Three different Ir:Sn ratios were investigated; 1:9, 1:4.5, and 3:7, but all reactions gave exclusively  $\text{Ir}_3\text{Sn}_7$  in the presence of large excesses of metallic Sn. In the absence of 2,2,2-crypt, only Sn metal was observed by XRD and no intermetallic formation was detected (Figure 5.5). These data suggest that the  $[\text{Sn}_9\text{Ir}(\text{cod})]^{3-}$  cluster is a necessary intermediate in the formation of  $\text{Ir}_3\text{Sn}_7$ .

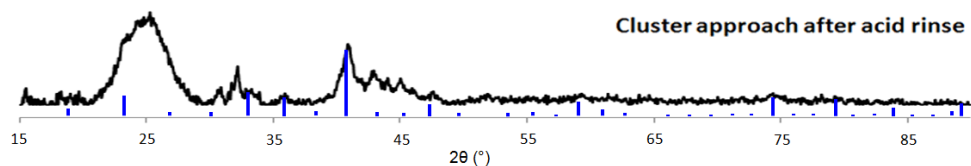


**Figure 5.5.** X-ray diffraction experiment of annealed, nitric acid-rinsed intermetallic  $\text{Ir}_3\text{Sn}_7$  nanoparticles on XC-72 carbon support ( $\text{Ir}_3\text{Sn}_7$  00-004-0673).

As further evidence for the Zintl cluster route of the fabrication of the two NPs, co-reduction experiments were conducted in attempts to isolate the materials through a more traditional method. In the case of the  $\text{Ir}_3\text{Sn}_7$  phase,  $\text{K}_4\text{Sn}_9$  and  $[\text{Ir}(\text{cod})\text{Cl}]_2$  precursors were reacted with an iridium-tin ratio of 3:7, in the presence of 2,2,2-crypt and sodium triethylborohydride as a reducing agent. Neither fabrication method afforded measureable amounts of the desired  $\text{PtSn}_4$  or  $\text{Ir}_3\text{Sn}_7$  phases by XRD experiments. In the case of the  $\text{IrSn}$  system, the same precursors were used as in the Zintl cluster route indicating the necessity of the

synthesis of the  $[\text{Sn}_9\text{Ir}(\text{cod})]^{3-}$  ion as a precursor due to its similarity in molecular structure to the crystal lattice of  $\text{Ir}_3\text{Sn}_7$  (Figure 5.5).

### 5.3. Discussion

The  $\text{PtSn}_8$  subunits that define the structures of the  $\text{PtSn}_4$  intermetallic and the  $\text{Pt}@\text{Sn}_9\text{Pt}(\text{PPh}_3)^{2-}$  cluster are strikingly similar, as illustrated in Figure 5.6 and Table 5.1. The  $\text{Pt}@\text{Sn}_9\text{Pt}(\text{PPh}_3)^{2-}$  ion has  $C_{3v}$  point symmetry with a 9-coordinate endohedral Pt atom. However, the structure can be viewed as a distorted monocapped square antiprism as is emphasized in Figure 5.6c. The crystal structure of  $\text{PtSn}_4$ , Figure 5.6a-b, contains very regular  $\text{PtSn}_8$  square antiprism repeat units, which define the orthorhombic *Ccca*  $\text{PtSn}_4$  lattice. The  $\text{PtSn}_4$  structure contains two-dimensional arrays of the  $\text{PtSn}_{8/2}$  square antiprisms that share common edges in the x-y plane. The layers are linked by weak Sn-Sn bonds ( $d_{\text{Sn-Sn}} = 2.7(3)$  Å, ave.) along the z direction of the monoclinic cell.<sup>170,174</sup> The 8 Pt-Sn contacts within the square antiprismatic subunits of both the  $\text{PtSn}_4$  intermetallic and the  $\text{Pt}@\text{Sn}_9\text{Pt}(\text{PPh}_3)^{2-}$  are equivalent at 2.75(1) Å, ave.<sup>58</sup> Aside from the slight trigonal elongation of the  $\text{PtSn}_8$  subunit in the  $\text{Pt}@\text{Sn}_9\text{Pt}(\text{PPh}_3)^{2-}$  ion, the cluster is ideally pre-organized to form the  $\text{PtSn}_4$  intermetallic.

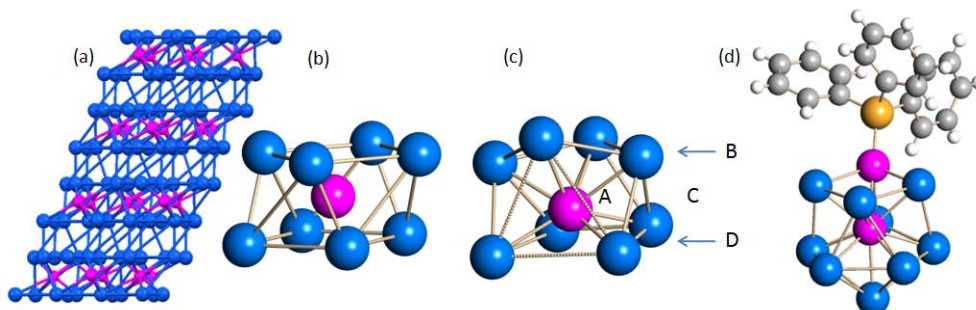


**Figure 5.6.** (a) Crystal lattice of  $\text{PtSn}_4$  (pink = Pt, blue = Sn); (b) atomic arrangement of Sn atoms about each Pt atom in  $\text{PtSn}_4$ ; (c) the  $\text{PtSn}_8$  subunit of the  $\text{Pt@Sn}_9\text{Pt}(\text{PPh}_3)_2^{2-}$  cluster showing the similarity to the structure of  $\text{PtSn}_4$ ; (d) the  $\text{Pt@Sn}_9\text{Pt}(\text{PPh}_3)_2^{2-}$  cluster.<sup>58,170</sup>

Structural similarities are also present between the  $\text{Ir}_3\text{Sn}_7$  intermetallic and the  $\text{Sn}_9\text{Ir}(\text{cod})^{3-}$  ion as shown in Figure 5.7. The  $\text{IrSn}_4$  square pyramid (Figure 5.7c) associated with the monocapped square anti-prism of  $\text{Sn}_9\text{Ir}(\text{cod})^{3-}$  in Figure 5.7d is also found in the crystal lattice of  $\text{Ir}_3\text{Sn}_7$  as a repeating subunit (Figure 5.7b).<sup>175,176</sup> The fundamental  $\text{Ir}_2\text{Sn}_{12}$  structural subunit in the  $\text{Ir}_3\text{Sn}_7$  crystal lattice contains two  $\text{IrSn}_8$  square antiprisms that share a common face (Figure 5.7b). These  $\text{Ir}_2\text{Sn}_{12}$  double prisms share common corners with other double prisms to make a cubic array with  $Im\text{-}3m$  crystal symmetry (Figure 5.7a).<sup>175,176</sup> The structure of  $[\text{Sn}_9\text{Ir}(\text{cod})]^{3-}$  contains an Ir-capped square antiprism but the endohedral Ir atom is missing. However, the  $\text{IrSn}_4$  capped square prismatic subunits of the  $\text{Ir}_3\text{Sn}_7$  intermetallic and the  $\text{Sn}_9\text{Ir}(\text{cod})^{3-}$  cluster anion are quite similar with equivalent Ir-Sn contacts of 2.77(9) Å, ave (Figure 5.7 group A, Table 5.1). The Sn-Sn contacts of  $\text{Sn}_9\text{Ir}(\text{cod})^{3-}$  are more varied than those of  $\text{Ir}_3\text{Sn}_7$ ; especially groups B and C (See Table 5.1). These differences are not unexpected in view of the differences in composition and charge.

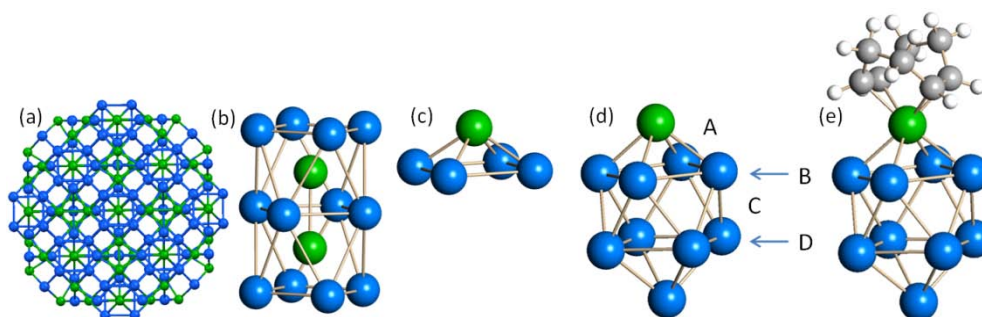


**Figure 5.7.** (a) Crystal lattice of  $\text{Ir}_3\text{Sn}_7$  (green = Ir, blue = Sn); (b) the  $\text{Ir}_2\text{Sn}_{12}$  subunit in the  $\text{Ir}_3\text{Sn}_7$  crystal lattice; (c)  $\text{IrSn}_4$  subunits in  $\text{Ir}_3\text{Sn}_7$ ; (d) The  $\text{IrSn}_9$  core of the  $[\text{Sn}_9\text{Ir}(\text{cod})]^{3-}$  ion; (e) the  $[\text{Sn}_9\text{Ir}(\text{cod})]^{3-}$  cluster anion.

**Table 5.1.** Average bond lengths of Zintl clusters and intermetallics (Å).

Subgroups	$\text{PtSn}_4$ <sup>(a)</sup>	$[\text{Sn}_9\text{Pt}_2(\text{PPh}_3)]^{2-}$ <sup>(b)</sup>	$\text{Ir}_3\text{Sn}_7$ <sup>(c)</sup>	$[\text{Sn}_9\text{Ir}(\text{cod})]^{3-}$ <sup>(d)</sup>
<b>A</b> (M-Sn) M=Pt,Ir	2.766	2.746(9)	2.762	2.770(9)
<b>B</b> (Sn-Sn)upper square	3.376	3.052(52)	3.307	3.110(27)
<b>C</b> (Sn-Sn)waist	3.390	3.291(68)	3.582	2.989(22)
<b>D</b> (Sn-Sn)lower square	3.376	3.543(4)	3.086	3.151(56)

(a) ref.<sup>170</sup> (b) ref.<sup>58</sup> (c) ref.<sup>176</sup> (d) ref.<sup>124</sup>

There are 3 forms of  $\text{IrSn}_4$ ;  $\alpha\text{-IrSn}_4$ ,  $\beta\text{-IrSn}_4$  and  $\text{HT-IrSn}_4$ . The latter 2 phases are very similar to the  $\text{PtSn}_4$  structure but are only found at high temperature or pressure.  $\alpha\text{-IrSn}_4$  is the ambient phase but has a trigonal structure with distorted bisdisphenoid  $\text{IrSn}_8$  subunits that are quite distinct from the  $\text{PtSn}_4$ -type subunits.<sup>174</sup> The presence of the  $\text{IrSn}_4$  square pyramids throughout the  $\text{Ir}_3\text{Sn}_7$  crystal lattice apparently leads to its selective formation over other phases in the oxidation of  $[\text{Sn}_9\text{Ir}(\text{cod})]^{3-}$ .

The atomic pre-organization of  $[\text{Sn}_9\text{Pt}_2(\text{PPh}_3)]^{2-}$  and  $[\text{Sn}_9\text{Ir}(\text{cod})]^{3-}$  provides a direct, facile route to the fabrication of ordered intermetallic NPs that are difficult to prepare by other methods. In the case of the  $\text{Ir}_3\text{Sn}_7$  NPs, the importance of cluster structure over stoichiometry is particularly supported by the

discrepancy in Ir:Sn ratios between the intermetallic and cluster. Despite the 1:9 atomic ratio, ordered Ir<sub>3</sub>Sn<sub>7</sub> NPs were formed instead of the more stoichiometric IrSn<sub>4</sub> phases.

Many bimetallic Zintl clusters isolated to date are composed of elements pertinent to various catalytic applications including [Pt@Pb<sub>12</sub>]<sup>2-</sup>, [Pd<sub>2</sub>@Sn<sub>18</sub>]<sup>4-</sup>, [Sn<sub>9</sub>Ni<sub>2</sub>(CO)]<sup>3-</sup>, and [Pb<sub>9</sub>Ir(cod)]<sup>3-</sup> to name a few.<sup>52,58,85,99,124</sup> PdPb, PbSn, PtSn, and IrSn phases have been studied for use in direct formic acid fuel cells, as hydrogenation catalysts, oil reforming catalysts, and for use in direct ethanol fuel cells.<sup>169,177-179</sup> The facile room temperature synthesis of the PtSn<sub>4</sub> and Ir<sub>3</sub>Sn<sub>7</sub> NPs is important because it provides a pathway to small, ordered NPs making them readily available for the first time. The findings of this study show that the fabrication method may possibly be extended to other transition metal-stannide systems currently under investigation that could potentially yield other catalytically active materials. The catalytic activity of these various NPs could potentially be tested in future studies, while we also aim to compare and contrast the catalytic activity of the well-studied PtSn and Pt<sub>3</sub>Sn phases.

## 5.4. Conclusion

Controlled I<sub>2</sub> oxidations of preformed Zintl clusters [Pt<sub>2</sub>Sn<sub>9</sub>(PPh<sub>3</sub>)]<sup>2-</sup> and [Sn<sub>9</sub>Ir(cod)]<sup>3-</sup>, give well ordered tin-rich intermetallic NPs of PtSn<sub>4</sub> and Ir<sub>3</sub>Sn<sub>7</sub>, respectively. These materials were made accessible as NPs for the first time. The facile nature of the Zintl cluster route of fabrication can most likely be attributed to the atomic pre-organization of Sn<sub>9</sub>Pt<sub>2</sub>(PPh<sub>3</sub>)]<sup>2-</sup> and [Sn<sub>9</sub>Ir(cod)]<sup>3-</sup>; this

direct route to the catalytic intermetallics that are difficult to prepare by other methods. The intermetallics were characterized via HR-TEM and XRD analysis.

Both clusters have strong structural similarities with the final intermetallic, which appears to be an important factor in determining the phase of the resulting intermetallic NP. The distorted monocapped square antiprismatic structure of the  $[\text{Pt}_2\text{Sn}_9(\text{PPh}_3)]^{2-}$  cluster is comparable to the skeletal make up of the  $\text{PtSn}_4$  intermetallic phase; the intermetallic contains very regular  $\text{PtSn}_8$  square antiprism units. Beyond initial expectations, the oxidation of the  $[\text{Sn}_9\text{Ir}(\text{cod})]^{3-}$  cluster yields crystalline  $\text{Ir}_3\text{Sn}_7$  NPs instead of the  $\text{IrSn}_4$  phase, which is compositionally more similar to the iridium-based cluster. The preference of the  $[\text{Sn}_9\text{Ir}(\text{cod})]^{3-}$  ion towards the fabrication of  $\text{Ir}_3\text{Sn}_7$  is presumably driven by the Ir-Sn bonding motif in the bicapped square antiprism and square pyramid of the respective structures. These key findings show that the fabrication method may possibly be extended to other transition metal-stannide systems to provide accessibility to additional catalytically active materials currently under investigation. The catalytic activity of the studied NPs could also potentially be tested in future studies in comparison to the well-studied  $\text{PtSn}$  and  $\text{Pt}_3\text{Sn}$  phases.

## 5.5. Experimental Section

### 5.5.1. General Data

All reactions were performed in a nitrogen atmosphere dry box. A Bruker D8 Advance  $\theta$ - $\theta$  X-ray Powder Diffractometer ( $\text{CuK}_\alpha$  radiation, LynxEye detector) was used to obtain XRD patterns for phase identification. A step width



of  $0.02^\circ$  between of  $15^\circ \leq 2\theta \leq 90^\circ$  was used. Analysis of the XRD patterns was done using the Eva® software package equipped with the JC-PDF database. Samples for TEM imaging were prepared by dispersing the sample in ~ 1 mL of dmf and a drop was placed on copper grid and the grid was allowed to dry. The TEM images in Figures 5.1 and 5.2 were collected on a JEOL 2100F Transmission Electron Microscope at an accelerating voltage of 160 kV. The reported lattice fringes were measured several times to determine the average distance of the lattice spacings.

### **5.5.2. Chemicals**

$K_4Sn_9$  was made by high-temperature fusion (~1000 °C) of stoichiometric amounts of the elements. The chemicals were loaded into evacuated quartz tubes and carefully heated with a natural gas/oxygen flame behind a blast shield. Bis(1,5-cyclooctadiene)diiridium(I) dichloride, iodine, and tetrakis(triphenylphosphine)platinum(0) were purchased from Aldrich. 4,7,13,16,21,24-Hexaoxa-1,10-diazobicyclo[8.8.8]hexacacosane (2,2,2-crypt) was purchased from Fisher. Anhydrous ethylenediamine (en) and pyridine (pyr) were purchased from Fisher, vacuum distilled from  $K_4Sn_9$ , and stored under dinitrogen. Toluene was distilled from sodium/benzophenone under dinitrogen and stored under dinitrogen. Concentrated HCl was diluted to 0.01M with distilled water.

### 5.5.3. Synthesis

#### Fabrication of PtSn<sub>4</sub> nanoparticles

A previously published protocol<sup>58</sup> was followed to synthesize [K(2,2,2-crypt)]<sub>2</sub>[Sn<sub>9</sub>Pt<sub>2</sub>(PPh<sub>3</sub>)] precursor. In vial 1, K<sub>4</sub>Sn<sub>9</sub> (80 mg, 0.065 mmol) was dissolved in en (~2 mL), giving a dark red solution. Four equivalents of solid crypt (98 mg, 0.260 mmol) were added to the solution and allowed to stir for an hour. In vial 2, Pt(PPh<sub>3</sub>)<sub>4</sub> (81 mg, 0.065 mmol) was dissolved in toluene (~2 mL) to produce yellow solution. The contents of vial 2 were slowly added to vial 1 and the reaction mixture was stirred for 2 h to yield a dark brown solution. The reaction mixture was then filtered through tightly packed glass wool in a pipet. Dark red crystals formed in the reaction vessel after 2 weeks. <sup>31</sup>P NMR (162.0 MHz, Pyr, 25 °C) δ = 34.8 ppm (<sup>1</sup>J(<sup>195</sup>Pt, <sup>31</sup>P) = 4777 Hz, <sup>2</sup>J(<sup>195</sup>Pt, <sup>31</sup>P) = 296 Hz). [K(2,2,2-crypt)]<sub>2</sub>[Sn<sub>9</sub>Pt<sub>2</sub>(PPh<sub>3</sub>)] crystals (10 mg, 0.004 mmol) dissolved and stirred in ethylenediamine for ten minutes. Elemental iodine (10 mg, 0.038 mmol) dissolved in minimal toluene was added to solution of [K(2,2,2-crypt)]<sub>2</sub>[Sn<sub>9</sub>Pt<sub>2</sub>(PPh<sub>3</sub>)] dropwise and stirred for an hour. Solution precipitates, giving a black solid. Solvent drained off and particles rinsed in hexanes, sonicated, and isolated via centrifugation. The cell parameters match those given for the JCPDS card PtSn<sub>4</sub>, #04-0744.

#### Fabrication of Ir<sub>3</sub>Sn<sub>7</sub> nanoparticles

A previously published protocol<sup>124</sup> was followed to synthesize K(2,2,2-crypt)]<sub>3</sub>[Sn<sub>9</sub>Ir(cod)] precursor. In vial 1, K<sub>4</sub>Sn<sub>9</sub> (54 mg, 0.044 mmol) was dissolved in en (~2 mL), giving a dark red solution. Three equivalents of solid

crypt (50 mg, 0.133 mmol) were added to the solution and allowed to stir for an hour. In vial 2,  $[\text{Ir}(\text{C}_8\text{H}_{12})\text{Cl}]_2$  (30 mg, 0.044 mmol) was dissolved in toluene (~2 mL) to produce an orange-yellow solution. The contents of vial 2 were slowly added to vial 1 and the reaction mixture was stirred for 2 h to yield a dark brown solution. The reaction mixture was then filtered through tightly packed glass wool in a pipet. Elemental iodine (10 mg, 0.038 mmol) dissolved in minimal toluene was added to the reaction solution dropwise and stirred for an hour. Solution precipitates, giving a black solid. Solvent drained off and particles rinsed in acetone, dispersed, and isolated via centrifugation. Excess tin removed by nitric acid rinse. The cell parameters match those given for the JCPDS card  $\text{Ir}_3\text{Sn}_7$ , #00-004-0673.

### **IrSn co-reduction**

$\text{K}_4\text{Sn}_9$  (54 mg, 0.044 mmol),  $[\text{Ir}(\text{C}_8\text{H}_{12})\text{Cl}]_2$  (57 mg, 0.085 mmol), and three equivalents of solid crypt (50 mg, 0.133 mmol) were mixed in 20 mL of phenyl ether under nitrogen and stirred. Temperature increased to 200 °C and 1.0 M  $\text{Na}(\text{BHEt}_3)$  carefully added to the reaction. Reaction mixture refluxed for 30 minutes then allowed to cool to RT. Solvent drained off of black solid and particles rinsed in ethanol, dispersed, and isolated via centrifugation.

## Chapter 6: Conclusions

Bimetallic Zintl ions are important because of their ability to influence the field of nanotechnology. This thesis describes the synthesis of bimetallic Zintl clusters and their use in the fabrication of intermetallic nanoparticles. Various novel group 9 transition metal derivatives of  $\text{Sn}_9^{4-}$  and  $\text{Pb}_9^{4-}$  of nuclearities ranging from 8-12 were isolated and characterized by X-ray crystallography and NMR spectroscopy. The controlled oxidation of  $\text{Sn}_9\text{Ir}(\text{cod})^{3-}$  and  $\text{Sn}_9\text{Pt}_2(\text{PPh}_3)^{2-}$  clusters afforded intermetallic NPs.

Novel metallic complexes were synthesized in these studies as a result of the reducing properties of the  $\text{E}_9^{4-}$  and  $\text{E}_7^{3-}$  parent Zintl ions. The high charge of the cluster anions likely gives them their reducing properties. These rare soluble reducing agents are strong enough to reduce “non-reducible” precursors such as organic phosphines and ethylenediamine, as well as zero-valent metals such as cobalt(0) complexes.

The successful incorporation of group 9 metals into Zintl clusters is significant because it provides a new set of PGM metal cluster derivatives for future use as precursors to new intermetallic NPs. This work also expands the isolated bimetallic stannides and plumbides beyond the group 6 and group 10 derivatives, which implies that derivatives from transition metals from groups 3-8 may also be attainable. In concurrent studies by Goicoechea,<sup>89</sup> the  $\text{Fe}@\text{Ge}_{10}^{3-}$  iron germanide cluster has been characterized, but the isolation of Zintl cluster group 8 PGMs (Ru, Os) derivatives has yet to occur. Isolation of Zintl cluster derivatives of the early transition metals will lead to clusters with interesting

properties. It is anticipated that these clusters will exhibit magnetic properties due to the unpaired electrons of the early transition metals.

The structures of the  $\text{Rh@Pb}_{12}^{3-}$  and  $\text{Ir@Pb}_{12}^{3-}$  ions are closely related to the group 10  $\text{M@Pb}_{12}^{2-}$  plumbaspherenes ( $\text{M} = \text{Ni, Pd, Pt}$ ). The group 10 series of plumbaspherenes have extremely downfield  $^{207}\text{Pb}$  chemical shifts, due to the  $\sigma$ -aromaticity of the icosahedral ions. Similar findings were detailed in this thesis, where the group 9 derivatives have record  $^{207}\text{Pb}$  chemical shifts that possess the most down field chemical shifts known to date. These findings confirm that the high chemical shift result of the group 10 complexes are a direct result of the icosahedral nature of the Zintl cluster, and less reliant on the Ni, Pd, and Pt atoms.

This work provides insight into the factors that affect  $\sigma$ -aromaticity. The icosahedral group 9 derivatives possess higher chemical shifts than the group 10 clusters by over 800 ppm, and now possess the highest  $^{207}\text{Pb}$  chemical shifts known to date. The drastic chemical shift increase suggests that the increased charge on the cluster anions, or perhaps different electronic interactions between the core and shell atoms, causes an increase in the aromaticity of the clusters. This observation indicates that  $\sigma$ -aromaticity is also directly affected by metal substituents in addition to the spherical nature of the structures. It is therefore imperative that future studies target group 8 icosahedral derivatives to observe if these clusters have enhanced aromaticity.

In this study, bimetallic Zintl clusters were utilized as precursors to access intermetallic NPs which has been a long term goal of the field of Zintl cluster

chemistry. The use of Zintl clusters in NP fabrication is also critical because it is the first application of the cluster anions. The Zintl cluster approach to NP fabrication is beneficial because it bypasses some of the major synthetic issues associated with current intermetallic fabrication methods. The Zintl cluster approach avoids intrinsic particle uniformity issues arising from utilizing two metallic precursors with differing reduction rates. The method described herein also eliminates the need to utilize extremely high reaction temperatures, which makes it possible to access these materials as NPs, circumventing the agglomeration of the particles into bulk material.

This study shows that  $\text{PtSn}_4$  and  $\text{Ir}_3\text{Sn}_7$  intermetallic phases can now be accessed as NPs for the first time. As a result, critical oil reforming and direct ethanol fuel cell catalytic studies can now be investigated. PtSn phases are utilized as oil reforming catalysts in industry but the chemistry of the catalysts is not well established due to the inability to previously isolate  $\text{PtSn}_4$  due to the presence of the competing Pt-rich phases in the bulk phase. The fabrication method described in this thesis now allows two very important catalytic studies to be carried out. The catalytic activity of  $\text{PtSn}_4$  NPs may now be studied versus the bulk phase intermetallic, and versus  $\text{Pt}_3\text{Sn}$ ,  $\text{PtSn}$ ,  $\text{Pt}_2\text{Sn}_3$  and  $\text{PtSn}_2$  phases which have all been isolated as NPs via other methods.<sup>171,172</sup>

This research has presented the fabrication of intermetallic NPs from bimetallic Zintl clusters in a facile method that may be extended to various clusters in the growing library of known Zintl ions. We show that specific intermetallic phases are fabricated from a given Zintl cluster based on similarities

in the atomic arrangement of the two structures, and not necessarily based on the stoichiometry of the structures. Additional studies can be done to compare different phases formed from the oxidation of the icosahedral  $M@E_{12}$  ions versus the smaller  $Sn_9ML$  clusters, because the different structural arrangements of the clusters are likely to give access to unique intermetallic NPs.

The pre-organization of bimetallic Zintl clusters towards specific intermetallic phases may also open the door to intermetallic phases that have not been isolated even in the bulk phase. The metastable  $NiSn_4$  phase for example may be readily available via the oxidation of the structurally similar  $Sn_9Ni_2(cod)^{3-}$  Zintl ion. New intermetallics comprised of immiscible metals, such as Co and Cu, can now be targeted via the Zintl cluster route discussed in this thesis. Highly ordered trimetallic phases may be isolated via the co-oxidation of two bimetallic clusters, each containing one of the metals of interest. For example the controlled co-oxidation of  $Cu@Sn_9^{3-}$  and  $Co@HSn_9^{3-}$  could afford a  $CoCuSn$  intermetallic phase because the precursors possess similar structures that could fragment to give a single phase. Similar phases may be accessible via the oxidation of trimetallic Zintl clusters that possess both immiscible metals in the polyanionic structure, although the isolation of such precursors would first need to be achieved. Such a trimetallic cluster anion would act as a metastable trap to isolate the intermetallic phase of interest. Trimetallic Zintl clusters such as the  $Ni@Sn_9Cr(CO)_3^{4-}$  and  $Ni@Sn_9W(CO)_3^{4-}$  ions exist and have syntheses that may be flexible enough to give desired trimetallic Zintl clusters.

## Appendix

This appendix contains syntheses and structural analysis results of other ions prepared during the course of this study.

### Appendix A. Cobalt Derivatives of $\text{Sn}_9^{4-}$

There has been success in the synthesis of cobalt derivatives of the  $\text{Sn}_9^{4-}$  parent complex.  $\text{K}_4\text{Sn}_9$  reacts with  $\text{Co}_4(\text{CO})_{12}$  in en/tol solvent mixtures in the presence of 2,2,2-crypt and KO-*t*-Bu to give  $\text{Sn}_n\text{Co}_x\text{H}_y^{z-}$  cluster anions (**A**) ( $n = 8$  or  $9$ ;  $x = 0-2$ ;  $z = 2,3$ ;  $y$  is unknown). Ions **A** crystallizes from solution as part of a solid state mixture, in which it co-crystallizes with  $\text{HSn}_9^{3-}$  clusters as a  $[\text{K}(2,2,2\text{-crypt})]^+$  salt.

The crystal structure illustrated in Figure A1 is very complicated, showing disorder over six atomic sites. Contrary to the disorder over much of the cluster, the capping tin atom and the adjacent four tin atoms of the lower square of the cluster are not disordered. The capping Sn-Sn bonds have an average bond length of  $2.932(x)$  Å. The Sn-Sn bonds of the lower square of the antiprism have average bond lengths of  $3.201(x)$  Å. The disorder is in large part due to incomplete cobalt occupancy in the crystal lattice. In the preliminary structure, two independent clusters are present with one being that illustrated in Figure A1, while the other is an empty  $\text{HSn}_9^{3-}$  cage. The illustrated structure can be described as a superimposed structure due to the co-crystallization of clusters with 0-2 cobalt atoms present. No ligand was detected via X-ray crystallography, suggesting that the cluster is ligand-free or is ligated by an undetectable hydride.



It is more plausible that a hydride is present, though it has not been detected via  $^1\text{H}$  NMR spectroscopy.

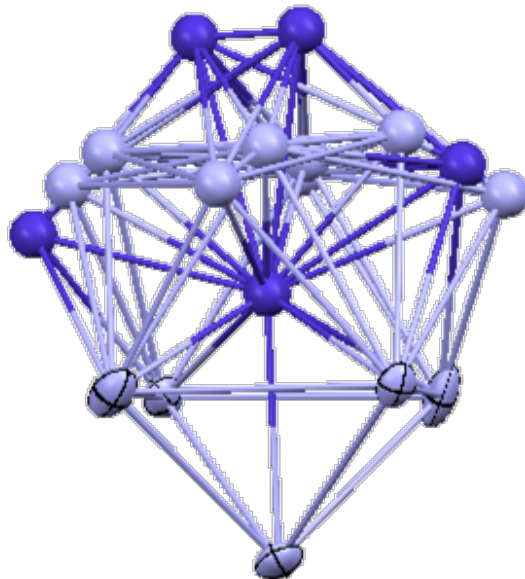


**Figure A1.** ORTEP drawing of the  $\text{Sn}_n\text{Co}_x\text{H}_y^{z-}$  (A) cluster mixture where  $n = 8-9$ ,  $x = 0-2$ ,  $z = 2-3$ , and  $y$  is unknown.

The identity of the co-crystallized clusters is not known with absolute certainty. The superimposed structure suggests that the clusters contain nine or possibly even eight tin atoms, and each of the unique clusters share the five ordered lattice positions. Innocuous structural assignments include the  $\text{Co@HSn}_9^{3-}$ ,  $\text{Sn}_9\text{CoH}^{3-}$ , and  $\text{Co@Sn}_9\text{CoH}^{3-}$  ions where the hypothetical structures are isostructural to  $\text{Ni@HSn}_9^{3-}$ ,<sup>73</sup>  $\text{Sn}_9\text{Cd}(\text{C}_6\text{H}_5)^{3-}$ ,<sup>70</sup> and  $\text{Ni@Sn}_9\text{NiCO}^{3-}$  respectively.<sup>58</sup>  $\text{Co@HSn}_9^{3-}$  and  $\text{Sn}_9\text{CoH}^{3-}$  are plausible structures containing 21 and 19 cluster bonding electrons and are therefore paramagnetic in nature, showing the possibility of a new set of paramagnetic Zintl. It is also important to note that clusters with a 2- charge cannot be ruled out despite the presence of three  $\text{K}(2,2,2\text{-crypt})^+$  ions in the unit cell of the solved structure. The close

proximity of an en solvent molecule to one of the cations suggests the presence of dianions in the mixture of unresolved clusters. The said en molecule possesses a K-N contact of 3.453 Å, which is in the range of an amide K-N bond. For example, the K-N bonds of potassium cyanamide range from 2.763-3.354 Å.<sup>180</sup> Likewise, potassium amide has K-N bonds from 2.875-3.307 Å.<sup>181</sup>

The above proposed structures for  $\text{Sn}_n\text{Co}_x\text{H}_y^{z-}$  are not definite as the number of protons/hydrides bound to the cluster cannot be determined. Additionally, there is no Sn occupancy present at the top of the cluster which suggests the presence of a rare  $\text{Sn}_8$ -cluster. The cobalt atoms about the upper waist of the clusters (Figure A1) suggest that a cluster with eight tin atoms is present, as tin has a zero-occupancy in the upper capping site of the cluster. The *arachno*- $\text{Sn}_8^{6-}$  ion was the first cluster of this type, reported by Sevov and coworkers.<sup>182</sup> The ion is a square antiprism seemingly bicapped by two lithium cations, while the  $\text{Sn}_8$  cobalt derivative described herein resembles an  $\text{HSn}_9^{3-}$  ion in which one of the tin atoms has been replaced by cobalt.

<sup>119</sup>Sn NMR experiments of the cobalt derivatives were unsuccessful, as no chemical shift has been detected at this time. The inability to detect <sup>119</sup>Sn signals could be a direct result of a dynamic equilibrium and/or paramagnetism of the product mixture. An average paramagnetic shift of 81.2 Hz was observed in an Evans Method type shift for the  $\text{Sn}_n\text{Co}_x\text{H}_y^{z-}$  reaction solution (Figure A2), though an unknown solution composition prevents the quantification of the molar susceptibility.

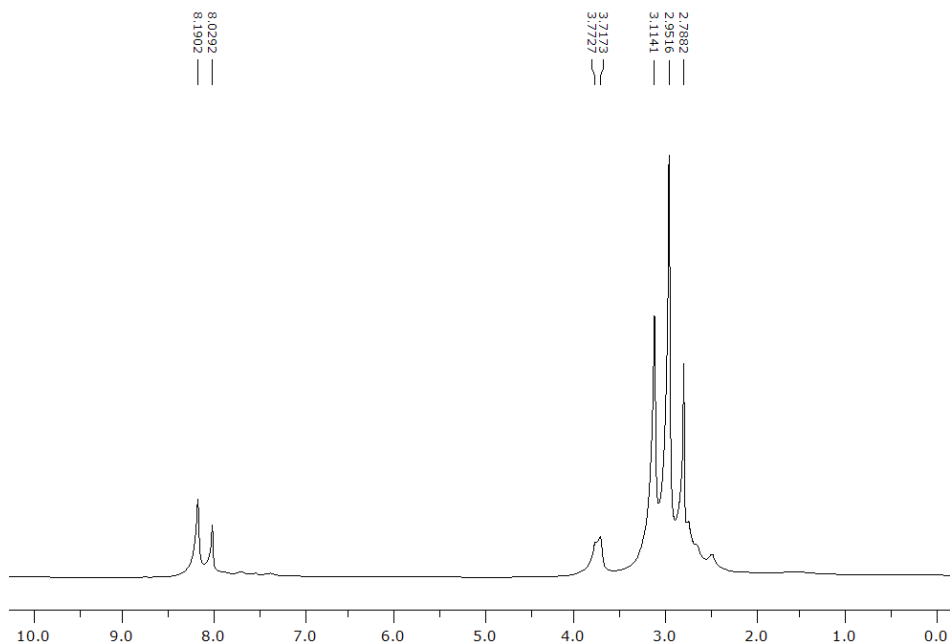


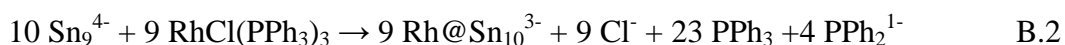
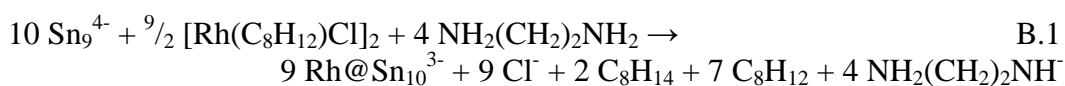
**Figure A2.** <sup>1</sup>H NMR spectrum for the reaction solution of  $K_4Sn_9$  and  $Co_4(CO)_{12}$  with paramagnetic shift observed with the use of a dmf internal standard . Data were recorded at 300 K at 500.1 MHz in dmf. An average shift of  $81.2 \pm 0.7$ Hz was observed for the three dmf protons.

### Preparation of Sn-Cobalt Cluster Mixture

In vial 1,  $K_4Sn_9$  (81 mg, 0.066 mmol) was dissolved in en (~2 mL), giving a dark red solution. Five equivalents of solid crypt (125 mg, 0.332 mmol) were added to the solution and allowed to stir for about ten minutes. In vial 2,  $Co_4(CO)_{12}$  (19 mg, 0.033 mmol) was dissolved in toluene (~4 mL) to produce an orange-yellow solution. The contents of vial 2 were slowly added to vial 1 and the reaction mixture was stirred for 2 h to yield a dark brown solution. The reaction mixture was then filtered through tightly packed glass wool in a pipet. Black crystals formed in the reaction vessel after 1 week (50 mg yield).

## Appendix B. Isolation of Rh@Sn<sub>10</sub><sup>3-</sup>

In the presence of five equivalents of 2,2,2-crypt, en solutions of K<sub>4</sub>Sn<sub>9</sub> react with tol solutions of [Rh(cod)Cl]<sub>2</sub> and RhCl(PPh<sub>3</sub>)<sub>3</sub> to give Rh@Sn<sub>10</sub><sup>3-</sup> (**B**) ions as the [K(2,2,2-crypt)]<sup>+</sup> salt. Ion **B** is synthesized according to Equations B.1 and B.2. The [K(2,2,2-crypt)]<sup>+</sup> salt is both air and moisture sensitive in solution and in the solid state.



The [K(2,2,2-crypt)]<sub>3</sub>[Rh@Sn<sub>10</sub>] salt is monoclinic, space group P2<sub>1</sub>/c, containing two clusters in the unit cell. The Rh@Sn<sub>10</sub><sup>3-</sup> ion is slightly distorted from D<sub>4d</sub> point symmetry, marked by the square antiprism bicapped by two apical Sn atoms with an endohedral Rh center as illustrated in Figure B1. Both clusters in the unit cell are disordered with one showing disorder across 3 atoms at the top of the cluster in which the top of the cluster is leaning 9° in the direction of either of two reflections. This unique crystallographic problem is indicative of a proton on the cluster, suggesting acid/base equilibrium in solution. Three views of the cluster, showing the disorder, are shown in Figure B1.

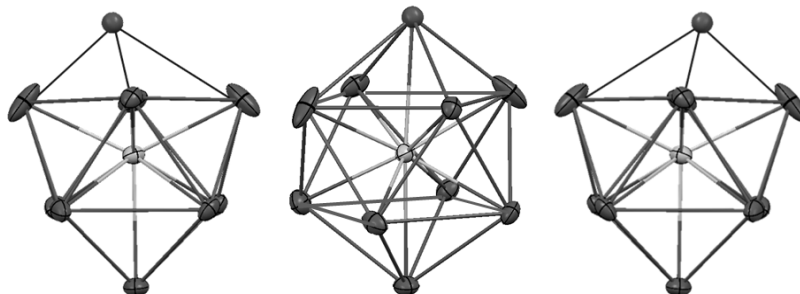


**Figure B1.** Drawings of  $\text{Rh@Sn}_{10}^{3-}$  (**B**), highlighting the bicapped square antiprism; and a side view of the disordered orientations of ion **3** (left and right). Thermal ellipsoids drawn at the 50% probability level.

Cluster **B** possesses a *closo* 22-electron (each Sn = 2e<sup>-</sup>, Rh = -1e<sup>-</sup>, charge = 3e<sup>-</sup>) framework with an interstitial rhodium with a -1 formal charge inside the  $\text{Sn}_{10}^{2-}$  cage.<sup>59</sup> The Rh-Sn and Sn-Sn bond lengths differ greatly when bonds involving the apical Sn-atoms are compared to the bonds about the waist of the cluster, highlighting the bicapped square anti-prismatic structure. The axial Sn-Rh bonds average 2.95 Å versus the remaining eight Sn-Rh bonds that average 2.69 Å. The average Sn-Sn bond distances to the capping Sn atoms (Sn1, Sn10) are the shortest at 2.99 Å (ave). The Sn-Sn contacts within the square planes are longest at 3.42 Å (ave) whereas the distances between the square planes are 3.02 Å.

### Preparation of $[\text{K}(\text{2,2,2-crypt})]_3[\text{Rh@Sn}_{10}] \cdot \text{solvent}$

In vial 1,  $\text{K}_4\text{Sn}_9$  (81 mg, 0.066 mmol) was dissolved in en (~2 mL), giving a dark red solution. Five equivalents of solid crypt (125 mg, 0.332 mmol) were added to the solution and allowed to stir for about 10 minutes. In vial 2,  $[\text{Rh}(\text{C}_8\text{H}_{12})\text{Cl}]_2$  (16 mg, 0.033 mmol) was dissolved in toluene (~2 mL) to produce a yellow solution. The contents of vial 2 were slowly added to vial 1

and the reaction mixture was stirred for 2 h to yield a dark greenish-brown solution. The reaction mixture was then filtered through tightly packed glass wool. Dark crystals formed in the reaction vessel after 1 week (44 mg yield). A similar reaction was performed using Wilkinson's catalyst (61 mg, 0.066 mmol) in the presence of K-*t*-OBu (4 mg, 0.033 mmol).

## References

- (1) Baudler, M.; Glinka, K. *Chem. Rev.* **1993**, *93*, 1623-1667.
- (2) Scharfe, S.; Fassler, T. F. *Philos. Trans. R. Soc. London, Ser. A.* **2010**, *368*, 1265-1284.
- (3) Sevov, S. C.; Goicoechea, J. M. *Organometallics* **2006**, *25*, 5678-5692.
- (4) Corbett, J. D. *Angew. Chem. Int. Ed.* **2000**, *39*, 670-690.
- (5) Andres, R. P.; Averback, R. S.; Brown, W. L.; Brus, L. E.; Goddard, W. A.; Kaldor, A.; Louie, S. G.; Moscovits, M.; Peercy, P. S.; Riley, S. J.; Siegel, R. W.; Spaepen, F.; Wang, Y. *J. Mater. Res.* **1989**, *4*, 704-736.
- (6) Aiken, J. D.; Finke, R. G. *J. Mol. Catal. A: Chem.* **1999**, *145*, 1-44.
- (7) Rao, C. N. R.; Vivekchand, S. R. C.; Biswasa, K.; Govindaraja, A. *Dalton Trans.* **2007**, 3728-3749.
- (8) Watzky, M. A.; Finke, R. G. *J. Am. Chem. Soc.* **1997**, *119*, 10382-10400.
- (9) Aiken, J. D.; Lin, Y.; Finke, R. G. *J. Mol. Catal. A: Chem.* **1996**, *114*, 29-51.
- (10) Schmid, G. *Angew. Chem. Int. Ed.* **2008**, *47*, 3496-3498.
- (11) Cao, B. P.; Neal, C. M.; Starace, A. K.; Ovchinnikov, Y. N.; Kresin, V. Z.; Jarrold, M. F. *J. Supercond. Novel Magn.* **2008**, *21*, 163-166.
- (12) Scharfe, S.; Kraus, F.; Stegmaier, S.; Schier, A.; Fassler, T. F. *Angew. Chem. Int. Ed.* **2011**, *50*, 3630-3670.
- (13) Fassler, T. F.; Hoffmann, S. D. *Angew. Chem. Int. Ed.* **2004**, *43*, 6242-6247.

- (14) Joannis, M. *C. R. Hebd. Senaces Acad. Sci.* **1891**, *113*, 795-798.
- (15) Joannis, M. *C. R. Hebd. Senaces Acad. Sci.* **1892**, *114*, 585-587.
- (16) Kraus, C. A. *J. Am. Chem. Soc.* **1907**, *29*, 1557-1571.
- (17) Smyth, F. H. *J. Am. Chem. Soc.* **1917**, *39*, 1299-1312.
- (18) Peck, E. B. *J. Am. Chem. Soc.* **1918**, *40*, 335-347.
- (19) Kraus, C. A. *J. Am. Chem. Soc.* **1922**, *44*, 1216-1239.
- (20) Zintl, E.; Dullenkopf, Z. *Z. Phys. Chem. Abt. B* **1932**, *16*, 183-194.
- (21) Zintl, E.; Goubeau, J.; Dullenkopf, W. *Z. Physik. Chem., Abt. A* **1931**, *154*, 1-46.
- (22) Zintl, E.; Harder, A. *Z. Physik. Chem., Abt. A* **1931**, *154*, 47-91.
- (23) Zintl, E.; Kaiser, H. *Z. Anorg. Allg. Chem.* **1933**, *211*, 113.
- (24) Kummer, D.; Diehl, L. *Angew. Chem. Int. Ed.* **1970**, *9*, 895.
- (25) Dietrich, B.; Lehn, J. M.; Sauvage, J. P. *Tetrahedron Lett.* **1969**, 2885-2888.
- (26) Lehn, J. M.; Sauvage, J. P.; Dietrich, B. *J. Am. Chem. Soc.* **1970**, *92*, 2916-2918.
- (27) Lok, M. T.; Tehan, F. J.; Dye, J. L. *J. Phys. Chem.* **1972**, *76*, 2975-2981.
- (28) Corbett, J. D.; Adolphson, D. G.; Merryman, D. J.; Edwards, P. A.; Armatis, F. J. *J. Am. Chem. Soc.* **1975**, *97*, 6267-6268.
- (29) Tobey, S. L.; Anslyn, E. V. *J. Am. Chem. Soc.* **2003**, *125*, 10963-10970.
- (30) Edwards, P. A.; Corbett, J. D. *Inorg. Chem.* **1977**, *16*, 903-907.
- (31) Campbell, J.; Schrobilgen, G. J. *Inorg. Chem.* **1997**, *36*, 4078-4081.
- (32) Goicoechea, J. M.; Sevov, S. C. *J. Am. Chem. Soc.* **2004**, *126*, 6860-6861.



- (33) Corbett, J. D.; Edwards, P. A. *J. Chem. Soc., Chem. Commun.* **1975**, 984-985.
- (34) Critchlow, S. C.; Corbett, J. D. *J. Am. Chem. Soc.* **1983**, *105*, 5715-5716.
- (35) Fassler, T. F.; Hunziker, M.; Spahr, M. E.; Lueken, H.; Schilder, H. A. *Anorg. Allg. Chem.* **2000**, *626*, 692-700.
- (36) Belin, C. H. E.; Corbett, J. D.; Cisar, A. *J. Am. Chem. Soc.* **1977**, *99*, 7163-7169.
- (37) Corbett, J. D.; Edwards, P. A. *J. Am. Chem. Soc.* **1977**, *99*, 3313-3317.
- (38) Goicoechea, J. M.; Sevov, S. C. *Inorg. Chem.* **2005**, *44*, 2654-2658.
- (39) Baudler, M. *Angew. Chem. Int. Ed.* **1982**, *21*, 492-512.
- (40) Corbett, J. D. *Chem. Rev.* **1985**, *85*, 383-397.
- (41) Belin, C. H. E. *J. Am. Chem. Soc.* **1980**, *102*, 6036-6040.
- (42) Bolle, U.; Tremel, W. *J. Chem. Soc., Chem. Commun.* **1992**, 91-93.
- (43) Critchlow, S. C.; Corbett, J. D. *Inorg. Chem.* **1984**, *23*, 770-774.
- (44) Cisar, A.; Corbett, J. D. *Inorg. Chem.* **1977**, *16*, 2482-2487.
- (45) Xu, L.; Bobev, S.; El-Bahraoui, J.; Sevov, S. C. *J. Am. Chem. Soc.* **2000**, *122*, 1838-1839.
- (46) Kraus, F.; Hanauer, T.; Korber, N. *Inorg. Chem.* **2006**, *45*, 1117-1123.
- (47) Thomas F. Fässler, S. D. H. *Angew. Chem. Int. Ed.* **2004**, *43*, 6242-6247.
- (48) Shriver, D. A., *Peter Inorganic Chemistry*; 3rd ed.; W. H. Freeman and Company: New York, New York, 1999.
- (49) Fässler, T. F. *Coord. Chem. Rev.* **2001**, *215*, 347-377.

- (50) Wilson, W. L.; Rudolph, R. W.; Lohr, L. L.; Taylor, R. C.; Pyykko, P. *Inorg. Chem.* **1986**, *25*, 1535-1541.
- (51) Moses, M. J.; Fettinger, J. C.; Eichhorn, B. W. *Inorg. Chem.* **2007**, *46*, 1036-1038.
- (52) Esenturk, E. N.; Fettinger, J.; Eichhorn, B. *J. Am. Chem. Soc.* **2006**, *128*, 9178-9186.
- (53) Chang, A. H. H.; Ermler, W. C.; Pitzer, R. M. *J. Chem. Phys.* **1991**, *94*, 5004-5010.
- (54) Cui, L. F.; Wang, L. S. *Int. Rev. Phys. Chem.* **2008**, *27*, 139-166.
- (55) Chen, Z.; Neukermans, S.; Wang, X.; Janssens, E.; Zhou, Z.; Silverans, R. E.; King, R. B.; Schleyer, P. v. R.; Lievens, P. *J. Am. Chem. Soc.* **2006**, *128*, 12829-12834.
- (56) Cui, L.-F.; Huang, X.; Wang, L.-M.; Li, J.; Wang, L.-S. *Angew. Chem. Int. Ed.* **2007**, *46*, 742-745.
- (57) Teixidor, F.; Luetkens, M. L.; Rudolph, R. W. *J. Am. Chem. Soc.* **1983**, *105*, 149-150.
- (58) Kesanli, B.; Fettinger, J.; Gardner, D. R.; Eichhorn, B. *J. Am. Chem. Soc.* **2002**, *124*, 4779-4786.
- (59) Wade, K. *Chem. Br.* **1975**, *11*, 177-183.
- (60) Mingos, D. M. P. *Nat. Phys. Sci.* **1972**, *236*, 99.
- (61) Eichhorn, B. W.; Haushalter, R. C.; Pennington, W. T. *J. Am. Chem. Soc.* **1988**, *110*, 8704-8706.
- (62) Kesanli, B.; Fettinger, J.; Eichhorn, B. *Chem. Eur. J.* **2001**, *7*, 5277-5285.

- (63) Campbell, J.; Mercier, H. P. A.; Franke, H.; Santry, D. P.; Dixon, D. A.; Schrobilgen, G. J. *Inorg. Chem.* **2002**, *41*, 86-107.
- (64) Yong, L.; Hoffmann, S. D.; Fassler, T. F. *Eur. J. Inorg. Chem.* **2005**, 3663-3669.
- (65) Scharfe, S.; Fassler, T. F. *Eur. J. Inorg. Chem.* **2010**, 1207-1213.
- (66) Goicoechea, J. M.; Sevov, S. C. *J. Am. Chem. Soc.* **2006**, *128*, 4155-4161.
- (67) Sun, Z. M.; Zhao, Y. F.; Li, J.; Wang, L. S. *J. Cluster Sci.* **2009**, *20*, 601-609.
- (68) Goicoechea, J. M.; Sevov, S. C. *Organometallics* **2006**, *25*, 4530-4536.
- (69) Zhou, B. B.; Denning, M. S.; Jones, C.; Goicoechea, J. M. *Dalton Trans.* **2009**, 1571-1578.
- (70) Zhou, B. B.; Denning, M. S.; Chapman, T. A. D.; Goicoechea, J. M. *Inorg. Chem.* **2009**, *48*, 2899-2907.
- (71) Scharfe, S.; Fassler, T. F.; Stegmaier, S.; Hoffmann, S. D.; Ruhland, K. *Chem. Eur. J.* **2008**, *14*, 4479-4483.
- (72) Gillett-Kunnath, M. M.; Paik, J. I.; Jensen, S. M.; Taylor, J. D.; Sevov, S. *C. Inorg. Chem.* **2011**, *50*, 11695-11701.
- (73) Kocak, F. S.; Downing, D. O.; Zavalij, P.; Lam, Y.-F.; Vedernikov, A. N.; Eichhorn, B. *Submitted to J. Am. Chem. Soc.* **2012**.
- (74) Kesanli, B.; Halsig, J. E.; Zavalij, P.; Fettingner, J. C.; Lam, Y.-F.; Eichhorn, B. W. *J. Am. Chem. Soc.* **2007**, *129*, 4567-4574.
- (75) Kocak, F. S.; Zavalij, P.; Eichhorn, B. *Chem. Eur. J.* **2011**, *17*, 4858-4863.
- (76) Seifert, G. *Nat Mater* **2004**, *3*, 77-78.

- (77) Hagelberg, F.; Xiao, C.; Lester, W. A. *Phys. Rev. B.* **2003**, *67*, 9.
- (78) Kumar, V.; Kawazoe, Y. *Appl. Phys. Lett.* **2002**, *80*, 859-861.
- (79) Kumar, V.; Kawazoe, Y. *Appl. Phys. Lett.* **2003**, *83*, 2677-2679.
- (80) Kumar, V.; Singh, A. K.; Kawazoe, Y. *Nano Lett.* **2004**, *4*, 677-681.
- (81) Lu, J.; Nagase, S. *Phys. Rev. Lett.* **2003**, *90*, 115506.
- (82) Lu, J.; Nagase, S. *Chem. Phys. Lett.* **2003**, *372*, 394-398.
- (83) Sen, P.; Mitas, L. *Phys. Rev. B.* **2003**, *68*, 155404.
- (84) Sun, Q.; Wang, Q.; Briere, T. M.; Kumar, V.; Kawazoe, Y.; Jena, P. *Phys. Rev. B* **2002**, *65*, 235417.
- (85) Esenturk, E. N.; Fettinger, J.; Lam, Y. F.; Eichhorn, B. *Angew. Chem. Int. Ed.* **2004**, *43*, 2132-2134.
- (86) Esenturk, E. N.; Fettinger, J.; Eichhorn, B. *Chem. Commun.* **2005**, 247-249.
- (87) Neukermans, S.; Janssens, E.; Chen, Z. F.; Silverans, R. E.; Schleyer, P. v. R.; Lievens, P. *Phys. Rev. Lett.* **2004**, *92*, 163401.
- (88) Wang, J. Q.; Stegmaier, S.; Fassler, T. F. *Angew. Chem. Int. Ed.* **2009**, *48*, 1998-2002.
- (89) Zhou, B. B.; Denning, M. S.; Kays, D. L.; Goicoechea, J. M. *J. Am. Chem. Soc.* **2009**, *131*, 2802-2803.
- (90) Korber, N. *Angew. Chem. Int. Ed.* **2009**, *48*, 3216-3217.
- (91) Wang, J.; Chen, X.; Liu, J. H. *J. Phys. Chem. A.* **2008**, *112*, 8868-8876.
- (92) Rios, D.; Sevov, S. C. *Inorg. Chem.* **2010**, *49*, 6396-6398.

- (93) Moses, M. J.; Fettinger, J. C.; Eichhorn, B. W. *Science* **2003**, *300*, 778-780.
- (94) Goicoechea, J. M.; Sevov, S. C. *Angew. Chem. Int. Ed.* **2005**, *44*, 4026-4028.
- (95) Gardner, D. R.; Fettinger, J. C.; Eichhorn, B. W. *Angew. Chem. Int. Ed.* **1996**, *35*, 2852-2854.
- (96) Esenturk, E. N.; Fettinger, J.; Eichhorn, B. *Polyhedron* **2006**, *25*, 521-529.
- (97) Goicoechea, J. M.; Sevov, S. C. *J. Am. Chem. Soc.* **2005**, *127*, 7676-7677.
- (98) Esenturk, E. N.; Fettinger, J. C.; Eichhorn, B. W. *J. Am. Chem. Soc.* **2006**, *128*, 12-13.
- (99) Kocak, F. S.; Zavalij, P.; Lam, Y.-F.; Eichhorn, B. W. *Inorg. Chem.* **2008**, *47*, 3515-3520.
- (100) Sun, Z. M.; Xiao, H.; Li, J.; Wang, L. S. *J. Am. Chem. Soc.* **2007**, *129*, 9560-9561.
- (101) Xu, L.; Sevov, S. C. *J. Am. Chem. Soc.* **1999**, *121*, 9245-9246.
- (102) Ugrinov, A.; Sevov, S. C. *J. Am. Chem. Soc.* **2002**, *124*, 10990-10991.
- (103) Ugrinov, A.; Sevov, S. C. *Inorg. Chem.* **2003**, *42*, 5789-5791.
- (104) Downie, C.; Tang, Z. J.; Guloy, A. M. *Angew. Chem. Int. Ed.* **2000**, *39*, 337-340.
- (105) Spiekermann, A.; Hoffmann, S. D.; Kraus, F.; Fessler, T. F. *Angew. Chem. Int. Ed.* **2007**, *46*, 1638-1640.
- (106) Spiekermann, A.; Hoffmann, S. D.; Fessler, T. F.; Krossing, I.; Preiss, U. *Angew. Chem. Int. Ed.* **2007**, *46*, 5310-5313.

- (107) Nienhaus, A.; Hauptmann, R.; Fassler, T. F. *Angew. Chem. Int. Ed.* **2002**, *41*, 3213-3215.
- (108) Kocak, F. S., University of Maryland, 2011.
- (109) Wang, J. X.; Brankovic, S. R.; Zhu, Y.; Hanson, J. C.; Adzic, R. R. *J. Electrochem. Soc.* **2003**, *150*, A1108-A1117.
- (110) Igarashi, H.; Fujino, T.; Zhu, Y.; Uchida, H.; Watanabe, M. *Phys. Chem. Chem. Phys.* **2001**, *3*, 306-314.
- (111) Matsumoto, F.; Roychowdhury, C.; DiSalvo, F. J.; Abruna, H. D. *J. Electrochem. Soc.* **2008**, *155*, B148-B154.
- (112) Roychowdhury, C.; Matsumoto, F.; Mutolo, P. F.; Abruna, H. D.; DiSalvo, F. J. *Chem. Mater.* **2005**, *17*, 5871-5876.
- (113) Roychowdhury, C.; Matsumoto, F.; Zeldovich, V. B.; Warren, S. C.; Mutolo, P. F.; Ballesteros, M.; Wiesner, U.; Abruna, H. D.; DiSalvo, F. J. *Chem. Mater.* **2006**, *18*, 3365-3372.
- (114) Leonard, B. M.; Zhou, Q.; Wu, D. N.; DiSalvo, F. J. *Chem. Mater.* **2011**, *23*, 1136-1146.
- (115) Cable, R. E.; Schaak, R. E. *Chem. Mater.* **2005**, *17*, 6835-6841.
- (116) Chou, N. H.; Schaak, R. E. *J. Am. Chem. Soc.* **2007**, *129*, 7339-7345.
- (117) Bondi, J. F.; Misra, R.; Ke, X. L.; Sines, I. T.; Schiffer, P.; Schaak, R. E. *Chem. Mater.* **2010**, *22*, 3988-3994.
- (118) Liu, Z. F.; Jackson, G. S.; Eichhorn, B. W. *Angew. Chem. Int. Ed.* **2010**, *49*, 3173-3176.

- (119) Liu, Z.; Jackson, G. S.; Eichhorn, B. W. *Energy Environ. Sci.* **2011**, *4*, 1900-1903.
- (120) Liu, Z.; Hu, J. E.; Wang, Q.; Gaskell, K.; Frenkel, A. I.; Jackson, G. S.; Eichhorn, B. *J. Am. Chem. Soc.* **2009**, *131*, 6924-6925.
- (121) Ji, X. L.; Lee, K. T.; Holden, R.; Zhang, L.; Zhang, J. J.; Botton, G. A.; Couillard, M.; Nazar, L. F. *Nat. Chem.* **2010**, *2*, 286-293.
- (122) Silaghi-Dumitrescu, I.; King, B. *Stud. Univ. Babeş-Bolyai.* **2008**, *53*, 83-88.
- (123) Wang, J.-Q.; Stegmaier, S.; Wahl, B.; Fässler, T. F. *Chem. Eur. J.* **2010**, *16*, 1793-1798.
- (124) Downing, D. O.; Zavalij, P.; Eichhorn, B. W. *Eur. J. Inorg. Chem.* **2010**, 890-894.
- (125) Schenk, C.; Schnepf, A. *Chem. Commun.* **2009**, 3208-3210.
- (126) James, S. L.; Mingos, D. M. P.; Xu, X. L.; White, A. J. P.; Williams, D. J. *J. Chem. Soc., Dalton Trans.* **1998**, 1335-1340.
- (127) Xu, C.; Baum, T. H.; Rheingold, A. L. *Chem. Mater.* **1998**, *10*, 2329-2331.
- (128) Martin, M.; Sola, E.; Torres, O.; Plou, P.; Oro, L. A. *Organometallics* **2003**, *22*, 5406-5417.
- (129) Cipot, J.; Vogels, C. M.; McDonald, R.; Westcott, S. A.; Stradiotto, M. *Organometallics* **2006**, *25*, 5965-5968.
- (130) Cipot, J.; McDonald, R.; Ferguson, M. J.; Schatte, G.; Stradiotto, M. *Organometallics* **2007**, *26*, 594-608.

- (131) Lee, H. M.; Jiang, T.; Stevens, E. D.; Nolan, S. P. *Organometallics* **2001**, *20*, 1255-1258.
- (132) Brown, M. D. L., W.; Gillian, R.; Webster, M. *Dalton Trans.* **2006**, 4039-4046.
- (133) Armatas, G. S.; Kanatzidis, M. G. *Science* **2006**, *313*, 817-820.
- (134) Schleyer, P. v. R.; Maerker, C.; Dransfeld, A.; Jiao, H.; Hommes, N. J. R. v. E. *J. Am. Chem. Soc.* **1996**, *118*, 6317-6318.
- (135) Schleyer, P. V.; Jiao, H. *J. Pure Appl. Chem.* **1996**, *68*, 209-218.
- (136) Pople, J. A.; Untch, K. G. *J. Am. Chem. Soc.* **1966**, *88*, 4811-4815.
- (137) Fleischer, U.; Kutzelnigg, W.; Lazzeretti, P.; Muhlenkamp, V. *J. Am. Chem. Soc.* **1994**, *116*, 5298-5306.
- (138) Queneau, V.; Sevov, S. C. *Inorg. Chem.* **1998**, *37*, 1358-1360.
- (139) Meek, D. W.; Kreter, P. E.; Christoph, G. G. *J. Organomet. Chem.* **1982**, *231*, C53-C58.
- (140) Cowie, M.; Dickson, R. S. *Inorg. Chem.* **1981**, *20*, 2682-2688.
- (141) Cowie, M. *Inorganic Chemistry* **1979**, *18*, 286-292.
- (142) Miessler, G. L.; Tarr, D. A. *Inorganic Chemistry*; 3rd ed.; Pearson Prentice-Hall: Englewood, NJ, 2004.
- (143) Steyl, G. *Acta Crystallogr., Sect. E.* **2007**, *63*, m23-m25.
- (144) Tiburcio, J.; Bernes, S.; Torrens, H. *Polyhedron* **2006**, *25*, 1549-1554.
- (145) Christoph, G. G.; Halpern, J.; Khare, G. P.; Koh, Y. B.; Romanowski, C. *Inorg. Chem.* **1981**, *20*, 3029-3037.



- (146) Connelly, N. G.; Emslie, D. J. H.; Geiger, W. E.; Hayward, O. D.;  
Linehan, E. B.; Orpen, A. G.; Quayle, M. J.; Rieger, P. H. *J. Chem. Soc., Dalton Trans.* **2001**, 670-683.
- (147) Burkhardt, E. W.; Mercer, W. C.; Geoffrey, G. L. *Inorg. Chem.* **1984**, *23*,  
1779-1782.
- (148) Kreter, P. E.; Meek, D. W. *Inorg. Chem.* **1983**, *22*, 319-326.
- (149) Farrugia, L. J.; Braga, D.; Grepioni, F. *J. Organomet. Chem.* **1999**, *573*,  
60-66.
- (150) Plecnik, C. E.; Liu, S. M.; Chen, X. N.; Meyers, E. A.; Shore, S. G. *J. Am. Chem. Soc.* **2004**, *126*, 204-213.
- (151) Albano, V.; Chini, P.; Scatturi, V. *Chem. Commun.* **1968**, 163-164.
- (152) Orpen, A. G.; Brammer, L.; Allen, F. H.; Kennard, O.; Watson, D. G.;  
Taylor, R. *J. Chem. Soc., Dalton Trans.* **1989**, S1-S83.
- (153) Harley, A. D.; Whittle, R. R.; Geoffroy, G. L. *Organometallics* **1983**, *2*,  
60-63.
- (154) Bailey, W. I.; Collins, D. M.; Cotton, F. A.; Baldwin, J. C.; Kaska, W. C.  
*J. Organomet. Chem.* **1979**, *165*, 373-381.
- (155) Jones, R. A.; Stuart, A. L.; Atwood, J. L.; Hunter, W. E. *Organometallics*  
**1983**, *2*, 1437-1441.
- (156) Brammer, L.; McCann, M. C.; Bullock, R. M.; McMullan, R. K.;  
Sherwood, P. *Organometallics* **1992**, *11*, 2339-2341.
- (157) Gervasio, G.; Kettle, S. F. A.; Musso, F.; Rossetti, R.; Stanghellini, P. L.  
*Inorg. Chem.* **1995**, *34*, 298-305.

- (158) Wu, J. X.; Fanwick, P. E.; Kubiak, C. P. *Organometallics* **1987**, *6*, 1805-1807.
- (159) Lin, Y.-S.; Yamamoto, A. *Organometallics* **1998**, *17*, 3466-3478.
- (160) Dai, F. R.; Xu, L. *Inorg. Chem. Acta* **2006**, *359*, 4265-4273.
- (161) Mazanec, T. J.; Tau, K. D.; Meek, D. W. *Inorg. Chem.* **1980**, *19*, 85-91.
- (162) Lavastre, O.; Bonnet, G.; Boni, G.; Kubicki, M. M.; Moïse, C. *J. Organomet. Chem.* **1997**, *547*, 141-147.
- (163) Boni, G.; Moïse, C. *Polyhedron* **1998**, *17*, 261-265.
- (164) Dulebohn, J. I.; Ward, D. L.; Nocera, D. G. *J. Am. Chem. Soc.* **1988**, *110*, 4054-4056.
- (165) Huheey, J. E.; Keiter, E. A.; Keiter, R. L. *Inorganic Chemistry: Principles of Structure and Reactivity*; 4th ed.; Harper Collins College Publishers: New York, New York, 1993.
- (166) Choi, S. Y.; Lee, S. C.; Lee, H. J.; Ahn, H. S.; Kim, S. W.; Ryu, J. Y. *Phys. Rev. B.* **2002**, *66*, 155208.
- (167) Lu, J.; Wei, S.; Yu, W. C.; Zhang, H. B.; Qian, Y. T. *Inorg. Chem.* **2004**, *43*, 4543-4545.
- (168) Butler, L.; Redmond, G.; Fitzmaurice, D. *J. Phys. Chem.* **1993**, *97*, 10750-10755.
- (169) Larese, C.; Campos-Martin, J. M.; Calvino, J. J.; Blanco, G.; Fierro, J. L. G.; Kang, Z. C. *J. Catal.* **2002**, *208*, 467-478.
- (170) Kunnen, B.; Niepmann, D.; Jeitschko, W. *J. Alloys Compd.* **2000**, *309*, 1-9.

- (171) Bauer, J. C.; Chen, X.; Liu, Q. S.; Phan, T. H.; Schaak, R. E. *J. Mater. Chem.* **2008**, *18*, 275-282.
- (172) Cable, R. E.; Schaak, R. E. *J. Am. Chem. Soc.* **2006**, *128*, 9588-9589.
- (173) Xie, Y.; Lu, J.; Yan, P.; Jiang, X. C.; Qian, Y. T. *Chem. Lett.* **2000**, 114-115.
- (174) Nordmark, E.-L.; Wallner, O.; Häussermann, U. *J. Solid State Chem.* **2002**, *168*, 34-40.
- (175) Sreeraj, P.; Kurowski, D.; Hoffmann, R.-D.; Wu, Z.; Pöttgen, R. *J. Solid State Chem.* **2005**, *178*, 3420-3425.
- (176) Schlüter, M.; Häussermann, U.; Heying, B.; Pöttgen, R. *J. Solid State Chem.* **2003**, *173*, 418-424.
- (177) Li, R.; Hao, H.; Cai, W.-B.; Huang, T.; Yu, A. *Electrochem. Commun.* **2010**, *12*, 901-904.
- (178) Breinlich, C.; Haubrich, J.; Becker, C.; Valcarcel, A.; Delbecq, F.; Wandelt, K. *J. Catal.* **2007**, *251*, 123-130.
- (179) Cao, L.; Sun, G.; Li, H.; Xin, Q. *Electrochem. Commun.* **2007**, *9*, 2541-2546.
- (180) Becker, M.; Jansen, M. *Solid State Sciences* **2000**, *2*, 711-715.
- (181) Jacobs, H.; Vonosten, E. *Z. Naturforsch., B: Chem. Sci.* **1976**, *31*, 385-386.
- (182) Bobev, S.; Sevov, S. C. *Angew. Chem. Int. Ed.* **2000**, *39*, 4108-4110.